OPTICAL PROPERTIES AND PHOTOCATALYTIC ACTIVITY OF 2D MATERIALS

Thesis by

Srilatha Arra
Registration ID : 20133236

In partial fulfillment of the requirements
for the degree of
Doctor of Philosophy

Under the supervision of

Dr. Mukul Kabir
Department of Physics

Indian Institute of Science Education and Research
Pune, India

June 2021

CERTIFICATE

This is to certify that the work incorporated in the thesis entitled *"Optical properties and photocatalytic activity of 2D materials"* submitted by Srilatha Arra was carried out by the candidate under my supervision. To the best of my knowledge, the work presented here or any part of it has not been included in any other thesis submitted previously for the award of any degree or diploma from any other university or institution.

Dr. Mukul Kabir

Thesis Supervisor

DECLARATION

I, *Srilatha Arra*, declare that this Ph.D. thesis entitled *Optical properties and photocatalytic activity of 2D materials* was carried out by me for the degree of Doctor of philosophy under the guidance and supervision of Dr. Mukul Kabir. For the present thesis, which I am submitting to the institute, no degree or diploma or distinction has been conferred on me before, either in this or in any other University.

Srilatha
Srilatha Arra

ID: 20133236

To my beloved family members

ACKNOWLEDGEMENTS

First and foremost, I would like to express my sincere gratitude to my advisor Prof. Dr. Mukul Kabir for the continuous support of my PhD study and related research, for his ideas, advice, patience, motivation, and immense knowledge. He has always provided me the space to work in my own way. He was always beside me with his valuable advice and support during each up and down in my Ph.D. life. Beside thesis related work, his friendly nature helped me to approach him without any hesitation any type of problem and, he gave me useful advice. His guidance helped me in all the time of research and writing of this thesis. I could not have imagined having a better advisor and mentor for my Ph.D. study.

Besides my advisor, I would like to thank the rest of my thesis committee: Dr. Ghosh Prasenjit, Dr. Kavita Joshi, for their insightful comments and encouragement, but also for the hard question which incented me to widen my research from various perspectives.

I would like to thank my labmates, Rohit Babar, Chandan Kumar Singh, Nitin, Tilak, Ramya, Bhagyashri Bhat, Deepak Roy.

This thesis would not have been possible without the financial support of UGC, and IISER Pune

Last but not the least, I would like to thank my family: my parents, husband and to my brothers and sisters for supporting me spiritually throughout the writing this thesis and my life in general.

SYNOPSIS

Two-dimensional semiconductors, owing to their large active surface area and extraordinary electronic properties, are promising candidates for catalysis in clean energy applications. In this context, we investigate the optical properties of various two-dimensional materials such as phosphorene, graphene nitride and transition-meal dichalcogenides within different first-principles hierarchies.

First, we will discuss the two-dimensional phosphorene and its derivatives. Since the pristine phosphorene is unstable in air and easily oxidized, we exploit this chemical instability to our advantage. We argue that the stable derivatives with N, O and S coverages have the correct band alignment necessary for photo-catalysis along with high photo-absorption capability. Next, we will discuss the possibilities in designer van der Waals heterostructures with graphitic carbon nitride g-C_3N_4 and Janus transition-metal dichalcogenides MoXY. The results are discussed in the context of photocatalytic water splitting and solar-to-hydrogen conversion efficiency.

In the end, we will discuss excitonic properties in the two-dimensional materials, which is fundamentally very different from their bulk counterparts due to much weaker electron screening in the reduced dimension. We describe a tractable hydrogenic model, where the parameters are calculated from inexpensive and conventional density functional theory. The results, at first, are benchmarked against relatively more accurate GW-BSE calculations and available experimental results. Within this methodology, the effects of strain in the lattice and impurities are investigated in phosphorene. Exciton renormalization due to better electron screening is investigated in thicker samples and heterostructures. Excellent agreement between the results and the available experimental results indicates general applicability of the hydrogenic model to other two-dimensional materials.

TABLE OF CONTENTS

CHAPTER 1

INTRODUCTION

1.1 Two-dimensional materials

Two-dimensional materials gained extensive interest among the researchers after preparation of graphene by mechanical exfoliation of highly oriented pyrolytic graphite in 2004. [1] Graphene has zero bandgap, which limits the applications, and leads to the search for alternative materials. 2D materials have distinct physical and chemical properties such as a large surface area, layer dependent bandgap, excellent electronic, mechanical, and optical properties, which originate from their ultrathin thickness and 2D morphological features. Several hundred different 2D materials have been investigated, including silicone, [2] germanene, [3] h-BN, [4] graphene, [5] black phosphorous, [6] MXenes, [7] etc.

Transition metal dichalcogenides (TMDs) are well studied 2D materials that differ from the semimetallic nature of graphene. The energy spectrum of TMDs ranged from visible to near infrared wavelength region. [8, 9] These atomically thin 2D semiconductors have exceptional optical properties such as the indirect-to-direct bandgap transition from bulk to the monolayer, [10, 11] rich spin-valley interplays, [12–14] strong light–matter interactions, [15–17] and large exciton binding energy. [11, 18–21] The bandgaps in TMDs can be tunable by applying of an external electric field or mechanical strain, [22–24] which is desired in optoelectronic applications. Duerloo et al. theoretically reported that mechanical deformations can switch thermodynamic stability between a semiconducting and a metallic crystal structure in Mo and W-dichalcogenide monolayers. [25] They observed

that molybdenum telluride ($MoTe_2$) exhibits such phase transitions, which can be utilized to exploit the optical response of the materials.

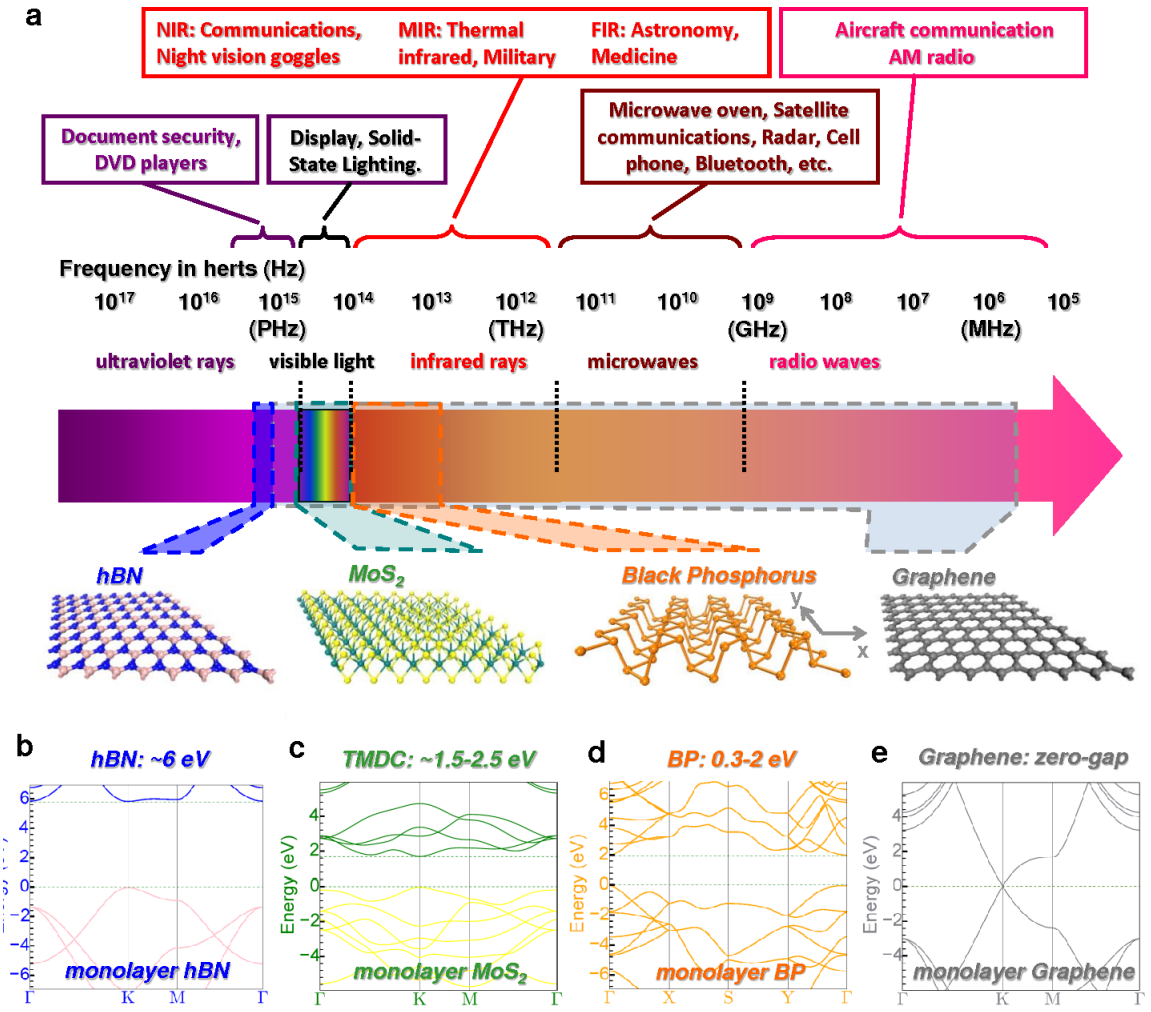

Figure 1.1: (a) Electromagnetic radiation spectrum, which utilized in various applications. h-BN, MoS_2, black phosphorous, and graphene covered a wide range in the electromagnetic spectrum.(b)-(e) Atomic crystal structures , and bandstructures of h-BN, MoS_2, black phosphorous, and graphene, respectively. Figure adopted from reference, [26] with permission from Springer Nature.

Excitonic effects dominate the optical response in 2D monolayer semiconductors. [18, 20, 27, 28] Experimentally excitons observed at room temperature, due to the presence of lower dimensionality and weak dielectric screening. The exciton binding energy of 2D materials is more than one order of magnitude higher

than those in bulk semiconductors. The electronic gap (quasiparticle) is larger than the band gap observed in optical absorption experiments. In group-6, two-dimensional TMDs, large exciton binding energies of 0.5–0.8 eV predicted with the GW-BSE method and measured experimentally. [18, 20, 27, 28] These values are in the order of those observed in carbon nanotubes, organic molecules, and some quantum dots, where all cases have the weak dielectric screening. The excitons in 2D-TMDs are of the Wannier type and thus delocalized over several unit cells. The radius of the lowest-energy exciton in MoS_2 and $MoSe_2$ have been computed to be of order 1.5 nm. [20, 27] Excitons in 2D materials can be bright or dark in character, which can be excited or not by light absorption in the linear regime, respectively, as followed by the dipole selection rules. [29] Dark excitons can be accessed, using two-photon absorption, which has different selection rules than one-photon absorption. [30]

Comparing with TMDs, black phosphorous (BP) has emerged as a new 2D semiconductor. [31] BP has useful properties for light emission as well as light absorption, and it is a direct bandgap material nevertheless of the thickness. [32, 33] The direct bandgap semiconductors are important for realizing high-efficiency light-emitting devices because the direct bandgap transition have much higher quantum efficiency than the indirect transition, which needs the additional phonon energy to conserve the momentum. The puckered structure of phosphorene gives highly anisotropic nature, which leads to unique optical and optoelectronic properties. [33, 34] The optical and quasiparticle band-gaps of monolayer black phosphorus are 1.3 ± 0.02 and 2.2 ± 0.1 eV, respectively. [35] Exciton binding energy of monolayer black phosphorene is $\sim$ 0.9 eV. As phosphorene is highly anisotropic, high exciton binding energy, it is a promising material for optoelectronics. The exciton binding energy of phosphorene layers depends on polarizability but not on the effective masses. [36]

Hexagonal boron nitride (h-BN) with the bandgap of 6 eV is the most attractive insulator these days. [37] The h-BN has atomically flat and smooth surface with lack of dangling bonds, it has been used as an ideal substrate for other 2D conducting channels such as graphene and TMDCs. [38–40]

1.2 Photocatalysis

Hydrogen is a promising energy carrier, as it has high energy density. [41] Hydrogen can be generated from fossil fuels, biomass, and water. If hydrogen is derived from fossil fuels and biomass, CO_2 is the byproduct which is not environmentally friendly. Hydrogen can be produced from water, where green gas emission is not observed. Water splitting is not a spontaneous reaction, where external energy has to be supplied to produce the hydrogen from water. Renewable energy sources, such as solar energy can be used to split the water molecules.

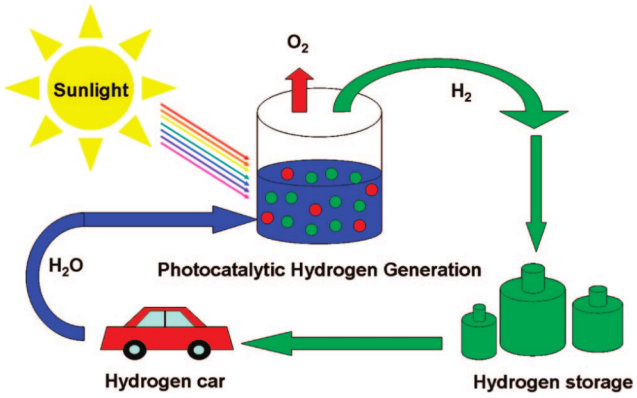

Figure 1.2: Schematic image of photocatalytic hydrogen production. Figure adopted from reference, [41] with permission from the American Chemical Society.

Photocatalytic water splitting ($H_2O \rightarrow H_2 + O_2$) consists of hydrogen evolution reaction (HER) ($2H^+ + 2e^- \rightarrow H_2$), and oxygen evolution reaction (OER) ($H_2O + 2h^+ \rightarrow \frac{1}{2}O_2 + 2H^+$). [42] As water splitting is an uphill reaction, it requires 237 kJ/moles of change in the Gibbs free energy [43], which is equivalent to 1.23 eV

from the Nernst equation $E^0 = -\frac{\Delta G}{nF}$. Here, E^0 is the electrode potential, n is the number of electrons per mole and F is the Faraday constant in C mol^{-1}. [44]

The reduction potential of the proton is 0-0.59 pH, and the oxidation potential of water is 1.23-0.59 pH, where V vs NHE. [45] Pure water has pH=7, -0.41 V, and 0.82 V is the reduction potential of hydrogen production, the oxidation potential of oxygen evolution from pure water, respectively. Thus, a semiconductor should have minimum 1.23 eV band gap to become a photocatalyst of water splitting reactions. However, all the semiconductors which have band gap greater than 1.23 eV can not become photocatalysts of water splitting. The minimum criteria of a water splitting photocatalyst are the band gap, and then the conduction band minimum should be located above the reduction potential (negative), the valance band maximum should be located below the oxidation potential (more positive).

Solar hydrogen production consists of photophysical processes such as photon absorption, generation of charge carriers, recombination and separation of photogenerated carriers; and photochemical processes such as migration, and utilization of excited carriers in the redox reactions. When a photocatalyst is irradiated by light, it absorbs the photons with different energies. When a semiconductor absorbs photons with greater energy than the band gap, the electrons in the VBM excites to the CBM by leaving holes in the VBM. Now excited electron-hole pairs are generated by absorbing the photons, but the excited electrons in the conduction band can fall back to the valance band by the radiative or non-radiative process. Thus, the recombination of excited charge carriers can happen and annihilates the water redox reactions. The charge carriers, which survived from the recombination, migrate to the surface and participates in the corresponding redox reactions. The migration of excited carriers to the surface active sites happens by diffusion or electric fields generated at the semiconductor/electrolyte and semiconductor/cocatalyst interfaces. [46]

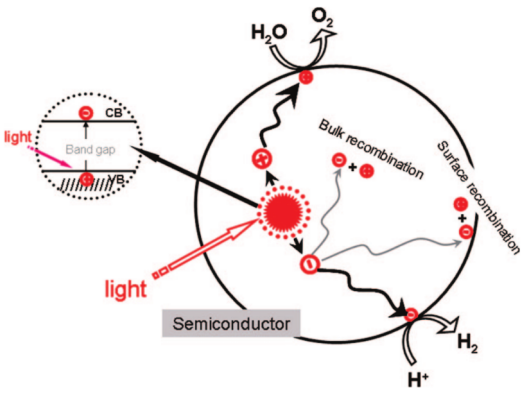

Figure 1.3: Processes in photocatalytic water splitting. Figure adopted from reference, [41] with permission from the American Chemical Society.

The photogenerated H_2 and O_2 can react and form H_2O on the surface, it is called a surface back reaction. This reduces the solar hydrogen yield, the addition of sacrificial reagents and separating the photocatalytic activity sites can reduce the back reaction. [41]

A wide range of semiconducting materials is invented as photocatalysts for water splitting reactions. The photocatalysts are categorized into 3 types

1.3 First generation of photocatalysts

Metals, which are UV-active known as first generation photocatalysts for water splitting. d^0 metal(Ti^{4+}, Zr^{4+},Nb^{5+}, Ta^{5+}, W^{6+}, Mo^{6+}) oxides, d^{10} metal (In^{3+}, Ga^{3+}, Ge^{4+}, Sn^{4+}, Sb^{5+}) oxides, f^0 metal (Ce^{4+}) oxides and non-oxide (ZnS in SO_3^{-2} solution, [47] and InP [48]) are UV photocatalysts for water splitting.

TiO_2 (d^0) is the first discovered photocatalyst for water splitting under UV irradiation. The energy conversion efficiency is very poor, because of the following reasons, [49]

I. Electrons from CBM recombine with the holes in VBM and produce heat or photons.

II. Water splitting into hydrogen and oxygen is an uphill reaction, the backward reaction of hydrogen with oxygen to form water can happen easily.

III. As TiO_2 has a wide band gap of 3.2 eV, it utilizes UV light. UV light is about only 4% in solar radiation energy, while visible light accounts for about 50%. The wide band gap of TiO_2 limits the utilization of solar energy, which leads to less efficiency towards photocatalytic hydrogen production.

To overcome the above limits, many criteria were applied, such as the addition of electron donors to suppress the recombination of photogenerated carriers. By adding carbonate salts, the backward reaction of water dissociation can be suppressed. Doping with noble metals such as, Pt, [50–52] Au, [51, 52] Ag, [53] Pd, [52] and Cu [54] are reported as efficient to achieve the photocatalytic enhancement towards water splitting reactions.

1.4 Second generation of photocatalysts

The metals, which are active under visible light, come under the second generation of photocatalysts. Au/TiO_2 acts as visible light photocatalyst. [55] Lamellar Niobic acid (HNb_3O_8) with nitrogen dopant, acts as visible light active photocatalyst. [56] $Zn_{(1-x)}Cd_xS$ solid solutions reported as visible light photocatalysts. [57] Self-doped Ti^{+3} in TiO_2 is reported as visible light photocatalyst. [58]

1.5 Third generation of photocatalysts

2D metals/non-metals with visible light absorption falls under the third generation photocatalysts. 2D materials have a large surface area, less recombination rate of photogenerated charge carriers, and tunability of electronic structure. The enhanced photocatalytic activity of 2D materials than that of the bulk counter part is

reported by experimental studies.

Single layers of ZnSe shown a photocurrent density of 2.14 mA/cm^2, which is 195 times higher than the bulk value of ZnSe. [59] Photocatalytic enhancements are observed in other few and single layer 2D WS_2. [60]

The 2D semiconductor should have some of the following properties to facilitate the photocatalytic water splitting. [61]

(a) **Low formation energy:** The low formation energy of 2D material than that of the bulk counterpart facilitates the easy extraction from the bulk.

(b) **Sufficient band gap:** Semiconductor should have band gap more than water Gibbs free energy (1.23 eV), and less than 3 eV to absorb visible light.

(c) **Band edges must align with water redox potentials:** Conduction band minimum (CBM) should be higher than the reduction potential of H^+/H_2 (-4.44) and valance band maximum should align lower than the oxidation potential of O_2/H_2O (-5.67)

(d) **Insoluble in water:** The semiconductor should not dissolve in aqueous solutions.

(e) **Ability to absorb visible light:** The 2D material should be able to absorb the wide range of the visible spectrum, as it accounts for around 40% of solar energy.

(f) **Small exciton binding energy:** As the exciton binding energy is small, excitons can split into charge carrier and facilitates the photocatalytic reactions.

(g) **Low recombination rate of excitons:** If the exciton recombination rate is low, photogenerated charge carriers can reach the surface and facilitates the corresponding redox reactions.

(h) **Low rate of backward reaction:** The backward reaction of water dissociation, where hydrogen and oxygen combine to form water. It is energetically favorable, it should be kinetically suppressed.

(i) **Passivation of edges:** Edges of the semiconducting material should be passivated, which can minimize the reaction of ions in the solution with the edges of the material.

(j) **Stable suspension in water:** Semiconductor must be dispersed in water and should not form agglomeration (cluster).

1.5.1 2D-graphitic nitride as photocatalyst

Graphitic carbon nitride is a polymeric semiconductor with a wide band gap about 2.7 eV. [62, 63] It can be synthesized from more abundant nitrogen and carbon precursors.

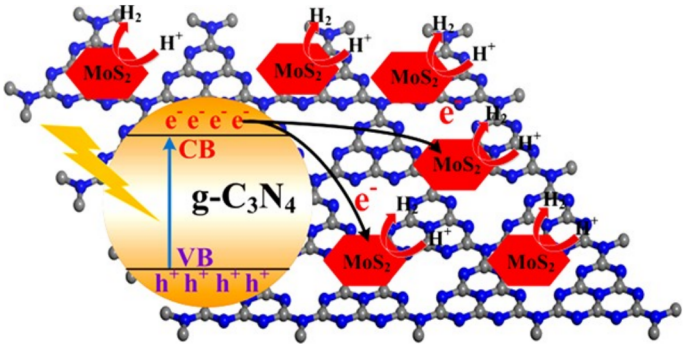

Figure 1.4: schematic image of heterojunction of g-C_3N_4/MoS_2. Figure adopted from reference, [64] with permission from the American Chemical Society.

Graphitic carbon nitride (g-C_3N_4) is investigated as a metal-free photocatalyst for solar hydrogen evolution. [65, 66] Wang et al first reported the g-C_3N_4 as photocatalyst for H_2 production. [63] It is a polymeric semiconductor, which can be synthesized from more abundant nitrogen and carbon precursors. g-C_3N_4 is ther-

mally and chemically stable, [67] not dissolved in acid, alkali, organic solvents, and robust under ambient conditions. [68, 69] g-C_3N_4 is composed of graphite like sp^2 hybridized C, N, and acts as a pi-conjugated electronic system. [70] g-C_3N_4 has a wide band gap about 2.7 eV [62, 63] and suitable for water redox reactions [63], but the efficiency is very poor. The reasons behind the low efficiency of g-C_3N_4 are wide band gap which limits blue light, low carrier mobility which leads to fast recombination of photo-excited carriers, the nature of covalent bonding in g-C_3N_4 lowers the active sites on the surface. [70] To enhance the efficiency of g-C_3N_4, various strategies applied such as doping with heteroatoms (B, C, F, P, O and S) [71–74], protonation [75], designing heterojunctions, and structure engineering like thin film/porous/ hollow/helical etc. [76–80] It is worth noted that using a co-catalyst can promote solar hydrogen evolution.

1.5.2 Transition Metal Dichalcogenides as photocatalysts

Transition metal dichalcogenides (TMDs), with formula MX_2 (M= transition metal; X= chalcogen) are being developed for photocatalytic water splitting. 2D (two-dimensional) TMDs exhibits unique physical, chemical, electronic properties compared to their bulk counterpart. [8, 10, 81–84] Each TMD layer consists of three layers as X-M-X, where intralayer has covalent bonding and weak vdW interaction exists between adjacent MX_2 layers. The MX_2 (M = Mo and W; X = S and Se) monolayers composed with M atom stays between two hexagonal planes of X atoms, where each M atom bonded with six neighboring X atoms through covalent bonds. [85] The band gap of TMD reduces as the thickness reduces from few-layers to monolayer, where the blue shift occurs in the absorption which leads into the visible light region.

Mo and W based dichalcogenides are reported as photocatalysts for water splitting. [86, 87] However, the photocatalytic efficiency is very poor because of the high

recombination rate of photo-generated electron-hole pair. [88, 89] TMDs act as co-catalysts for water splitting. [90–92] and some of the single layer TMDs reported as photocatalysts for water splitting. [93]

1.5.3 Phosphorene as a photocatalyst

Monolayer phosphorene is synthesized from black phosphorous by using sticky-tape method. [44] In phosphorene, P-atoms undergo sp^3 hybridization and forms 3-covalent bonds with neighboring P-atoms, and leaves one lone pair of electrons. Because of these lone pair electrons, phosphorous is very reactive.

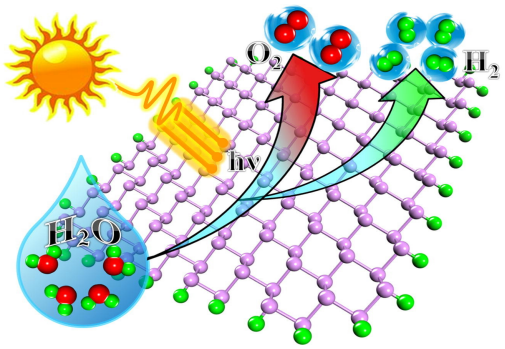

Figure 1.5: schematic image of photocatalytic water splitting on phosphorene. Figure adopted from reference, [94] with permission from Elsevier.

Black phosphorous is the stable allotrope of phosphorous. [95] Black phosphorous has a puckered honeycomb structure with orthorhombic lattice geometry. [96] The phosphorous atoms in the intralayer have covalent bonds and weak van der Waals forces exist between the adjacent phosphorene layers (interlayer).

Pure phosphorene monolayer is suitable for hydrogen evolution from water, but it can not catalyze the oxygen evolution from water. TiO_2/phosphorene [97], Au-particles on the phosphorene [98] show enhanced photocatalytic activity. Hydroxyl functionalized phosphorene nano-sheets exhibits enhanced photocatalytic hydrogen evolution. [99]

1.6 Outline of this work

Having discussed the many advantages of two-dimensional materials in the context of photocatalytic water splitting, here in this thesis, we investigate the optical properties of various two-dimensional materials. Within the first-principles calculations, we particularly investigate phosphorene, graphene nitride and transition-metal dichalcogenides; and exploit their derivates and van der Waals heterostructures in the context of photocatalysis. The thesis is organized as follows,

Chapter 2: In this chapter, starting from the many-body Hamiltonian, we briefly introduce the quantum chemical density functional theory, which is the workhorse of this thesis. Different exchange-correlation functional is described. We further provid an outline for the *GW* and BSE formalism that have been used to investigate the quasiparticle and optical spectra.

Chapter 3: We investigate the optical properties of phosphorene and its derivatives within the hybrid exchange-correlation functional and discuss the results in the context of photocatalytic water splitting. While pristine phosphorene is unstable in air and easily oxidizes, we exploit this feature to show that derivatives with N, O and S coverages are not only thermodynamically stable but also have correct band alignment necessary for photocatalysis along with high photo-absorption capability.

Chapter 4: In this chapter, we combine two extraordinary two-dimensional materials, graphitic carbon nitride g-C_3N_4 and Janus transition-metal dichalcogenides MoXY, in van der Walls heterostructures. We investigate the optical properties and investigate excitons within two-dimensional hydrogen model, which is benchmarked with the more accurate *GW*-BSE calculations. The results are discussed in the context of photocatalytic water splitting and the solar-to-hydrogen efficiency is calculated.

Chapter 5: Here we investigate the exciton binding energy in two-dimensional materials, which is fundamentally different from their bulk counterparts due to much weaker electron screening in the reduced dimension. We describe a tractable hydrogenic model where the parameters are calculated from the inexpensive and conventional DFT calculations that are benchmarked against the available experimental results and more accurate *GW*-BSE calculations. Within the presented methodology, the effects of strain in the lattice and impurities are investigated and as well as exciton renormalization is studied in thicker samples and in heterostructures.

Chapter 6: With the success of hydrogenic model discussed in the Chapter 5, in this chapter, we study the excitonic properties of Janus transition-metal dichalcogenides and compare the results with those using the *GW*-BSE formalism. Excellent agreement between these two approaches along with the available experimental results indicate the general applicability of the hydrogenic model for other two-dimensional materials.

Chapter 7: In this chapter, we summarize the results and contributions of this thesis and present further possibilities.

CHAPTER 2

METHODOLOGY

The quantum mechanical model of a condensed matter system is described by a collection of ion cores and itinerant valence electrons. However, the complexity arises from the various many-body interactions, and the general Hamiltonian for the interacting system can be written as,

$$\mathcal{H} = -\sum_I \frac{\hbar^2}{2M_I}\nabla_I^2 + \sum_i \frac{\hbar^2}{2m_i}\nabla_i^2 + \frac{1}{2}\sum_{I\neq J}\frac{Z_I Z_J e^2}{|\mathbf{R}_I - \mathbf{R}_J|} + \frac{1}{2}\sum_{i\neq j}\frac{e^2}{|\mathbf{r}_i - \mathbf{r}_j|} - \sum_{i,I}\frac{e^2 Z_I}{|\mathbf{R}_I - \mathbf{r}_i|}, \tag{2.1}$$

where $I(i)$ represents an ion (electron), $M(m)$ is the ion (electron) mass, $\mathbf{R}(\mathbf{r})$ is the position of ion (electron). The first two terms of the Hamiltonian describe the kinetic energy of ions and electrons, respectively. The third and fourth term represent the Coulomb interaction energy for ion-ion and electron-electron interaction while the electron-ion interaction is described by the final term. The relativistic corrections including the spin-orbit coupling is not considered. The solution of above system is given by the Schrödinger equation

$$\mathcal{H}\psi(\mathbf{r},\mathbf{R}) = E\psi(\mathbf{r},\mathbf{R}),$$

where ψ is the many-body wave function, and E is the eigenvalue of the system. However, a straightforward solution is not practical owing to a large $\sim 10^{23}$ quantum numbers, and therefore, approximate methods are necessary.

The ions including the nucleus are much heavier than the electrons ($M/m \sim 10^4$). The difference in mass and kinetic energy implies that the ions are signif-

icantly more sluggish than the electrons. Therefore, the electrons can react almost instantaneously to any ionic motion. Within this procedure called Born-Oppenheimer adiabatic approximation, [100, 101] the electronic and ionic degrees of freedoms are separated. It can be assumed that the electrons a system experience instantaneous potential produced by the ions that have spatially fixed positions. Therefore, the effective electronic Hamiltonian can be written as,

$$\mathcal{H} = \left[\sum_i \frac{\hbar^2}{2m_i}\nabla_i^2 - \sum_{i,I}\frac{e^2 Z_I}{|\mathbf{R}_I - \mathbf{r}_i|}\right] + \frac{1}{2}\sum_{i\neq j}\frac{e^2}{|\mathbf{r}_i - \mathbf{r}_j|} + V_{\text{ion}}, \tag{2.2}$$

where the first term describes the kinetic energy of electrons, the second term represents electron-electron interaction, the third term is the attractive Coulomb interaction among the electrons and static ions. The last term is additive energy for the ion-ion interaction calculated using the Born-Oppenheimer approximation. The electronic part represented in Eq.2.2 primarily determines the electronic structure of the system. The above Hamiltonian requires further *mean-field* simplification owing to the many-body electron-electron interactions.

In this regard, Hartree proposed that the many-body electronic wave function Φ can be written as a product of orthonormal one-electron wave functions φ, [102]

$$\Phi(\mathbf{r}_1, \mathbf{r}_2, \ldots, \mathbf{r}_N) = \varphi_1(\mathbf{r}_1)\varphi_k(\mathbf{r}_2)\ldots\varphi_N(\mathbf{r}_N) \equiv \prod_k \varphi_k(\mathbf{r}_k). \tag{2.3}$$

Here, one assumes that each electron moves in an average field created by the ions together with all the other electrons. Each one-electron wave function φ_k satisfies and independent Schrödinger equation,

$$\left[-\frac{\hbar^2}{2m}\nabla_k^2 + V(\mathbf{r})\right]\varphi_k(\mathbf{r}) + e^2\sum_{j(\neq k)}\int\frac{|\varphi_j(\mathbf{r}')|^2}{|\mathbf{r}-\mathbf{r}'|}d\mathbf{r}'\varphi_k(\mathbf{r}) = E_k\varphi_k(\mathbf{r}), \tag{2.4}$$

The corresponding total energy is then obtained by,

$$E = \sum_k E_k - \frac{e^2}{2} \int \int \frac{\rho_k(\mathbf{r})\rho_j(\mathbf{r}')}{|\mathbf{r} - \mathbf{r}'|} d\mathbf{r} d\mathbf{r}'.$$

The second term represents the doubly counted electron-electron interaction, known as the Hartree energy. Here, $\rho(\mathbf{r}) = |\varphi(\mathbf{r})|^2$ denotes the electron density. Within this approach, a self-consistent solution of the Hartree equation is obtained by variational approach, where the total energy is minimized with respect to the wave function or electron density. However, the Hartree wave function in Eq. 2.3 is quantum mechanically inconsistent for the electrons. The simple assumption in Eq. 2.3 is not compatible with the Pauli principle, since the fermionic wave function Φ must be antisymmetric and changes the sign when two particles are spatially interchanged. Moreover, the Hartree approximation does not incorporate exchange, correlation and screening.

To address the inconsistency, within the Hartree-Fock approximation the many-body wave function Φ is given by single Slater determinant of N single-particle spin-orbitals φ, [103]

$$\Phi = \frac{1}{\sqrt{N!}} \begin{vmatrix} \varphi_1(q_1) & \varphi_2(q_1) & \cdots & \varphi_N(q_1) \\ \varphi_1(q_2) & \varphi_2(q_2) & \cdots & \varphi_N(q_2) \\ \vdots & \vdots & \vdots & \vdots \\ \varphi_1(q_N) & \varphi_2(q_N) & \cdots & \varphi_N(q_N) \end{vmatrix} \tag{2.5}$$

Here q is a composite index for electronic coordinates and spin. This simple ansatz for the many-body wave function captures the Pauli exclusion principle. This wave function is used to calculate the total energy with varied orthonormal set of φ. The resulting one-electron equations resemble single-particle Schrödinger

equations, and the Hartree-Fock equation is given by, [104]

$$\left[-\frac{\hbar^2}{2m}\nabla_k^2 + V(\mathbf{r}) + e^2\sum_j \int \frac{|\varphi_j(\mathbf{r}')|^2}{|\mathbf{r}-\mathbf{r}'|}d\mathbf{r}'\right]\varphi_k(\mathbf{r}) \;-\; e^2\sum_j \int \frac{\varphi_j^*(\mathbf{r}')\varphi_k(\mathbf{r}')}{|\mathbf{r}-\mathbf{r}'|}d\mathbf{r}'\,\varphi_j(\mathbf{r}) = E_k\varphi_k(\mathbf{r}) \tag{2.6}$$

The first three terms are identical to those in Hartree equation, however, an additional exchange term appears owing to the inclusion of Pauli principle. Due to this exchange interaction, electrons of like-spin avoid each other and consequently surrounded by an *exchange hole*. While the Hartree-Fock approximation corresponds the conventional single-electron picture of electronic structure, by assuming the single determinant form for the wave function, it neglects electron correlation. Therefore, Hartree-Fock theory is insufficient to make accurate quantitative predictions, while it produces qualitatively correct results for many materials.

2.1 Density Functional Theory

The methods for solving the many-body Schrödinger equation based on the Slater determinant expansion of the wave function require a huge computational cost, which makes it virtually impossible to apply them to larger and more complex problems. The density functional theory (DFT) provides an attractive alternative, which maps the many-body problem with the electron-electron interaction onto a single-body problem without the interaction. DFT has its roots in Thomas-Fermi (TF) model of electronic structure, [105, 106] where the electron density $n(\mathbf{r})$ is the central variable instead of the wave function. The TF equation relates the ground-state electron density $n(\mathbf{r})$ with the external potential $V(\mathbf{r})$,

$$\frac{1}{2}(3\pi^2)^{2/3}n(\mathbf{r})^{2/3} + V(\mathbf{r}) + \int \frac{n(\mathbf{r}')}{|\mathbf{r}-\mathbf{r}'|}d\mathbf{r}' - \mu = 0, \tag{2.7}$$

where μ is the chemical potential. However, the TF suffers from many limitations, and it can not explain chemical bonding, since kinetic energy is crudely approximated. Further, the electron-electron interaction is classically approximated and the quantum phenomena like exchange interaction is completely neglected.

The modern DFT follows the TF model to use the density $n(\mathbf{r})$ as the basic variable to describe a quantum system. The mathematically rigorous Hohenberg-Kohn theorem states that the ground state density $n(\mathbf{r})$ of a bound system of interacting electrons in an external potential $v(\mathbf{r})$ determines this potential uniquely. The $n(\mathbf{r})$ implicitly determines all the properties derivable from the many-body Hamiltonian through the solution of Schrödinger equation. The kinetic and interaction energies are functional of density $n(\mathbf{r})$, and an universal functional $F[n(\mathbf{r})]$ can be defined as,

$$F[n(\mathbf{r})] = \langle \Psi | T[n(\mathbf{r})] + U[n(\mathbf{r})] | \Psi \rangle, \tag{2.8}$$

and the corresponding energy functional for a given external potential $v(\mathbf{r})$ is,

$$E_v[n(\mathbf{r})] = \int v(\mathbf{r}) n(\mathbf{r}) d\mathbf{r} + F[n(\mathbf{r})]. \tag{2.9}$$

According to the Hohenberg-Kohn variational theorem, [107] for every trial density function $n_{tr}(\mathbf{r})$ that satisfies the conditions, $\int n_{tr}(\mathbf{r}) d\mathbf{r} = N$ and $n_{tr}(\mathbf{r}) \geq 0$ for all $\mathbf{r}$, the inequality is $E_0 \leq E_v[n_{tr}]$. $E_0 = E_v[n_0]$ where n_0 is the true ground-state electron density. Here, the kinetic energy T is approximated by TF theory described earlier, which is severely inadequate and is the main source of error. This can largely remedied by the self-consistent Kohn- Sham approach.

2.1.1 The Kohn-Sham equation

Kohn-Sham approach maps the interacting many-body system onto a non-interacting system that generates the same density. The non-interacting electrons experience

a local effective external potential $V_{\text{eff}}(\mathbf{r})$, and are described by the single-particle Kohn-Sham equation,

$$\left[-\frac{\hbar^2}{2m}\nabla^2 + V_{\text{eff}}(\mathbf{r})\right]\varphi_i(\mathbf{r}) = \varepsilon_i\varphi_i(\mathbf{r}). \tag{2.10}$$

Here ε_i are the initial energies of the corresponding Kohn-Sham orbital φ_i and the density of the N-particle system is,

$$n(\mathbf{r}) = \sum_{i=1}^{N} |\varphi_i(\mathbf{r})|^2. \tag{2.11}$$

The total nergy of the system is expressed as,

$$E[n(\mathbf{r})] = T_s[n(\mathbf{r})] + \Delta T[n(\mathbf{r})] + E_H[n(\mathbf{r})] + E_X[n(\mathbf{r})] + \int v_{\text{ext}}(\mathbf{r})n(\mathbf{r})d\mathbf{r} \tag{2.12}$$

The kinetic energy is approximated to the ground-state of the non-interacting electrons, which is incomplete. The corresponding *error* is denoted as ΔT, which is the source of correlation energy. The electron-electron interaction energy is approximated at the Coulomb Hartree and quantum mechanical exchange energies, E_H and E_X, respectively. The last term is the interaction with the external potential.

The non-interacting kinetic energy is expressed as,

$$T_s[n(\mathbf{r})] = \sum_{i=1}^{n} \int \varphi^*(\mathbf{r}) \left[-\frac{\hbar^2}{2m}\nabla^2\right] \varphi_i(\mathbf{r})d\mathbf{r}, \tag{2.13}$$

and the Hartree energy is given by,

$$E_H[n] = \frac{e^2}{2}\int \frac{\rho(\mathbf{r})\rho(\mathbf{r}')}{|\mathbf{r}-\mathbf{r}'|}d\mathbf{r}d\mathbf{r}', \tag{2.14}$$

and the exchange-correlation energy is expressed as, $E_{XC}[n] = E_X[n] + \Delta T[n]$. The

V_{eff} is determined by varying the total energy with respect to the KS orbitals,

$$V_{\text{eff}}(\mathbf{r}) = v_{\text{ext}}(\mathbf{r}) + \int \frac{n(\mathbf{r}')}{|\mathbf{r} - \mathbf{r}'|} d\mathbf{r}' + \frac{\delta E_{XC}[n]}{\delta n(\mathbf{r})}, \tag{2.15}$$

where the last term is the exchange-correlation potential.

The corresponding ground state energy is given by,

$$E[n(\mathbf{r})] = \sum_i \varepsilon_i - \int v_{\text{ext}} n(\mathbf{r}) d\mathbf{r} + \frac{e^2}{2} \int \frac{n(\mathbf{r}) n(\mathbf{r}')}{|\mathbf{r} - \mathbf{r}'|} d\mathbf{r} d\mathbf{r}' + \int \frac{\delta E_{XC}[n]}{\delta n(\mathbf{r})} n(\mathbf{r}) d\mathbf{r} \tag{2.16}$$

Note that in the absence of exchange-correlation the KS equations reduces to the self-consistent Hartree equations.

2.1.2 Exchange-correlation functional

The KS formalism maps the fully interacting system onto an auxiliary non-interacting system that yields the same ground state density. However, KS kinetic energy is not the true kinetic energy. The exchange-correlation energy is expressed as,

$$E_{XC}[n(\mathbf{r})] = \Delta T[n(\mathbf{r})] + E_X[n(\mathbf{r})], \tag{2.17}$$

where $\Delta T[n(\mathbf{r})]$ is the kinetic energy difference between the exact and auxiliary non-interacting system, and $E_X[n(\mathbf{r})]$ is the many-body electron-electron and Hartree energies. The exchange-correlation term is interpreted as the *hole* that reduces the probability of finding an adjacent electron. While the Pauli exclusion principle is accounted here, it does not yet correct for the spurious interaction of electron with its own density (self-interaction).

2.1.3 Local density approximation (LDA)

Hohenberg and Kohn have shown that if the electron density $n(\mathbf{r})$ varies very slow with $\mathbf{r}$ then the $E_{XC}[n]$ is given by,

$$E_{XC}^{LDA}[n(\mathbf{r})] = \int n(\mathbf{r})\varepsilon_{XC}^{\mathrm{LDA}}[n(\mathbf{r})]dr, \tag{2.18}$$

Here $\varepsilon_{XC}^{LDA}[n]$ is the exchange plus correlation energy per electron, where the electron is in a homogeneous electron gas with electron density $n(\mathbf{r})$. The exchange part is $\varepsilon_{X}^{LDA}[n] = 3/4\pi(3\pi^2 n)^{1/3}$. The correlation part representations were given by Perdew and Wang, [108] and, Perdew and Zunger [109] can be used. We can use the earlier representations by Hedin and Lundquist, [110] and by Wigner. [111] The exchange-correlation potential comes from the derivative of E_{XC}^{LDA} within LDA,

$$\begin{aligned} v_{XC}^{\mathrm{LDA}} &= \frac{\delta E_{XC}^{\mathrm{LDA}}}{\delta n} && (2.19)\\ &= \varepsilon_{XC}[n(\mathbf{r})] + n(\mathbf{r})\frac{\partial \varepsilon_{XC}[n(\mathbf{r})]}{\partial n} && (2.20) \end{aligned}$$

2.1.4 Generalized gradient approximation (GGA)

Generalized gradient approximation (GGA) the function based on the density and the gradient,

$$E_{XC}^{\mathrm{GGA}}[n(\mathbf{r})] = \int n(\mathbf{r})\varepsilon_{XC}^{\mathrm{GGA}}[n(\mathbf{r}), |\nabla n(\mathbf{r})|]d\mathbf{r} \tag{2.21}$$

We can use the GGA functions by Perdew and Wang, [108] by Perdew, Burke and Ernzerhof (PBE). [112] In Cartesian coordinates, the exchange-correlation potential is given by,

$$v_{XC}^{GGA}[n(\mathbf{r})] = \left[\frac{\partial}{\partial n} - \sum_{i=1}^{3}\nabla_i \frac{\partial}{\partial \nabla_i n}\right] n(\mathbf{r}) E_{XC}^{\mathrm{GGA}}(n(\mathbf{r}), |\nabla n(\mathbf{r})|), \tag{2.22}$$

it depends on the first and second radial derivatives of the density.

2.1.5 Hybrid Functionals

Both LDA and GGA functionals underestimate the band gap, which can be overcome by hybrid functionals. Heyd, Scuseria, and Ernzerhof (HSE) [113–116] is an efficient screened hybrid functional. The HSE functional divides the Coulomb potential for exchange into long-range (LR) and short-range (SR) components

$$\frac{1}{r} = \frac{1 - erf(\omega r)}{r} + \frac{erf(\omega r)}{r}, \tag{2.23}$$

where, $\frac{1-erf(\omega r)}{r}$ indicates the short-range , and $\frac{erf(\omega r)}{r}$ is the long-range exchange. ω is the screening parameter, $\frac{1}{\omega}$ is the separation range. Now, the exchange-correlation energy is,

$$E_{XC}^{\mathrm{HSE}} = aE_X^{\mathrm{HF,SR}}(\omega) + (1-a)E_X^{\mathrm{PBE,SR}}(\omega) + E_X^{\mathrm{PBE,LR}}(\omega) + E_C^{\mathrm{PBE}}, \tag{2.24}$$

where, $E_X^{\mathrm{HF,SR}}$ is the short-range HF exchange, $E_X^{\mathrm{PBE,SR}}$, $E_X^{\mathrm{PBE,LR}}$ are the short-range and long-range components of the PBE exchange functional, and E_C^{PBE} is the PBE correlation energy. The parameter $a = 1/4$ is obtained from perturbation theory [117], which is HF mixing constant. HSE becomes PBE0, or PBEh, or PBE1PBE, for $\omega = 0$, and HSE is identical with PBE, for $\omega \to \infty$. The HSE version with $\omega_{\mathrm{HF}} = 0.15/\sqrt{2}$ and $\omega_{\mathrm{PBE}} = 0.15 \times 2^{1/3}$ referred as HSE03, $\omega_{\mathrm{HF}} = \omega_{\mathrm{PBE}}$ denoted as HSE06. The physical units of ω_{HF}, ω_{PBE} are Bohr^{-1} or Å^{-1}.

2.2 *GW* method

The theories described above are successful to predict the ground state properties, the drawback lies in calculating the quasiparticle energies and describing the

excited-state. [118–120] The *GW* approximation systematically derived from the many-body perturbation theory. [121] The form of the self-energy in the *GW* approximation is same as in the Hartree-Fock but the Coulomb interaction is dynamically screened, which is non-local and energy dependent. Therefore, *GW* approximation remedies the most serious deficiency of the HF method. The GW method can be described by the following eigenvalue equation, [122]

$$(T + V_{ext} + V_H)\varphi_{n\mathbf{k}}(\mathbf{r}) + \int d\mathbf{r}\Sigma(\mathbf{r}, \mathbf{r}', \omega = E_{n\mathbf{k}})\varphi_{n\mathbf{k}}(\mathbf{r}') = E_{n\mathbf{k}}\varphi_{n\mathbf{k}}(\mathbf{r}) \tag{2.25}$$

Here, T is the kinetic energy, V_{ext} is the external potential, V_H is the Hartree potential, $E_{n\mathbf{k}}$ is the quasiparticle energies with orbital $\varphi_{n\mathbf{k}}$. Here, in contrast to DFT, the exchange-correlation potential is replaced by the many-body self-energy Σ, and is obtained together with the Green's function G and screened Coulomb interaction W.

$$\begin{aligned} G(1,2) &= G_0(1,2) + \int d(3,4)G_0(1,3)\Sigma(3,4)G(4,2) && (2.26)\\ W(1,2) &= V(1,2) + \int d(3,4)V(1,3)\chi(3,4)W(4,2) && (2.27)\\ \Sigma(1,2) &= \int d(3,4)G(1,3)\Gamma(3,2;4)W(4,1), && (2.28) \end{aligned}$$

where,

$$\begin{aligned} \chi(1,2) &= \int d(3,4)G(1,3)G(4,1)\Gamma(3,4;2), \text{and} && (2.29)\\ \Gamma(1,2;3) &= \delta(1,2)\delta(1,3) + \int d(4,5,6,7)\frac{\delta\Sigma(1,2)}{\delta G(4,5)}G(4,6)G(7,5)\Gamma(6,7;3) && (2.30) \end{aligned}$$

Note the composite notation $1 = (\mathbf{r}_1, t_1)$, and V is the bare Coulomb potential. χ and Γ are irreducible polarizability and irreducible vertex functions, respectively. However, further approximations are necessary for real systems. Instead of the vertex function, bare vertex is used in *GW* approximation. The equations are

solved in reciprocal space in the frequency domain,

$$W_{GG'}(\mathbf{q},\omega) = [\delta_{GG'} - \chi_{GG'}(\mathbf{q},\omega)V_{GG'}(\mathbf{q})]^{-1}V_{GG'}(\mathbf{q}) \quad (2.31)$$

$$G_{GG'}(\mathbf{q},\omega) = [\delta_{GG'} - \Sigma_{GG'}(\mathbf{q},\omega)G^0_{GG'}(\mathbf{q})]^{-1}G^0_{GG'}(\mathbf{q}) \quad (2.32)$$

These equations are solved self-consistently, where the first iteration G^0 is the non-interacting Green's function,

$$G^0(\mathbf{r},\mathbf{r}',\omega) = \sum_{n\mathbf{k}} \frac{\varphi^{*0}_{n\mathbf{k}}(\mathbf{r})\varphi^0_{n\mathbf{k}}(\mathbf{r}')}{\omega - E^0_{n\mathbf{k}}}, \quad (2.33)$$

where $\varphi^0_{n\mathbf{k}}$ is a set of one-electron orbitals with $E^0_{n\mathbf{k}}$ energies. The GW approximation improved the quasiparticle energies relative to the LDA eigenvalues, due to screening which is absent in HF method.

2.3 Bethe-Salpeter Equation (BSE)

An exciton state $|S\rangle$ within the BSE formalism can be written as, [123]

$$|S\rangle = \sum_{\mathbf{k}} \sum_{v}^{\text{hole}} \sum_{c}^{\text{elec}} A^S_{vc\mathbf{k}} |vc\mathbf{k}\rangle; \quad (2.34)$$

where $|vc\mathbf{k}\rangle = \hat{a}^\dagger_{v\mathbf{k}}\hat{b}^\dagger_{c\mathbf{k}+\mathbf{q}}|0\rangle$ with $|0\rangle$ being the ground state, and $\hat{a}^\dagger(\hat{b}^\dagger)$ is hole (electron) creation operator. $\mathbf{q}$ is the momentum of the absorbed photon, and $A^S_{vc\mathbf{k}}$ are electron-hole amplitudes. The corresponding excitation energies E_S are determined via BSE, [124, 125]

$$\left(\epsilon^{\text{QP}}_{c\mathbf{k}+\mathbf{q}} - \epsilon^{\text{QP}}_{v\mathbf{k}}\right) A^S_{vc\mathbf{k}} + \sum_{v'c'\mathbf{k}'} A^S_{v'c'\mathbf{k}'}\langle vc\mathbf{k}|K^{eh}|v'c'\mathbf{k}'\rangle = E_S A^S_{vc\mathbf{k}}, \quad (2.35)$$

where ϵ^{QP} are quasiparticle energies, and K^{eh} is the electron-hole interaction. The imaginary part of the dielectric function $\varepsilon''(\omega)$ is calculated by the optical transition matrix element of the excitations.

Such a rigorous treatment within the many-body theory coupled with BSE scheme provides an excellent description of QP and optical gaps; and exciton binding, which all compare well with the experimental results.

CHAPTER 3

OPTICAL AND PHOTOCATALYTIC ACTIVITY OF PHOSPHORENE DERIVATIVES

In the context of two-dimensional metal-free photocatalyst, we investigate the electronic, optical and excitonic properties of phosphorene derivatives within the first-principles approach. While two-dimensional phosphorene does not catalyze the complete water splitting reactions, O, S, and N coverages improve the situation drastically, and become susceptible to catalyze the complete reaction at certain coverages. We find that for all these dopants, 0.25 - 0.5 ML coverages are thermodynamically more stable, and does not introduce midgap defect states and the composite systems remain semiconducting along with properly aligned valance and conduction bands. Further, within visible light excitation, the optical absorption remain very high 10^5 cm^{-1} in these composite systems, and the fundamental optical anisotropy of phosphorene remains intact. We also investigate the effect of layer thickness through bilayer phosphorene with oxygen coverages. Finally, we investigate the excitonic properties of these composite materials that are conducive to both redox re-actions. The present results will open up new avenues to take advantage of these metal-free phosphorene derivatives toward its outstanding potential in photocatalysis. These results are published in the Journal of Physical Chemistry C 122, 7194 (2018).

3.1 Introduction

Hydrogen is a promising energy carrier, which can be used along with oxygen in a fuel cell to convert chemical energy into electricity. [126] Although highly abundant, hydrogen occurs in chemical compounds such as hydrocarbons and water, which must be chemically transformed to produce H_2. Further, water splitting $H_2O = 1/2O_2 + H_2$ is an uphill reaction, and the change in Gibbs free energy is 237 kJ mol^{-1}, which according to Nernst equation corresponds to 1.23 eV per electron transfer. [127–129]

In the presence of light, semiconductors may catalyze the H_2O oxidation reaction if the incident photons have sufficient energy to generate electron-hole ($e - h$) pairs. While the hole participates in the oxidation reaction, $H_2O + 2h = 1/2O_2 + 2H^+$, the excited electron drives the consequent hydrogen reduction reaction $2H^+ + 2e = H_2$. Since the discovery of photocatalytic water splitting on TiO_2, numerous semiconducting materials have been proposed. [127–129] Materials that are in focus for the last 40 years consist of d^0 transition metals or the post transition metals with d^{10} electronic configuration along with the group VA and VIA ions. [127, 128, 130–135] However, the practical use of these materials are limited by their inability to absorb visible light, and fast recombination leading to insufficient quantum efficiency. Nanoscale materials with tuneable electronic structure have attracted enormous attention to improve performance. [136] For example, solar-to-hydrogen conversion efficiency is increased up to 16% for TiO_2 nanotubes, while that of the bulk rutile phase is only 2%. [137] Further, the two-dimensional materials pose several advantages due to their tuneable electronic and optical properties. Moreover, they maximize the active surface area, and reduce electron-hole recombination through minimizing the distance that the photogenerated carriers travel before reaching catalyst-water interface, where the reaction takes place. Re-

cent experiments corroborate these facts, and single to few layer SnS_2, ZnSe, WS_2, SnSe, and SnS show order-of-magnitude improvement in the efficiency compared to their bulk counterparts. [135, 138–140]

Metal-free photocatalysts are attracting more attention in recent times due to their corrosion free and non-toxic nature along with better processability. [141–143] The quantum efficiency for two-dimensional graphitic-C_3N_4 is found to be as high as 26.5% under visible light illumination with $\lambda > 395$ nm. [144] Another 2D material, phosphorene, has attracted enormous scrutiny due to its extraordinary electronic and optical properties; and envisioned in electronic, optoeletronic and spintronic applications. [145–149] Further, anisotropic band structure with high carrier mobility, tuneable quasiparticle gap between 0.3 to 2.2 eV, [145, 147, 150, 151] and excellent photon absorption ability in the ultraviolet, visible and near infrared region [152] indicate phosphorene to be a good photocatalyst and deserves concerted attention. [153] While pristine single layer phosphorene (SLP) has been found to be incapable of catalyzing the complete water decomposition reaction, under the influence of increased pH 8.0, the SLP is predicted to catalyze both the half-reactions. [154] Following these, phosphorene based heterostructures and composites have been investigated, and found to be a promising route to design new materials, which could prevent electron-hole recombination in addition to tuning the band edges. [154–156] While MoS_2/phosphorene and WS_2/phosphorene 2D heterostructures are not encouraging, [155, 156] TiO_2@phosphorene show increased photo-absorption in 250-1200 nm, and concurrent photocatalytic activity. [157] Further, Au-nanoparticle decorated on phosphorene show encouraging photocatalytic activity. [158]

However, due to the presence of lone-pair electrons, the single and few-layer phosphorene is not air-stable, and degrades via oxidation. [159, 160] A protective Al_2O_3 or PMMA coating is found to preserve the intrinsic properties, and ar e use-

ful for electronic and optoelectronic devices. [151, 159, 160] In contrast, here we utilize the reactive nature of phosphorene, and investigate the electronic and optical properties of surface absorbed O, N, and S in the context of photocatalysis. Indeed, it is reported recently that hydroxyl-functionalized black phosphorus nano-sheets are excellent photoca talyst for visible light ($\lambda > 420$ nm) H_2 evolution with better activity than graphitic-C_3N_4. [161] Here, we find that 0.25 – 0.5 ML coverages are thermodynamically most stable, and the band edges align to water redox potentials. Hydrogen electrodes are reference electrodes whose potentials mark the zero level for all redox half reactions in electrochemistry. NHE is constructed by immersing a platinum electrode into a solution of 1 N (normal concentration, for protons, 1 N = 1 M) protons and bubbling pure hydrogen gas through the solution at 1 atm pressure. Due to its ease of fabrication, NHE was used as the reference electrode in the early times of electrochemistry. Further, the absorption coefficient is found to be very high, 10^5 cm^{-1} in these derivatives. Finally, the excitonic properties are studied and discussed in the context of photocatalysis.

3.2 Computational Details

Calculations were based on the first-principles density functional theory within the projector augmented wave formalism, and the wave functions were expanded in the plane wave basis with 500 eV cutoff. [162–164] The exchange correlation energy was described with Perdew-Burke-Ernzerhof (PBE) functional form of generalized gradient approximation. [165] All the structures were fully optimized including volume until the force components were less than 0.01 eV/Å threshold. At least 15 Å of vacuum space was adopted along the z-axis to avoid the periodic interaction. The binding or adsorption energies of P_xX_y (X=O, N, S) were calculated by $E_a = \frac{1}{y}[E(P_xX_y) - E(P_x) - y\mu_X]$, where x and y are the number of P and X atoms

in cell used in the calculation. $E(P_xX_y)$ and $E(P_x)$ are the energies of SLP with and without X-adsorption, while μ_X is the chemical potential of X. Single atom adsorption was studied with a 4×3 supercell, and a 8×8×1 Γ-centred Monkhorst-Pack k-grid was used to sample the Brillouin-zone. [166] Energetics of the structures with varied X-coverage Θ (1, 0.5, 0.25, 0.125 and 0.0625 monolayer, ML) were studied with a 4×4 supercell, along with 8×8×1 k-grid. Further, the electronic structure is calculated within the computationally expensive Heyd-Scuseria-Ernzerhof (HSE06) hybrid exchange-correlation functional, [167, 168] and depending on the coverage a minimal (super)cell were used. For 1, 0.5, 0.33, 0.25, 0.125 and 0.0625 ML coverages, we used 1×1, 2×2, 2×3, 4×1, 4×2, and 4×4 supercell with commensurate k-meshes, 17×17×1, 8×8×1, 8×6×1, 4×17×1, 4×8×1, and 4×4×1, respectively. We incorporated the van der Waals interaction within DFT-D3 method along with Becke-Jonson damping during structural optimization. [169, 170]

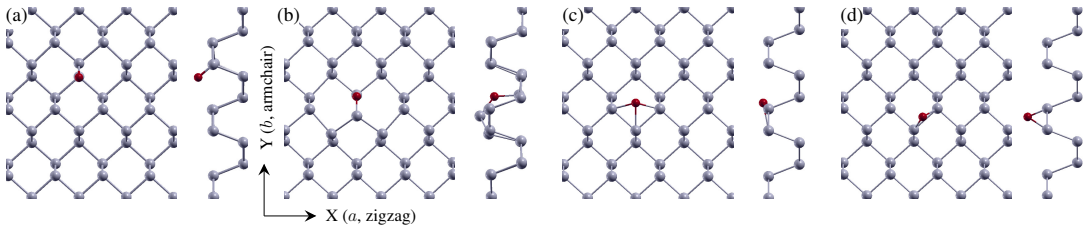

(e) Binding energies of single impurity

Absorption site	E_a (eV) O	S	N
Dangling	−5.68	−3.38	−4.06
Interstitial bridge	−5.14	−2.71	−3.52
Horizontal bridge	−3.70	−1.84	−3.47
Diagonal bridge	−3.59	−2.45	−3.71

Figure 3.1: Different adsorption sites on single layer phosphorene, (a) Dangling (b) interstitial bridge (c) horizontal bridge, and (d) diagonal bridge. (e) Binding energies of single impurity are tabulated, which indicate the dangling site adsorption to be preferable for all impurities. Bonding charge density is calculated as $\Delta\rho(r) = \rho_{SLP+X}(r) - \rho_{SLP}(r) - \rho_X(r)$, and are shown in (f), (g), and (h) for O, S, and N, respectively. Blue (red) color indicate electron depletion (accumulation). The charge densities are shown for 0.05 $e/Å^3$ isodensity. Bader population analysis of the charge density indicate P→X charge transfer (CT), and the impurity bonding is linearly correlated with the charge transfer.

In the context of photocatalysis the energy positions of the valence band maximum (VBM) and the conduction band minimum (CBM) are the key. To efficiently use the photogenerated electrons and holes, the CBM should be higher (more positive) than the H^+/H_2 reduction potential, and the VBM should be lower (more negative) than the oxidation potential of O_2/H_2O. These are -4.44 and -5.67 eV, respectively, with respect to the absolute vacuum level. Alternately, the water redox potentials are referenced with respect to the normal hydrogen electrode (NHE), H^+/H_2 to 0.0 eV and O_2/H_2O to 1.23 eV. The standard approach was employed to reposition the band edges with respect to the vacuum level $V(\infty)$, which is the electrostatic potential in the vacuum region far from the 2D material.

3.3 Results and Discussion

We begin our discussion with pristine SLP in the photocatalytic context. SLP has a puckered honeycomb structure resulting from covalently bonded sp^3 phosphorus atoms along with a pair of lone-pair electrons. The quasiparticle gap is experimentally measured to be in $2.05-2.20$ eV range through scanning tunnelling spectroscopy and photo-luminescence excitation spectroscopy. [151, 171] While it is known that the conventional exchange-correlational functionals underestimate the gap (PBE: 0.95 eV), [149] the HSE06 hybrid functional (1.4 – 1.7 eV)[150, 172, 173] and many-body perturbation based GW (2.00 – 2.25)[174, 175] calculations improve the results. As the GW calculations are computationally very expensive for the systems that we have investigated in this paper, we resort to HSE06 functional throughout the present investigation for electronic structure. The PBE-D3 optimized lattice parameters, a (zigzag) = 3.29 Å and b (armchair) = 4.45 Å compare well with the bulk black phosphorous. [176] The calculated HSE06 gap of 1.41 eV is in agreement with the previous calculations. [150] While the CBM of pristine

SLP is more negative than H^+/H_2 redox potential, the VBM is not more positive than O_2/H_2O oxidation potential (1.23 eV with respect to NHE). Thus, at ambient conditions, SLP is capable of catalyzing only half of the reaction, while in alkaline medium it catalyzes both the half-reactions. These results are in agreement with a previous report, which also indicate that strain engineering may improve the photocatalytic properties. [154]

3.3.1 Isolated impurities

Next we investigate the adsorption O, S, and N with SLP, which naturally reacts with these impurities due to the presence of lone-pair electrons. Possible adsorption sites are shown in Figure 3.1(a)-(d). These impurities are chemisorbed on SLP with strong binding energies [Figure 3.1(e)], and are absorbed in a dangling configuration [Figure 3.1(a)]. Absorbed oxygen bonds with a single phosphorus atom with a short P−O bond of 1.51 Å and very strong binding energy of -5.68 eV. According to Pauling electronegativity of P and O atoms, the P−O is polar covalent, which is evident from the bonding charge density and Bader population analysis [Figure 3.1(f)], which indicate a large P $\rightarrow$ O charge transfer of 1.31e. These results are in agreement with an earlier report. [177] The O adsorption at the interstitial bridge site with P−O−P bond is a metastable configuration with 0.54 eV higher energy. Here O lies between the two half-layers forming two P−O bonds, 1.65 and 1.69 Å and 130° P−O−P bond angle. The overall results are in agreement with recent X-ray photoemission spectroscopic measurement, which indicates the abundance of P−O bonds over P−O−P bonds. [161]

3.3.2 Impurity coverage

Having discussed the individual impurity adsorption, we now turn our attention to impurity coverage $\Theta \leqslant 1$ ML, and investigate their electronic structure, band

alignment and optical properties. First, we calculate the binding energy with varied impurity coverage, which is a tricky task as there might be several possible configurations for a particular coverage. Here, we consider only one sided adsorption, as if the SLP is placed on a non-interacting substrate. Impurities are chemisorbed at the most stable dangling site [Figure 3.1(e)]. Representative configurations for different coverages are shown in Figure 3.2(a)-(d) for $\Theta = 0.25$, 0.5 and 1 ML. Apart from the chemical interaction between the impurity and SLP, the impurity binding energy will be affected by varied coverage through Coulomb interaction between the impurities, and the strain developed in the SLP lattice due to impurity loading.

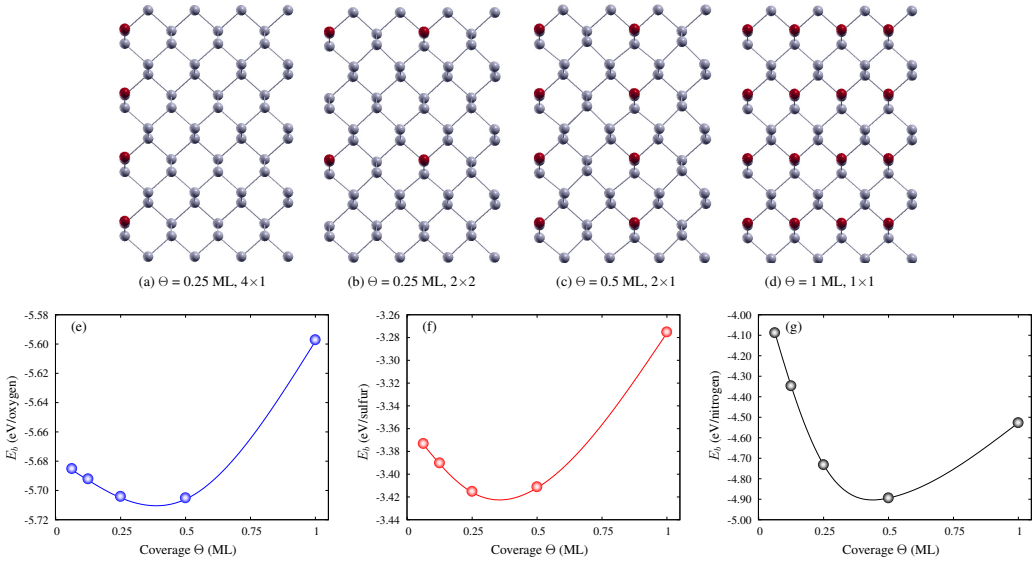

Figure 3.2: Representative configurations for impurity coverages shown for oxygen and sulfur, (a) $\Theta = 0.25$ ML – 4×1, (b) $\Theta = 0.25$ ML – 2×2, (c) $\Theta = 0.5$ ML – 2×1, and (d) $\Theta = 1$ ML – 1×1. Impurities are absorbed at the dangling site. (e)-(g) Calculated binding energy with varied impurity coverage $\Theta \leqslant 1$. Regardless the impurity type, the optimal coverage is found in the 0.25 – 0.5 ML range, which optimize the impurity–phosphorene bonding, Coulomb interaction between the impurities and the induced strain in SLP lattice.

Table 3.1: Structural details for SLP due to varied oxygen coverage, lattice parameters and P–O distance. Various configurations were considered for a particular coverage, and O is absorbed at the most preferable dangling site.

O-coverage & configuration	*a* (Å)	*b* (Å)	P–O (Å)
0.0625 ML (4×4)	3.29	4.45	1.51
0.125 ML (4×2)	3.29	4.46	1.51
0.125 ML (2×4)	3.29	4.46	1.51
0.25 ML (4×1)	3.29	4.47	1.51
0.25 ML (1×4)	3.30	4.46	1.50
0.25 ML (2×2)	3.29	4.48	1.51
0.5 ML (2×1)	3.30	4.49	1.51
0.5 ML (1×2)	3.31	4.47	1.50
0.5 ML c(2×2)	3.29	4.52	1.51
1 ML (1×1)	3.32	4.57	1.51

We have tabulated the structural parameters in Table 3.1, such as lattice parameters, and P-O bondlengths with varied oxygen coverage on SLP. The P-O bondlengths are not varying much with varied oxygen coverage. The lattice constant a is not ultered with varied oxygen coverages, but the lattice constant b increases as the oxygen coverage increases.

There is different configurations of impurity on phosphorene, which are not photocatalytically active are shown in the Figure 3.3. We did analysis of possible configurations for each coverage, with different impurity atoms . We observed that 0.5ML coverage has 3 differnt configurations, such as 2×1, 1×2, and c(2×2). Similarly , for 0.25 ML coverage is represented by 4×1, 1×4, 2×2 configurations, and 0.125ML coverage has 4×2, and 2×4 configurations.

To further investigate the dynamical stability of SLP under impurity coverage, we have investigated the phonon dispersion with in the density functional perturbation theory using the Phonopy code. [178, 179] For example, we calculated the phonon band structure and density of states (DOS) for SLP with 0.33 and 0.5 ML oxygen coverage, which are shown in Figure 3.4. The absence of any imaginary

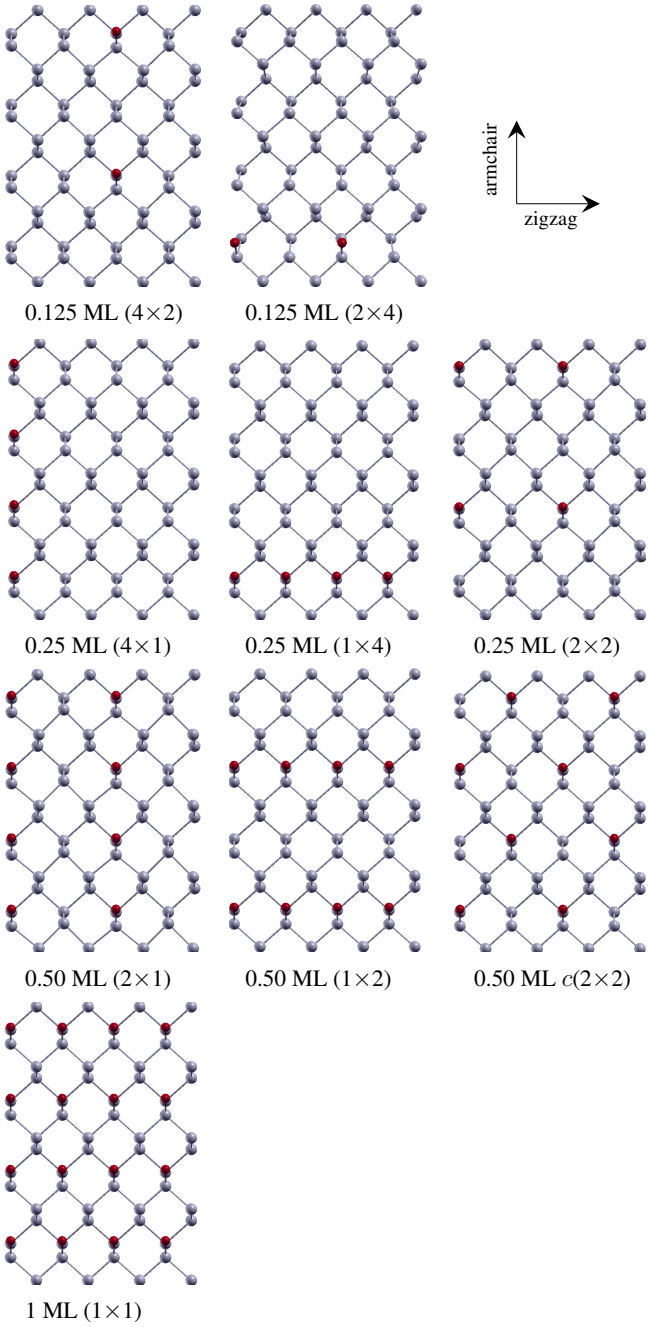

Figure 3.3: Possible configurations for adatom adsorption with varied coverage .

phonon mode indicates that the SLP under varied impurity coverages are indeed dynamically stable .

The picture is qualitatively similar for sulfur, and the binding is maximum for 0.25 – 0.5 ML coverage [Figure 3.2(f)]. For 0.25 ML sulfur, the 2×2 configuration

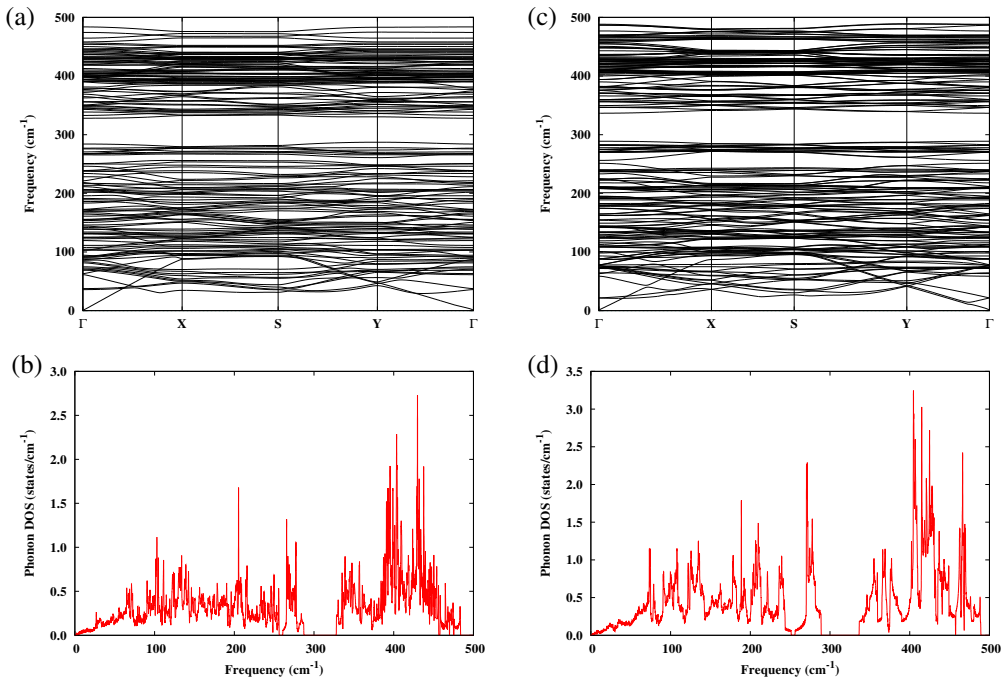

Figure 3.4: Calculated phonon band structure and phonon density of states for (a, b) 0.33 ML and (c, d) 0.5 ML oxygen coverage in their ground state. The absence of any imaginary phonon mode indicate that the SLP with impurity coverage are indeed dynamically stable.

is preferred, while the competing 4×1 is 26 meV/S higher. With increasing coverage at 0.5 ML, the 2×1 configuration is the ground state, which is 35 meV/S lower in energy than the corresponding $c(2\times2)$ configuration. Beyond 0.5 ML coverage, sulfur binding decreases rapidly. The change in P−S bond length and a do not show any noticeable change till 0.5 ML coverage, whereas b increases monotonically by 4.3% . However, at 1 ML coverage, the P−S bonds are increased by 0.05 Å, while a and b lattice parameters are increased by 2.9 and 6.7%, respectively, compared to pristine SLP. Thus, induced strain is larger for sulfur compared to oxygen coverage.

The structural analysis of S-coverage on SLP is tabulated [Table 3.2], the P-S bondlength is varied from 1.96 to 2.0 Å for 0.0625 to 1ML coverage . The lattice constant a is varied from 3.29 to 3.39 Å for 0.0625 to 1ML coverage, while b is

Table 3.2: Structural details for SLP due to varied sulfur coverage, lattice parameters and P-S distance. Various configurations were considered for a particular coverage, and S is absorbed at the most preferable dangling site.

S-coverage & configuration	*a* (Å)	*b* (Å)	P–S (Å)
0.0625 ML (4×4)	3.29	4.47	1.96
0.125 ML (4×2)	3.29	4.50	1.96
0.125 ML (2×4)	3.29	4.49	1.95
0.25 ML (4×1)	3.28	4.55	1.96
0.25 ML (1×4)	3.31	4.48	1.94
0.25 ML (2×2)	3.28	4.55	1.96
0.5 ML (2×1)	3.28	4.64	1.96
0.5 ML (1×2)	3.34	4.50	1.94
0.5 ML c(2×2)	3.27	4.72	1.99
1 ML (1×1)	3.39	4.75	2.00

varied from 4.47 to 4.75 Å for 0.0625 to 1ML coverage.

The structural parameters of N-coverage on SLP is analyzed (Table 3.3), where the lattice constant a is increased from 3.30 to 3.41 Å for 0.0625 to 1 ML coverage of N on SLP, respectively. The lattice constant b is reduced from 4.41 to 4.21 Å for 0.0625 to 1ML coverage of N on SLP, respectively.

Table 3.3: Structural details for SLP due to varied nitrogen coverage, lattice parameters and P-N distance. Various configurations were considered for a particular coverage, and N is absorbed at the most preferable dangling site.

N-coverage & configuration	*a* (Å)	*b* (Å)	P–N (Å)
0.0625 ML (4×4)	3.30	4.41	1.62, 1.68
0.125 ML (4×2)	3.30	4.37	1.60, 1.71
0.125 ML (2×4)	3.30	4.39	1.60, 1.69
0.25 ML (4×1)	3.33	4.24	1.63, 1.66
0.25 ML (1×4)	3.30	4.37	1.60, 1.67
0.25 ML dia-(4×1)	3.34	4.49	1.61, 1.68
0.25 ML (2×2)	3.38	4.18	1.60, 1.70
0.5 ML (2×1)	3.36	4.22	1.62, 1.66
0.5 ML (1×2)	3.34	4.29	1.61, 1.67
0.5 ML c(2×2)	3.35	4.25	1.63, 1.65
1 ML (1×1)	3.41	4.21	1.63, 1.66

The binding energy is found to be maximum around 0.5 ML N-coverage [Figure 3.2(g)]. For 0.5 ML coverage, the 2×1 configura tion is found to be the most stable over other configurations with binding energy 23 meV and 340 meV/N lower than the $c(2 \times 2)$ and 1×2 configurations, respectively. Beyond 0.5 ML coverage, E_b decreases much rapidly with varied coverage unlike oxygen and sulfur. Compared to 0.5 ML coverage, the calculated E_b increases by 367 and 547 meV/N for 1 ML and 0.125 ML coverages, respectively. In contrast, such increase is found to be much smaller (below 150 meV/dopant) for O and S coverages [Figure 3.2(e)-(g)]. We argue this feature to be connected to the lattice strain developed due to N-loading, which we notice to be much different from the cases with O and S doping, where only a tensile strain is developed in both zigzag and armchair direction. In contrast, a tensile and a concurrent compressive strains are developed along zigzag and armchair directions, respectively, which monotonically increases with increasing coverage. For 1ML N-coverage, the SLP lattice parameters increase by 3.7% (tensile strain) along the zigzag direction, while the same decreases by 5.3% (compressive strain) along the armchair direction, which can be observed in Table 3.3.

It would be interesting to investigate the differential effects of induced strain on the impurity binding. It is known that due to puckered nature along the armchair direction, the SLP can easily accommodate large strain along this direction, while the zigzag direction is relatively stiffer. [180] In this regard, we have calculated the strain energy relative to the pristine SLP, $\mathcal{E}_s = [E'(\text{SLP}) - E(\text{SLP})]/\text{area}$, where E and E' are the energies of pristine and distorted SLP due to impurity loading. Calculate strain energy increases monotonically with impurity loading, and is much smaller compared the corresponding impurity binding energy. For any coverage, we find $\mathcal{E}_s^{\text{O}} < \mathcal{E}_s^{\text{S}} < \mathcal{E}_s^{\text{N}}$, which is commensurate with the respective changes in their lattice parameters due to impurity adsorption. For example, while $\mathcal{E}_s$ is com-

parable for Θ= 0.5 ML O and S coverages (75 and 105 mJ/m^2, respectively), the same for N-coverage is much larger to 570 mJ/m^2. Furthermore, it is found that impurities repel each other due to Coulomb interaction while the separation fall below a 4 Å distance, and consequently binding energy decreases.

Table 3.4: Calculated strain energy due to impurity loading.

Coverage	Strain Energy $\mathcal{E}_s$ (mJ/m^2)		
	Oxygen	Sulfur	Nitrogen
0.0625 ML	7.92	12.40	47.34
0.125 ML	16.83	26.45	154.29
0.25 ML	37.14	59.06	458.46
0.5 ML	74.08	106.32	569.54
1 ML	161.70	536.56	703.25

The strain induced due to the dopant coverages on SLP, where the strain energy is enhanced as the dopant coverage is increased. Table 3.4 shows that nitrogen is inducing more strain than that of oxygen and sulfur, while oxygen is inducing less strain than the sulfur, and nitrogen.

3.3.3 Electronic structure and band alignment

The band structure of pristine SLP has been studied extensively in literature using various theoretical hierarchy and accuracy, [149, 150, 172–175] and the optical and quasiparticle gaps have been experimentally estimated. [151, 171] As conventional exchange-correlation functionals underestimate the band gap, we use hybrid HSE06 functional throughout the paper. Further, magnitude of the gap, and the corresponding energy positions of VBM and CBM are necessary for photocatalytic applications. In this context, as we have discussed earlier, pristine SLP catalyze only the H^+/H_2 half of the water oxidation, while O_2/H_2O reaction is not possible due to improper energy position of VBM (Figure 3.5). The calculated gap of 1.41 eV is in good agreement with the previous calculations within similar

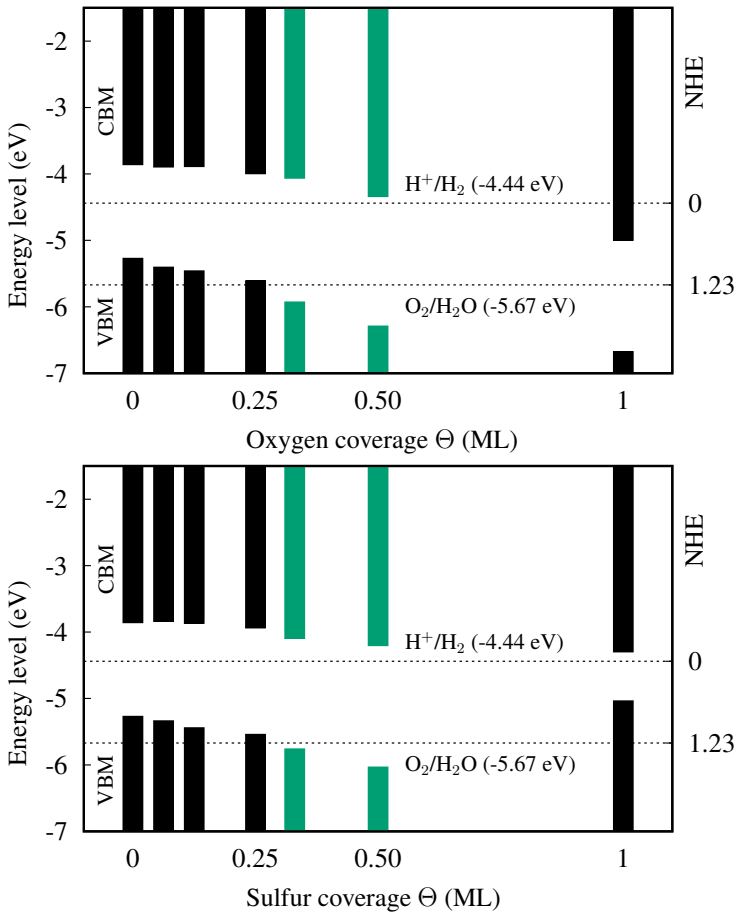

Figure 3.5: Band-edge positions of single layer phosphorene with varied oxygen and sulfur coverage at ambient conditions. These are calculated with hybrid HSE06 exchange-correlation functional and rescaled to the vacuum level and NHE. The redox potentials of H_2O is marked with the dashed lines. The band-edge positions for SLP with 0.33 and 0.5 ML oxygen and sulfur coverages are such that they catalyze both the half reactions.

theoretical hierarchy. [150, 172, 173] Here, we investigate to tune the gap and the corresponding VBM/CBM alignment with varied adatom coverages $\Theta \leq 1$ ML.

We start discussion with varied oxygen coverage, which does not introduce any electronic states in the gap and the composite system remain semiconducting. Calculated gap shows an overall non-monotonous variation. With increasing oxygen coverage, the gap first increases monotonously to 1.95 eV for 0.5 ML coverage, however which decreases to 1.68 eV for 1 ML oxygen. It is evident from the density

of states (DOS) that both VBM and CBM originate from the P-p_z orbital for pristine SLP, and this picture remains unperturbed with increasing oxygen coverage till 0.5 ML. We do not observe any contribution from oxygen to the band edges. However, for 1 ML coverage, hybridizied P-p_y and O-p_y contribution is observed in addition to P-p_z orbital at the valence band edge. Furthermore, the conduction band edge completely changes its character to P-p_x.

With increasing coverage, the band edges come down in energy (Figure 3.5) and the band-edge positions are such that for 0.33 and 0.5 ML become susceptible to catalyze both the water oxidation reactions. We have further investigated the oxidizing power $\Delta_{\mathrm{VBM}} = (E_{\mathrm{VBM}} + 5.67)$ eV, and reducing power $\Delta_{\mathrm{CBM}} = (E_{\mathrm{CBM}} + 4.44)$ eV. This is the energy measure of how negative (positive) the VBM (CBM) lies with respect to the respective redox potential. A large difference between Δ_{VBM} and Δ_{CBM} imbalances the oxidation and reduction reactions, which inhibit further redox reaction. Thus, similar Δ_{VBM} and Δ_{CBM} is required for overall catalytic efficiency. In this context, the SLP with 0.33 ML coverage ($\Delta_{\mathrm{VBM}} = -0.26$ eV and $\Delta_{\mathrm{CBM}} = 0.38$ eV) is expected to be a better catalyst than that with 0.5 ML coverage ($\Delta_{\mathrm{VBM}} = -0.62$ eV and $\Delta_{\mathrm{CBM}} = 0.10$ eV). The case with 0.25 ML coverage is interesting. While the VBM is unfavorable with being slightly positive (0.06 eV) compared to the oxidation potential, the CBM shows preferable alignment. However, increased pH of the solution will align the VBM in this case, as the redox potentials shift higher in energy by pH$\times$0.059 eV. [181] Thus, in a moderate pH 5 solution, both VBM and CBM align preferably with equivalent $\Delta_{\mathrm{VBM}} = -0.24$ eV and $\Delta_{\mathrm{CBM}} = 0.15$ eV, which indicate a balanced redox reactions. Although coverages below 0.25 ML are not thermodynamically preferable [Figure 3.2(e)], at moderate pH 5, structures with 0.0625 ML ($\Delta_{\mathrm{VBM}} = -0.03$ eV and $\Delta_{\mathrm{CBM}} = 0.25$ eV) and 0.125 ML ($\Delta_{\mathrm{VBM}} = -0.08$ eV and $\Delta_{\mathrm{CBM}} = 0.26$ eV) O-coverages are favourable to redox reactions.

It should be important to note that during the oxidation process, the O_2 molecule is physisorbed on the surface of phosphorene first, and then O_2 decomposition takes place. [177, 182] In such case, O-atoms can occupy the adjacent adsorption sites, which we investigate here. There are two possible ways in which two O-atoms can be absorbed at the adjacent adsorption sites in *trans* and *cis* configurations, which are shown in Figure 3.6.

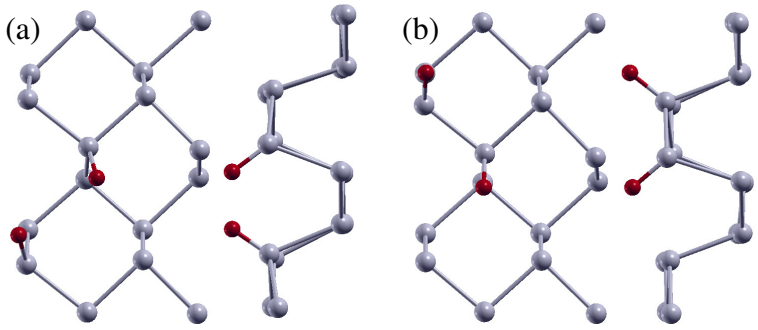

Figure 3.6: Oxygen atoms may occupy the adjacent adsorption sites on SLP, (a) trans configuration and (b)cis configuration. Although these configurations have slightly lower binding energy, these configurations may present as during the oxidation molecular O_2 is physisorbed before decomposition.

Here we investigate the 0.5 ML O-coverage as a test case to find that adsorption in *trans* configuration is comparatively more favourable than the *cis* configuration with -5.61 eV/O-atom binding energy. However, these binding energies are slightly lower than the 2×1 configuration which is found to be the ground state. Interestingly, compared to the ground state configuration, the calculated band gap, VBM, CBM, and work function are not significantly affected while the oxygen atoms are absorbed in these configurations, which are presented in Table 3.5 . Further, in these two configurations, the VBM and CBM align such that they are susceptible to catalyze the complete redox reaction, with $\Delta_{\mathrm{VBM}} = -0.54$ eV and $\Delta_{\mathrm{CBM}} = 0.24$ eV for the *trans* configuration, and $\Delta_{\mathrm{VBM}} = -0.49$ eV and $\Delta_{\mathrm{CBM}} = 0.21$ eV for the *cis* configuration.

Next we discuss oxygen coverage on bilayer phosphorene (BLP), for which we

Table 3.5: Calculated binding energy E_b , P–O distance, band gap E_g and the corresponding VBM and CBM, Δ_{VBM} and Δ_{CBM}, and work function φ for different configurations for 0.5 ML oxygen coverage.

	Configuration		
	2×1 groundstate	*trans*-configuration	*cis*-configuration
E_b (eV)	-5.71	-5.61	-5.54
P–O distance (Å)	1.51	1.50	1.50
E_g (eV)	1.95	2.01	1.93
VBM (eV)	-6.29	-6.21	-6.16
CBM (eV)	-4.34	-4.20	-4.23
Δ_{VBM} (eV)	-0.62	-0.54	-0.49
Δ_{CBM} (eV)	0.10	0.24	0.21
φ (eV)	5.84	5.79	7.73

consider the natural AB stacking that is energetically favorable. Calculated lattice parameters, within the PBE-D3 functional, are 3.30 and 4.33 Å along the zigzag and armchair directions, respectively. Calculated interlayer distance of 5.11 Å is in good agreement with previous quantum Monte Carlo results. [183] Here we have considered one-sided oxygen coverage only. While the lattice parameter along the zigzag direction is not perturbed by O coverage, the same along the armchair direction monotonically increases to 4.48 Å for 1ML coverage. The calculated binding energy with varied coverage show the same qualitative trend as discussed for the SLP [Figure 3.2(e)], while the binding is about 50 meV higher in case of BLP. The dangling d_{P-O} does not change upon increasing O loading, which remain at 1.51 Å.

The lattice parameters, and P-O bondlengths are tabulated in Table 3.6. The lattice constant(a) along zigzag direction is not altered as the oxygen coverage increases, while the lattice constant(b) along armchair direction increases from 0.25 ML to 1 ML coverage of oxygen on BLP. The P-O bondlength is constant, which does not depend on the oxygen coverage.

Compared to pristine SLP, the band gap decreases in pristine BLP to 1.10 eV,

Table 3.6: Structural details for BLP due to varied oxygen coverage, lattice parameters and P–O distance. The most stable configurations were considered for a particular coverage, and O is absorbed at the most preferable dangling site.

O-coverage & configuration	a (Å)	b (Å)	P–O (Å)
0.125 ML (2×4)	3.30	4.34	1.51
0.25 ML (2×2)	3.30	4.34	1.51
0.5 ML (1×2)	3.30	4.40	1.51
1 ML (1×1)	3.30	4.48	1.51

calculated within hybrid HSE06 functional, which is in good agreement with the previous reports. [150, 184] The trend in band gap with increasing O coverage for BLP shows similar qualitative trend as it is discussed for SLP earlier . The gap increases with increasing coverage till 0.5 ML to 1.44 eV, however, it decreases with further increase in coverage (1.32 eV for 1 ML). Similar to the trend observed in SLP, the band edges come down in energy with increasing coverage, and the BLP with 0.5 ML oxygen coverage becomes capable to catalyze both redox reactions with balanced oxidizing and reducing power ($\Delta_{VBM} = -0.09$ eV and $\Delta_{CBM} = 0.08$ eV). Note that for $\Theta \leqslant 0.25$ ML coverage, BLP catalyzes only one half of the complete reaction, H^+/H_2. However, for 0.25 ML O-coverage, BLP is predicted to catalyze both the half reactions at a moderate pH 4 solution ($\Delta_{VBM} = -0.08$ eV and $\Delta_{CBM} = 0.09$ eV).

We have studied the photocatalytic activity of bilayer phosphorene(BLP) with various coverages of oxygen atom. BLP with 0.5ML coverage of oxygen is oberved as suitable for water redox reactions. Figure 3.7 represents that pristine BLP, 0.125, 0.25 ML coverage of oxygen is feasible for water reduction, and 1ML coverage of oxygen on BLP is good for water oxidation reaction.

Motivated by our results with oxygen coverage, we have further investigated the role of sulfur. The calculated binding energy is maximum for 0.25–0.5 ML sulfur coverage, as we have discussed earlier [Figure 3.2(f)]. Similar to the trend

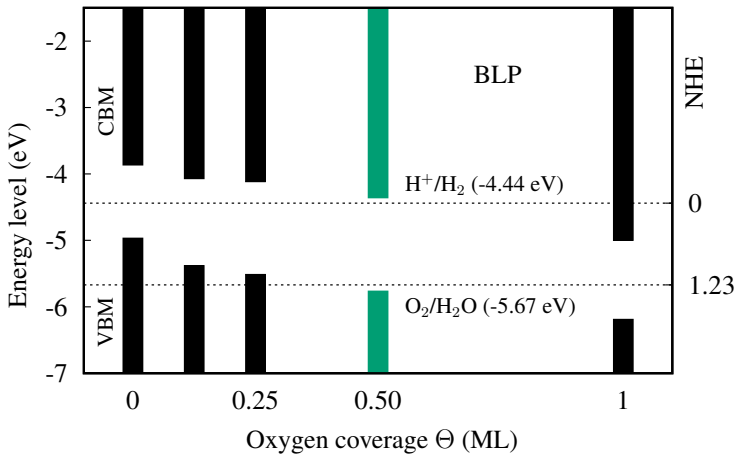

Figure 3.7: Band-edge positions of bilayer phosphorene (BLP) with varied oxygen coverage at ambient condition, calculated within the hybrid HSE06 exchange-correlation functional. The energies are rescaled to the vacuum level and NHE. Results are compared with the pristine BLP.

observed for oxygen coverage, absorbed sulfur does not introduce any midgap states at any coverage ≤ 1 ML that are studied here, and the composite systems remain semiconducting (Figure 3.5). The calculated gap monotonically increases with increasing coverage, 1.5 eV for 0.0625 ML to 1.83 eV for 0.5 ML coverage. However, the calculated gap for 1 ML coverage is severely reduced to 0.74 eV. Interestingly, we find for 0.33 and 0.5 ML sulfur coverages, the band edges align such that these systems become catalytically active. The corresponding oxidation and reduction powers are found to be $\Delta_{\mathrm{VBM}} = -0.09$ eV and $\Delta_{\mathrm{CBM}} = 0.35$ eV for 0.33 ML coverage, and the same for 0.5 ML are -0.36 and 0.24 eV, respectively. In contrast, the structures with 0.125 ML ($\Delta_{\mathrm{VBM}} = -0.07$ eV and $\Delta_{\mathrm{CBM}} = 0.28$ eV) and 0.25 ML ($\Delta_{\mathrm{VBM}} = -0.17$ eV and $\Delta_{\mathrm{CBM}} = 0.21$ eV) S-coverages become favourable to redox reactions at moderate pH 5 only.

The downward shift in band edges after O/S coverage is crucial for phosphorene to exhibit photocatalytic activity (Figure 3.5). The shift originate from the change in electron environment at the vacuum-phosphorene interface. [185] Due to P$\rightarrow$O/S charge transfer, O and S have surplus electron, and the electron-rich

environment at the surface induces a dipole that leads to altered band alignment with respect to the vacuum. Further, the work function φ, which is the energy difference between the vacuum level $V(\infty)$ and the Fermi energy, show monotonic increase with increasing O/S coverage. This is again due to the dipole formation between SLP and O/S impurity. Calculated φ for SLP, 0.0625, 0.125, 0.25, 0.33, 0.5, 1 ML O-coverages are 4.86, 4.93, 5.07, 5.10, 5.50, 5.84 and 6.28 eV, respectively, whereas φ monotonically increases to 5.65 eV for 0.5 ML S-coverage. Such tuneable work function by impurity coverage will have desirable impact on functional device applications.

Next we investigate nitrogen coverage on SLP, and find that the composite system with $\sim$ 0.5 ML coverage is thermodynamically most stable [Figure 3.2(g)]. Unlike O and S coverages, nitrogen introduces states at the Fermi level for most of the coverages studied here except of 0.33 and 0.5 ML . These are found to be semiconducting with 1.40 and 1.66 eV gap, respectively. For 0.5 ML coverage, the VBM and CBM align properly with $\Delta_{\mathrm{VBM}} = -0.07$ eV and $\Delta_{\mathrm{CBM}} = 0.36$ eV. In contrast, for 0.33 ML, the band edges align only at pH 9 solution with $\Delta_{\mathrm{VBM}} = -0.07$ eV and $\Delta_{\mathrm{CBM}} = 0.10$ eV.

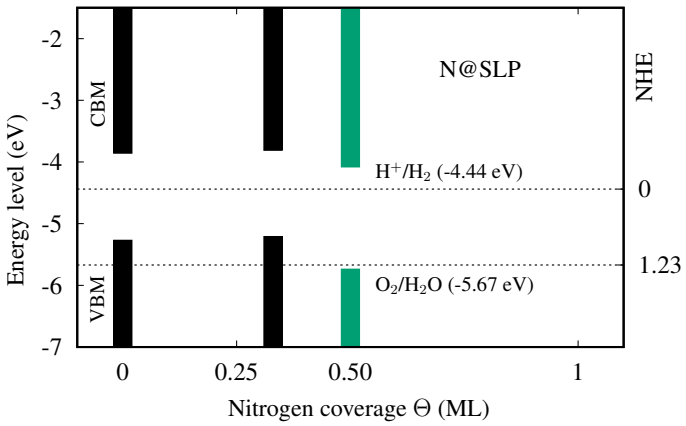

Figure 3.8: Band-edge positions of single layer phosphorene with varied nitrogen coverage at ambient condition, calculated within the hybrid HSE06 exchange-correlation functional.The energies are rescaled to the vacuum level and NHE.

We investigated the photocatalytic activity of nitrogen doped phosphorene, where 0.5 ML coverage of nitrogen on single layer phosphorene is active for water splitting reactions as shown in Figure 3.8.

The discussion will remain incomplete without an investigation of the interaction of H_2O molecule with these phosphorene derivatives. In this regard, the determination of active H_2O adsorption site is of supreme importance. We have thus investigated various H_2O adsorption sites on SLP with 0.5 ML O/S/N coverage, which are discussed to be conducive to complete redox reaction (Figure 3.5). We find that H_2O is adsorbed at the phosphorus atom with -0.35 eV binding energy, and acts as the active site. In comparison, H_2O adsorption at impurity oxygen is unfavourable with -0.28 eV binding energy.

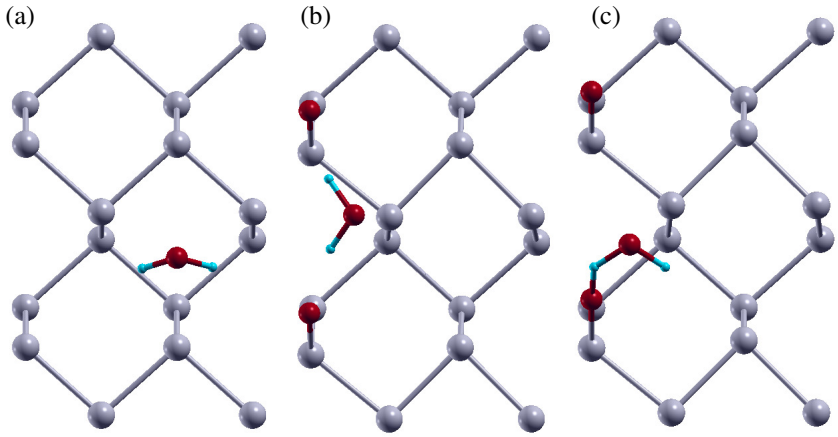

Figure 3.9: Water interaction with (a) pristine single layer phosphorene, (b, c) with the SLP with 0.5 ML oxygen coverage . Water adsorption at the phosphorous is shown in (b), while the same adsorbed at the impurity oxygen is shown in (c). Similar configurations were observed for 0.5 ML sulfur and nitrogen coverage, and are not shown here.

Figure 3.9 represents the favourable active site for pristine SLP, and 0.5ML oxygen coverage. From the binding energy criteria, configuration (b) is more favourable than (a) and (c) configurations.

In comparison H_2O binding on pristine SLP is weaker (-0.20 eV) in agreement with previous reports. [186, 187] Similar observation is achieved for S and N coverage. For adsorption at the active site, the O$-$H bonds in water is only slightly activated by 0.01 Å. However, the photocatalytic redox reaction is triggered by the photogenerated hole at the valence band. Thus, we investigate the H_2O structure in the presence of a hole to find that for 0.5 ML oxygen coverage, the O$-$H bond becomes much weaker and is elongated to 1.58 Å triggering the rupture.

3.3.4 Optical and excitonic properties

The frequency dependent complex dielectric tensor, $\varepsilon(\omega) = \varepsilon'(\omega) + i\varepsilon''(\omega)$, has been used to calculate the optical properties. The imaginary part $\varepsilon''(\omega)$ of the linear dielectric tensor is calculated in the long-wavelength $\mathbf{q} \to \mathbf{0}$ limit within the random phase approximation, [188]

$$\begin{aligned} \varepsilon''_{\alpha\beta}(\omega) &= \frac{4\pi^2 e^2}{\Omega} \lim_{q\to 0} \frac{1}{q^2} \sum_{c,v,\mathbf{k}} 2w_{\mathbf{k}} \delta(\epsilon_{c\mathbf{k}} - \epsilon_{v\mathbf{k}} - \omega) \\ &\times \langle u_{c\mathbf{k}+\mathbf{e}_\alpha q} | u_{v\mathbf{k}} \rangle \langle u_{c\mathbf{k}+\mathbf{e}_\beta q} | u_{v\mathbf{k}} \rangle^*, \end{aligned}$$

where the factor 2 inside the summation accounts for the spin degeneracy, Ω is the volume of the primitive cell, and $\omega_{\mathbf{k}}$ are k-point weights. The $\epsilon_{c\mathbf{k}}$ ($\epsilon_{v\mathbf{k}}$) are $\mathbf{k}$-dependent conduction (valence) band energies, $u_{c\mathbf{k},v\mathbf{k}}$ are cell periodic part of the pseudo-wave-function, and $\mathbf{e}_{\alpha,\beta}$ are unit vectors along the Cartesian directions. $\mathbf{q}$ is the Bloch vector of the incident wave. The corresponding real part $\varepsilon'(\omega)$ is calculated using Kramers-Kronig transformation. The absorption co-efficient $\Lambda_{\alpha\alpha}(\omega) = \frac{2\omega}{c}[|\varepsilon_{\alpha\alpha}(\omega)| - \varepsilon''_{\alpha\alpha}(\omega)]^{\frac{1}{2}}$ is calculated using the hybrid HSE06 exchange-correlation functional.

The electronic structure of phosphorene is anisotropic along different crystallographic directions. Thus, a strong anisotropic optical absorption is expected while

the incident light is linearly polarized along the armchair and zigzag directions of phosphorene (Figure 3.10). Pristine SLP and BLP show strong dichroism. For the incident light polarized along the armchair direction, the absorption peak is formed at the bandgap (1.41 eV for SLP), which show a sharp layer dependence (1.10 eV for BLP). In contrast, for the light polarized along the zigzag direction, the optical absorption peak is found at $\sim$ 3.22 eV for SLP, which does not show strong layer dependence (3.14 eV for BLP). The overall trend is in good agreement with previous reports. [150] The anisotropic nature of optical absorption remains intact upon oxygen coverage, and both SLP and BLP show similar features upon oxygen coverage. The absorption edge shifts to higher energy with increasing coverage for the light polarization along the armchair direction [Figure 3.10(a)]. In contrast, the same shifts to lower energy for light polarization along the zigzag direction [Figure 3.10(b)]. Further, the high absorption coefficient is unaffected by the oxygen coverage reported in Figure 3.10 and remains $\sim 10^5$ cm^{-1} for visible light absorption.

For S coverage, the optical properties show similar qualitative trends that are discussed for oxygen coverage (Figure 3.10). The absorption remains anisotropic in armchair and zigzag directions. For S coverage with $\Theta \leqslant 0.50$, the absorption edge is blue shifted for the incident light polarization along the armchair direction, as the band gap increases compared to pristine SLP (1.66 and 1.86 eV for 0.33 and 0.5 ML coverages, respectively). In contrast, the absorption is red shifted for light polarization along the zigzag direction with the absorption edge at 3.05 and 2.90 eV for 0.33 and 0.5 ML coverages, respectively. For both cases that are conducive to water oxidation (Figure 3.5), the absorption coefficient is found to be very high 10^5 cm^{-1} within visible light excitation.

In the figure(Figure 3.11), the absorption peaks along the armchair direction are 1.41, 1.66,and 1.86 eV for pristine SLP , 0.33ML, and 0.5ML of S-coverage, respec-

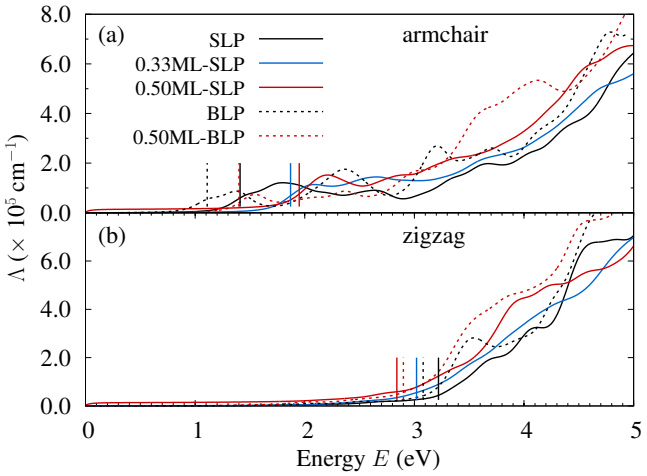

Figure 3.10: Optical absorption coefficients Λ for linearly polarized incident light along the (a) armchair, and (b) zigzag direction calculated with HSE06 hybrid exchange-correlation functional. Pristine SLP and BLP are compared with different oxygen coverages. The vertical lines correspond to the absorption edge calculated from the Tauc plots. Anisotropic nature of optical absorption is retained with oxygen coverage along with very high absorption coefficient $\Lambda \sim 10^5$ cm^{-1} in the visible optical range. While the absorption edge is shifted to higher energy for the light polarization along the armchair direction, it is reversed for the incident light polarization along the zigzag directions.

tively. While, the absorption peaks along the zigzag directions are 3.22, 3.05, and 2.90 eV for pristine SLP, 0.33 ML, and 0.50 ML of S-coverage, respectively.

Next, we investigate the excitonic properties in phosphorene derivatives, which are conducive to water splitting. The exciton binding, the bound state energy of an electron-hole pair, is an important metric for photocatalytic efficiency. However, a rigorous treatment within many-body theory with Bethe-Salpeter equation is practically impossible due to exceptional computational cost. In contrast, here we use a simplified hydrogenic model for anisotropic two-dimensional materials, which has been proved to provide results with very reasonable accuracy.[189–191] The parameters in this model, effective hole and electron mass along different crystallographic directions, and dielectric constant at zero frequency are calculated using HSE06 exchange-correlation functional. The obtained results for pristine SLP and

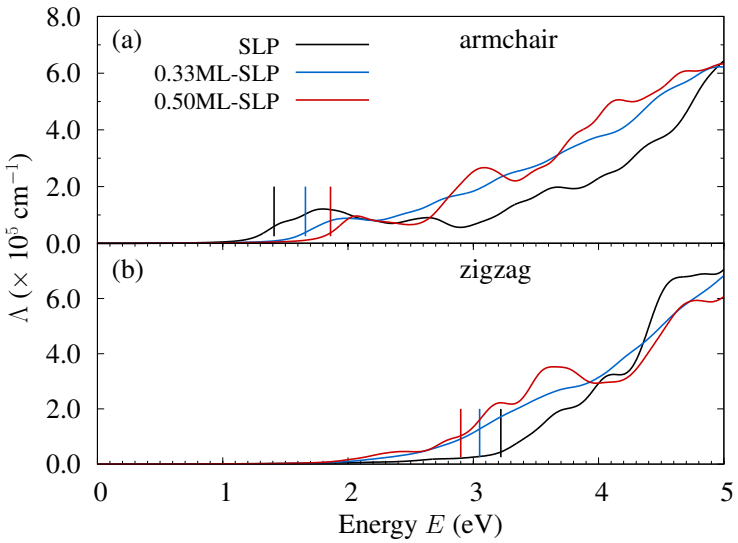

Figure 3.11: Optical absorption coefficient for SLP and compared with varied sulfur coverage. For linearly polarized light along (a) armchair and (b) zigzag directions calculated with hybrid HSE06 exchange-correlation functional. The vertical lines correspond to the absorption edge calculated from the Tauc plot.

BLP are in excellent agreement with previous GW-BSE results [174, 175, 192] and experimental measurement. [151] The calculated exciton binding E_b^{ex} is 0.76 eV, which confirm strongly bound exciton in SLP. Further, the exciton extension, $\mathcal{R}_{\text{arm}}^{\text{ex}}$ and $\mathcal{R}_{\text{zig}}^{\text{ex}}$, is found to be anisotropic with 12.20 and 4.88 Å, along the armchair and zigzag directions, respectively. Impurity coverage affects both exciton binding and extension. The exciton binding increases in phosphorene with impurity coverage, and further increases with increasing coverage. For example, E_b^{ex} = 0.87 and 0.92 eV for 0.33 and 0.5 ML O-coverage, respectively; whereas the same for S-coverage are found to be 0.90 and 1.13 eV, respectively. In contrast to pristine SLP, the excitons become more localized in these systems, $\mathcal{R}_{\text{arm}}^{\text{ex}}$ = 9.73 Å and $\mathcal{R}_{\text{zig}}^{\text{ex}}$ = 3.99 Å for 0.5 ML O-coverage, while the same for 0.5 ML S-coverage are calculated to be 6.94 and 5.34 Å, respectively. On the other hand, with increasing layer thickness in BLP, E_b^{ex} decreases to 0.48 eV, which is 0.75 eV for the 0.5 ML O-BLP system. A large exciton binding may lead to higher recombination and detrimental to photocatalytic

application. On the other hand, in these complexes, the very large electron/hole mobility with concurrent effective mass may lead to quick charge separation, and could be consumed in the respective catalytic reaction.

3.4 Conclusions

In the context of metal-free photocatalyst, a comprehensive investigation of electronic and optical properties of phosphorene derivatives is performed within first-principles calculations. The N, O and S adatoms bind strongly on the two- dimensional phosphorene, and preferentially bind at the dangling site. Further, the binding energy show strong coverage dependence, and 0.25–0.5 ML coverages are found to be most stable. The differential contribution of induced strain due to impurity loading has been discussed. Impurity binding does not introduce midgap impurity states, and the composite system remains semiconducting. At certain coverages (0.33 – 0.5 ML), which are also thermodynamically stable, the band edges align with the redox potentials for water splitting. Moreover, the absorption coefficient is found to be very high 10^5 cm^{-1} within the visible absorption range. Further, the layer dependence of band alignment and optical properties are investigated in bilayer phosphorene, and the same is found to be capable of oxidation and reduction reactions at 0.5 ML oxygen coverage. Further, we investigate the excitonic properties of the composites conducive to water splitting and compared with the pristine phosphorene. While two-dimensional phosphorene has been already proposed for potential applications in electronic and optoelectronic applications, the current investigation open up the possibility of using phosphorene derivatives as metal-free photocatalyst. [161] We hope the current study will simulate further theoretical and experimental investigations to take a complete advantage of its outstanding potential.

CHAPTER 4

VAN DER WAALS HETEROSTRUCTURE FOR PHOTOCATALYSIS: GRAPHITIC CARBON NITRIDE AND JANUS TRANSITION-METAL DICHALCOGENIDES

Converting solar energy into chemical energy by splitting water is a promising means to generate a sustainable and renewable solution without detrimental environmental impact. The two-dimensional semiconductors serve as potential catalysts in this regard, and here we combine Janus transition-metal dichalcogenides (MoXY, X/Y = S, Se, Te) and graphitic carbon nitride in a van der Waals heterostructure. Within the first-principles calculations, we investigate the electronic, optical and excitonic properties that determine the photocatalytic activity. Due to the internal electric field, the photogenerated electrons and holes are separated in the MoXY layers, and also generates high overpotentials for the redox reactions. The high optical absorptions span throughout the entire visible and near ultraviolet regime in these heterostructure nanocomposites. Further, the lower exciton binding, calculated within the two-dimensional hydrogenic model, indicates efficient charge separation. Enormous tunability of photocatalytic properties in such heterostructures should attract considerable theoretical and experimental attention in future. These results are published in the Physical Review Materials 3, 095402 (2019).

4.1 Introduction

The fascinating mechanical, electronic and optical properties of 2D materials and their concurrent tunability have opened up its applications in the modern electronic, catalytic, and in energy conversion and storage devices. [193–197] Combining properties in 2D heterostructures provides further tunability in this context. Among other energy applications, the photocatalytic water splitting on the 2D materials has been attracted particular attention to improve quantum efficiency. Apart from the easily tuneable intrinsic electronic structure, the 2D materials pose several advantages over other forms of nanomaterials. It maximizes the surface area for optical absorption and photocatalytic reaction. Further, it minimizes the distance travelled by the photogenerated electron and holes reducing recombination. In contrast, high exciton binding in the two-dimension due to reduced electron screening is a significant concern. [198–201] Despite significant achievements in optimizing photocatalytic activity, the low quantum efficiency hinders possible practical applications and warrants further material optimization.

Several 2D materials such as metal oxides and hydroxides, [202–206] metal chalcogenides, [207–210] and metal-free semiconductors [153, 211–215] have been investigated as photocatalysts. The metal chalcogenides and metal-free graphitic carbon nitride (g-C_3N_4) have attracted particular attention. The free-standing SnS_2 and wide-gap ZnSe single-layers exhibit much enhanced photocurrent, water splitting efficiency and photostability. [207, 208] The transition-metal dichalcogenides (TMDCs) offer encouraging optical properties in the visible region along with exceptionally high carrier mobility, which makes them excellent candidate materials for photocatalysis. [209, 210] On the other hand, heptazine based g-C_3N_4 is the most promising metal-free candidate, which show photocatalytic activity under visible-light irradiation, however, it suffers from extremely low quantum effi-

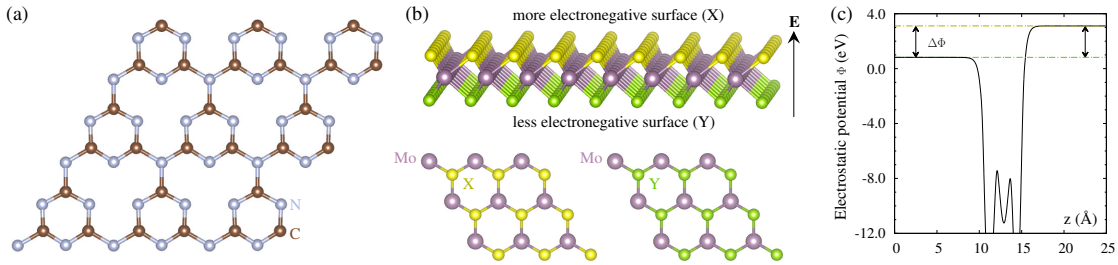

Figure 4.1: (a) The hexagonal 2D lattice of triazine-based graphitic carbon nitride (TGCN). No corrugation is observed in the free-standing single-layer TGCN. (b) The side and top views for the single-layer Janus MoXY (X/Y = S, Se and Te), where the out-of-plane crystal symmetry is broken, and an internal electric field **E** is developed due to the difference in Pauling electronegativity. (c) Schematic description of a high electrostatic potential difference $\Delta\Phi$ that is thus produced between the X and Y surfaces.

ciency. [211] In general, the catalytic activity in these materials is further tuned by doping, [213, 214, 216, 217] thickness, [207, 214, 218] defect engineering [219, 220] and making composites including 2D van der Waals heterostructures. [221–225] For example, the quantum efficiency has been drastically improved for the g-C_3N_4 quantum dots and while modified with iodine, oxygen, phosphorous and boron. [212–214, 216, 217]

The 2D van der Waals stacking is an attractive strategy to combine materials with distinctive properties to optimize the photocatalytic properties. Apart from the improved light absorption, the effective inter-layer charge separation can trigger reduction and oxidation of water on the different component layers. The concept was developed by combining MoS_2 and g-C_3N_4 in a heterostructure, which showed improved catalytic activity. [221] Since then several MoS_2 and g-C_3N_4 based heterostructures have been proposed. [222–225]

The breaking of out-of-plane structural symmetry in Janus TMDC provides another effective way to manipulate the electronic and optical properties. Single-layer MoSSe has been synthesized recently through a chemical vapour deposition based selenization or sulphurization methods. [226, 227] The presence of the

optically active vertical dipole presents an interesting light-matter interaction in this symmetry-broken TMDC. On the other hand, depending on the size of the nitrogen-linked aromatic moieties there are two structural models for g-C_3N_4 – triazine (C_3N_4) and heptazine C_6N_7 based graphitic sheets. Thus, owing to their structural differences, the intrinsic electronic and optical properties vary substantially. [228] While enormous experimental attempts have been put forward for heptazine based g-C_3N_4, [153, 211–215] it is only recently that the triazine-based counterpart was successfully synthesized. [229]

Here, we combine Mo-based Janus TMDCs and triazine-based g-C_3N_4 in a heterostructure architecture to investigate the properties that primarily determine the catalytic activity. Within the first-principles calculations the structural, electronic, and optical properties are studied comprehensively. Further, a two-dimensional hydrogenic exciton model is used to investigate exciton binding, where the parameters are derived from the first-principles calculations. Charge separation in the MoXY layers due to the internal electric field and lower exciton binding in these heterostructure nanocomposites indicate efficient charge separation favourable for photocatalysis. Effective utilization of the solar spectrum and high overpotential drive the redox reactions efficiently.

4.2 Methodology

The first-principles calculations were carried out using the density functional theory as implemented in the Vienna *Ab Initio* Simulation Package. [162, 163] The wave function of the systems was described within the projector augmented wave formalism and expanded in plane-wave basis with 500 eV cut-off for the kinetic energy. [164] The exchange-correlation energy was treated with the Perdew-Burke-Ernzerhof functional form of generalized gradient approximation during the struc-

tural optimization. [165] The weak van der Waals interaction was treated with non-local correlation functional vdW-DF-optB86. [230, 231] All the structures were completely optimized until all the force components are less than 0.01 eV/Å threshold. Subsequent electronic and optical properties are calculated using the hybrid Heyd-Scuseria-Ernzerhof (HSE06) exchange-correlational functional where a fraction of the exact Hartree-Fock exchange was considered. [167] A Γ-centered $9\times9\times1$, $17\times17\times1$, and $4\times4\times1$ k-mesh was used to sample the corresponding Brillouin zone for single-layers of g-C_3N_4, Janus MoXY (X/Y = S, Se, Te) and the van der Waals g-C_3N_4/MoXY heterostructures. We used a 30 Å vacuum in the direction perpendicular to the surface to minimize the spurious periodic interaction between the images. Dipole correction was incorporated due to the presence of an intrinsic electric field in the Janus MoXY TMDCs.

4.3 Results and Discussion

First, we discuss the single layers of triazine-based graphitic carbon nitride (TGCN) and Janus MoXY TMDCs. Next, we discuss the van der Waals MoXY/TGCN heterostructures, and investigate the electronic and optical properties in the context of their photocatalytic abilities. Finally, we discuss exciton renormalization in the composite structures within a two-dimensional hydrogenic model.

4.3.1 Single-layers of TGCN and Janus MoXY

While the heptazine based g-C_3N_4 has been studied extensively, [153, 211–214] very little attention has been put forward for TGCN since it was successfully synthesized. [229] The calculated hexagonal in-plane lattice parameter of 4.78 Å for the single-layer TGCN [Figure 4.1(a)] is consistent with the experimental bulk value and previous theoretical calculations. [229, 232] There are two distinct ni-

trogen sites in the lattice [Figure 4.1(a)]. The nitrogens that are bonded with two (three) neighbouring carbon atoms and form shorter 1.33 Å (longer 1.46 Å) C−N bonds. The HSE06 calculated bandstructure indicates the TGCN to be a direct gap semiconductor and the corresponding gap increases with the fractional Hartree-exchange a_{H}. The calculated gap of 2.7 eV for a_{H}=0.15 is consistent with the previous calculations, [229, 232] which increases to 3.3 eV for the conventional HSE06 functional with a_{H}=0.25 (Table 4.1). In comparison, the experimental gap for the macroscopic TGCN flake measured via optical absorption was in the 1.6-2.0 eV range. [229] However, due to stronger quantum confinement in the single-layer, the bandgap is expected to be larger. The valence band is composed of the atomic orbitals from the undercoordinated nitrogens in the lattice, while the conduction band originates from the carbon and undercoordinated nitrogen atoms. In contrast, the electronic states corresponding to the three-coordinated nitrogens appear much deeper in energy.

Table 4.1: Indirect and direct bandgaps E_g^i and E_g^d calculated using the HSE06 hybrid exchange-correlation functional for the single-layer MoSSe, MoSTe, TGCN, and their various heterostructures. The potential difference $\Delta\Phi$ across the two surfaces, and the calculated overpotentials $\chi_{\mathrm{H_2}}$ and $\chi_{\mathrm{O_2}}$ for the hydrogen and oxygen evolution reactions. All values are in eV.

System	E_g^i	E_g^d	$\Delta\Phi$	$\chi_{\mathrm{H_2}}$	$\chi_{\mathrm{O_2}}$
MoSSe	–	2.06	0.78	0.56	1.08
MoSTe	1.63	1.88	1.64	1.06	0.95
TGCN	–	3.32	–	1.81	0.29
MoSSe/TGCN					
S-facing	2.15	2.33	0.62	0.10	0.21
Se-facing	2.15	2.33	0.98	0.89	1.02
MoSTe/TGCN					
S-facing	1.73	1.80	1.54	0.63	1.07
Te-facing	1.73	1.80	1.95	1.27	1.17

The Janus MoSSe monolayer in Figure 4.1(b) was recently synthesized via sel-

enization and sulphurization of MoS_2 and $MoSe_2$, respectively. [226, 227] The calculated lattice parameter of MoSSe, MoSTe and MoSeTe are found to be 3.23, 3.34, and 3.41 Å, which are consistent with the available experimental and previous theoretical results. [226, 227, 233–235] The lattice parameters of MoXY is found to be the arithmetic mean of MoX_2 and MoY_2. Further, the Mo−X and Mo−Y bonds in Janus MoXY are almost equal to the corresponding bonds in the pristine MoX_2 and MoY_2.

The Janus TMDCs retain the semiconducting properties with a bandgap equivalent to the average of their natural counterparts. The HSE06 gaps are calculated to be 2.06, 1.63 and 1.76 eV for MoSSe, MoSTe, and MoSeTe, respectively, and are consistent with the previous calculation. [233] While MoSSe and MoSeTe are found to be direct-gap semiconductors with the gap at the K-point, the bandgap of MoSTe is found to be indirect in nature. While the conduction band minimum (CBM) in MoSTe is retained at the K-point, the valence band maximum (VBM) moves to the Γ-point. The out-of-plane structural symmetry in broken in the Janus MoXY and an internal electric field is developed due to the difference in electronegativity of the X and Y elements [Figure 4.1(b)]. Thus, a finite dipole moment perpendicular to the 2D surface is generated. [226, 233] As a result, a large electrostatic potential difference $\Delta\Phi$ is developed between the X and Y surfaces [Figure 4.1(c)] and should be carefully incorporated while the VBM and CBM are normalized with the electrostatic potential far from the 2D surface. The calculated $\Delta\Phi$ is 0.78, 1.64 and 0.89 eV for MoSSe, MoSTe, and MoSeTe, respectively.

4.3.2 TGCN and Janus MoXY heterostructures

While the single-layer TGCN structure is atomically flat [Figure 4.1(a)], a large corrugation d_{corr} is observed in the MoXY/TGCN heterostructures (Figure 4.2). We have considered both possible configurations, while the X or Y sublayer of MoXY

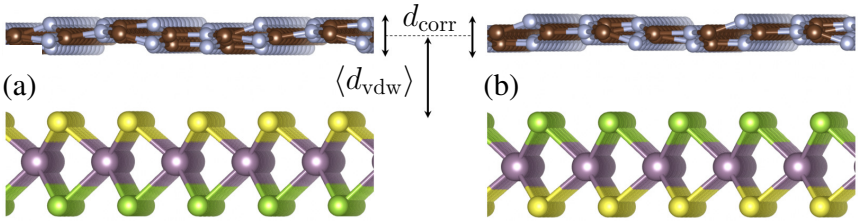

(c) Structural details and binding energy.

Heterostructure	Interaction	d_{corr} (Å)	$\langle d_{\text{vdw}} \rangle$ (Å)	E_b (meV/Å^2)
MoSSe/TGCN	S-side	0.92	3.35	−31
	Se-side	0.93	3.45	−30
MoSTe/TGCN	S-side	0.73	3.31	−12
	Te-side	0.72	3.61	−11
MoSeTe/TGCN	Se-side	0.63	3.37	+3
	Te-side	0.64	3.60	+3

Figure 4.2: In the MoXY/TGCN heterostructures, the X or Y sublayer of Janus MoXY interacts with the TGCN. The MoSSe/TGCN heterostructure is shown for the (a) S-side and (b) Se-side interactions. (c) The structural parameters, such as the corrugation in the TGCN layer d_{corr} and the average van der Waals separation $\langle d_{\text{vdw}} \rangle$ between the layers, for different heterostructures and the corresponding binding energies. The $\langle d_{\text{vdw}} \rangle$ increases with increasing chalcogen mass. The MoSeTe/TGCN heterostructures are not thermodynamically stable.

interacts with the TGCN [Figure 4.2(a) and (b)]. The structure and the concurrent electronic properties are modified accordingly [Figure 4.2(c)]. The corrugation is higher for MoSSe/TGCN than in the MoSTe/TGCN and MoSeTe/TGCN heterostructures. The average van der Waals distance between the layers $\langle d_{\text{vdw}} \rangle$ increases with increasing mass of the chalcogen [Figure 4.2(c)]. The heterostructures are thermodynamically stable except the MoSeTe/TGCN. The binding energy is calculated as $E_b = -[E(\text{MoXY/TGCN}) - E(\text{MoXY}) - E(\text{TGCN})]$ as shown in Figure 4.2(c). We did not further investigate the MoSeTe/TGCN structures as they are not thermodynamically stable. The redox potentials for the oxygen evolution reaction (OER, H_2O/O_2) and hydrogen evolution reaction (HER, H^+/H_2) are determined by the relative electrostatic potential of the two respective surfaces

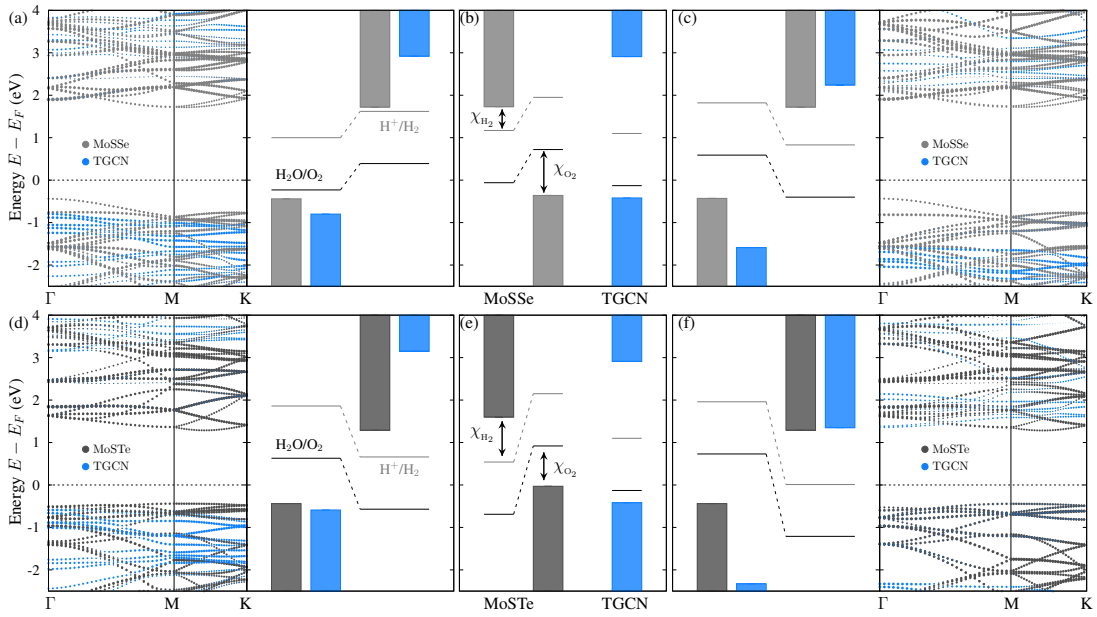

Figure 4.3: Band structure and band edge alignment for MoXY/TGCN heterostructures showing for (a) S-side interaction and (c) Se-side interaction in MoSSe/TGCN, (d) S-side interaction and (f) Te-side interaction in MoSTe/TGCN. Band alignments for the single-layer MoSSe, TGCN, and MoSTe are shown in (b) and (e). The redox potentials of H_2O/O_2 and H^+/H_2 are represented with black and grey lines, respectively. The overpotential for oxygen and hydrogen evolution reactions χ_{O_2} and χ_{H_2} are indicated in (b) and (e).

that are normalized by the vacuum potential. The overpotentials indicate the redox abilities of photogenerated carriers and are defined as the potential difference between the VBM/CBM and the corresponding redox potentials. Therefore, the χ_{O_2} (χ_{H_2}) is the energy difference between the VBM (CBM) and OER (HER) redox potential (Table 4.1 and Figure 4.3).

Before we discuss the electronic structure of these heterostructure nanocomposites in the context of photocatalytic activity, we start with the photocatalytic activities of the single layers of TGCN and MoXY. Similar to the heptazine based counterpart, we find that the valence band maximum (VBM) and conduction band minimum (CBM) for the single-layer TGCN lie at energies such that the photogenerated electrons and holes catalyse water-splitting [Figure 4.3(b)]. However, an

imbalance in the calculated overpotential is observed, $\chi_{O_2} = 0.29$ and $\chi_{H_2} = 1.81$ eV (Table 4.1). The photocatalytic activity of the Janus MoXY have been discussed in literature, [233, 234] and have proposed advantages over the pristine MoX_2. Due to the internal electric field shown in Figure 4.1 (a) the fundamental restriction to the band gap (> 1.23 eV) is lifted, and the redox potentials between the two surfaces shift by the electrostatic potential difference of $\Delta\Phi$ (Figure 4.3). (b) The photogenerated hot carriers are separated on the different X/Y sublayers indicating very efficient charge separation. For example, the photoexcited electrons and holes are accumulated on the Se and S side, respectively, for single-layer MoSSe. Therefore, the reduction and oxidation reactions are triggered on the different sides of the MoXY monolayer. The present results for these individual Janus MoXY are consistent with the previous results. [233, 234] Further, high overpotentials indicate efficient redox activity (Table 3.1 and Figure 4.3).

Having discussed the effectiveness of the single-layers of MoSSe, MoSTe and TGCN toward the redox reactions, we investigate their van der Waals heterostructures shown in Figure 4.2. The band structure in MoSSe/TGCN heterostructures is altered in both the configurations in which S/Se sublayer interacts with the TGCN [Figure 4.3(a) and (c)]. In both cases, while the overall band structure becomes indirect with a gap of 2.15 eV, the direct gap at the Γ-point is slightly higher at 2.33 eV. The layer-projected band structures in Figure 4.3(a) and (c) indicate type I band alignment, and both the VBM and CBM lies in the MoSSe layer. While the MoSSe band structure in both the composite structures are similar to that of the isolated MoSSe monolayer, the same corresponding to the TGCN is substantially perturbed. Further, due to a different $\Delta\Phi$ in these two configurations, the redox potentials are shifted [Figure 4.3(a) and (c)], which results in different values for the χ_{O_2} and χ_{H_2} overpotentials (Table 4.1). The overpotentials are much larger in the case of Se-side interaction than the S-side interaction, which indicates high re-

dox ability (Table 4.1 and Figure 4.3). A deeper investigation into the electronic density of states reveals that both VBM and CBM is composed of the Mo-d_{xy} and Mo-d_{z^2} orbitals in S/Se-facing MoSSe/TGCN configurations. The charge density analysis indicates that due to the internal electric field, the photoexcited electron and holes are separated on the Se and S sublayers, respectively. Thus, while for the MoSSe/TGCN heterostructure with S-side interaction [Figure 4.3(a)], the excited electrons on the Se-side are exposed to the H^+/H_2 reaction, the H_2O/O_2 redox reaction is blocked as the photogenerated holes at the S-side cannot be accessed. Conversely, for the heterostructure with Se-side interaction [Figure 4.3(c)], the H_2O/O_2 reaction takes place at the exposed S-sublayer, while the H^+/H_2 reaction is blocked.

In the cases of S-faced and Te-faced MoSTe/TGCN heterostructures, both the MoSTe and TGCN band structures are perturbed, and the band gap remains indirect (1.73 eV) similar to that of the single-layer MoSSe (Table 4.1 and Figure 4.3). However, the direct gap at the M-point is found to be slightly larger at 1.80 eV (Table 4.1). We find the type I band alignment for MoSTe/TGCN configurations, while both VBM and CBM are composed with the Mo-d_{z^2}, Mo-d_{xy} and Mo-$d_{x^2-y^2}$ orbitals. In the MoSTe/TGCN heterostructures, the photoexcited electrons (holes) are separated on the Te (S) sublayers of MoSTe, respectively. The overpotentials χ_{O_2} and χ_{H_2} for all the heterostructures, except for the S-faced MoSSe/TGCN is calculated to be higher than 0.6 eV, indicating their high redox abilities. The χ_{O_2} and χ_{H_2} are much higher than the recently predicted M_2X_3 (M = Al, Ga, In; X = S, Se, Te) family of photocatalysts. [236]

4.3.3 Optical properties

The frequency-dependent complex dielectric tensor $\varepsilon(\omega) = \varepsilon'(\omega) + i\varepsilon''(\omega)$ is used to calculate the optical properties. As discussed in the Chapter 3, the imaginary

part $\varepsilon''(\omega)$ is evaluated in the long-wavelength $\mathbf{q} \to \mathbf{0}$ limit, [188]

$$\begin{aligned} \varepsilon''_{\alpha\beta}(\omega) &= \frac{4\pi^2 e^2}{\Omega} \lim_{q\to 0} \frac{1}{q^2} \sum_{c,v,\mathbf{k}} 2w_{\mathbf{k}} \delta(\epsilon_{c\mathbf{k}} - \epsilon_{v\mathbf{k}} - \omega) \\ &\times \langle u_{c\mathbf{k}+\mathbf{e}_\alpha q} | u_{v\mathbf{k}} \rangle \langle u_{c\mathbf{k}+\mathbf{e}_\beta q} | u_{v\mathbf{k}} \rangle^*. \end{aligned} \tag{4.1}$$

$\mathbf{q}$ is the Bloch vector of the incident wave. The factor 2 inside the summation accounts for the spin degeneracy, Ω is the volume of the primitive cell, and $\omega_{\mathbf{k}}$ are k-point weights. The $\epsilon_{c\mathbf{k}}$ ($\epsilon_{v\mathbf{k}}$) are $\mathbf{k}$-dependent conduction (valence) band energies, $u_{c\mathbf{k},v\mathbf{k}}$ are cell periodic part of the pseudo-wave-function, and $\mathbf{e}_{\alpha,\beta}$ are unit vectors along the Cartesian directions. The real part $\varepsilon'(\omega)$ of the frequency dependent complex dielectric tensor $\varepsilon(\omega)$ is calculated using the Kramers-Kronig transformation, and the absorption co-efficient is calculated as $\Lambda_{\alpha\alpha}(\omega) = \frac{2\omega}{c}[|\varepsilon_{\alpha\alpha}(\omega)| - \varepsilon'_{\alpha\alpha}(\omega)]^{\frac{1}{2}}$.

The optical absorption coeffiecients are calculated for Janus MoSSe and MoSTe, using GW+BSE formalism(Figure 4.4). GW+BSE calculations are not possible for the heterostructures due to enormous computational cost, and we proceed with the hybrid exchange-correlation functional instead.

We calculate the absorption coefficient $\Lambda(\omega)$ in Figure 4.5 using the HSE06 exchange-correlation functional, which means that the electron-hole interaction is not considered. However, we will estimate the binding between the photogenerated $e-h$ pair in the next section. Both MoSSe and MoSTe show strong photoabsorption in the entire visible range (Figure 4.5). While single-layer of MoSSe is a direct gap semiconductor, the direct and indirect gaps in the single-layer MoSTe are similar, reflecting in high photoabsorption. Although TGCN is a direct gap semiconductor with 3.3 eV HSE06 gap, the absorption is negligible below 4.5 eV, which is in agreement with the experimental and previous theoretical calculations. [229, 232] The negligible optical transition between the VBM and CBM at

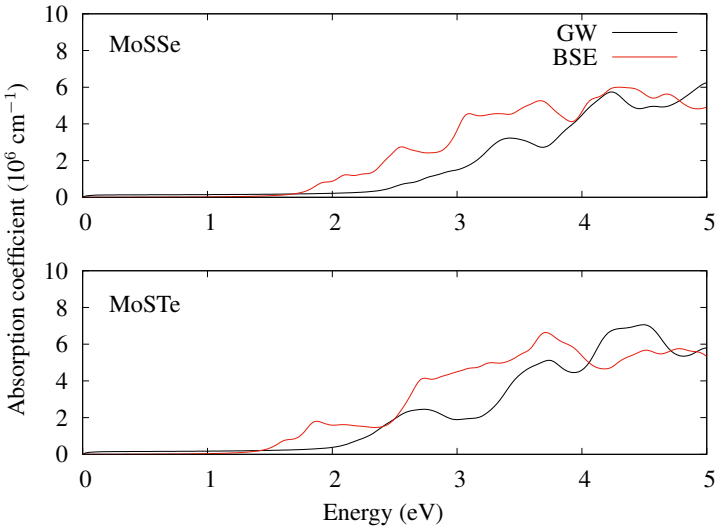

Figure 4.4: Absorption coefficient for the Janus MoXY calculated without and with the electron-hole interaction using GW+BSE formalism. The top (bottom) panel refers to MoSSe (MoSTe). Excitonic contributions are significant for both monolayers.

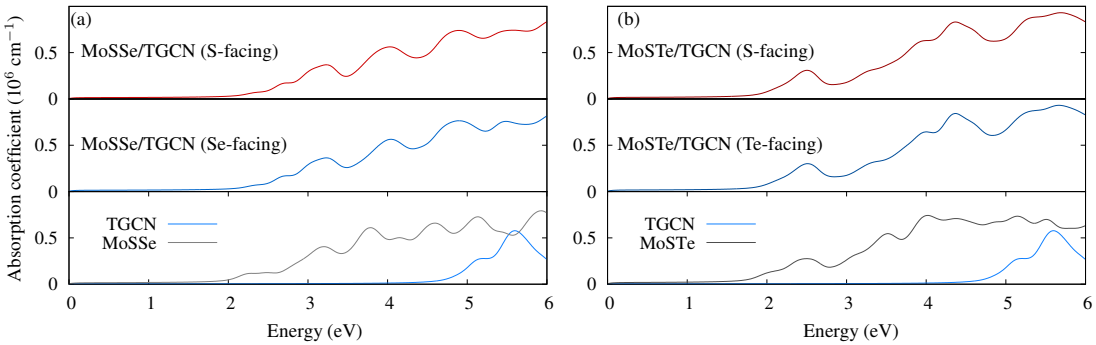

Figure 4.5: The optical absorption coefficient $\Lambda(\omega)$ calculated for the (a) MoSSe/TGCN and (b) MoSTe/TGCN heterostructure nanocomposites. All possible interaction architectures are considered. All the heterostructures show strong photoabsorption in the entire visible range and extend to the ultraviolet regime.

the Γ-point pushes light absorption to the ultraviolet range. The nanocomposites form type I heterojunction as discussed earlier, and the corresponding visible light absorption is similar to that of the MoSSe and MoSTe monolayers, with very high $\Lambda > 10^5$ cm^{-1} (Figure 4.5). Further, compared to the TGCN monolayer, the heterostructures exhibit more efficient ultraviolet absorption.

Table 4.2: Energy conversion efficiency of light absorption (η^{abs}), carrier utilization η^{CU}, solar-to-hydrogen η^{STH} and corrected solar-to-hydrogen $\eta^{STH'}$ for MoSSe/TGCN heterostructure. All values are in %.

System	η^{abs}	η^{CU}	η^{STH}	$\eta^{STH'}$
MoSSe	33.94	45.81	15.55	13.11
MoSTe	54.78	50.57	27.70	17.76
MoSSe/TGCN				
S-face	30.27	23.31	7.05	6.21
Se-face	30.27	44.88	13.59	13.58
MoSTe/TGCN				
S-face	49.77	49.48	24.63	16.54
Te-face	49.77	49.48	24.63	15.20

4.3.4 Solar to hydrogen efficiency

Although the methodology to calculate the solar-to-hydrogen efficiency has been described in detail elsewhere in References [236, 237], here we reproduce it for convenience of the reader, along with the results for the present heterostructures. For an ideal photocatalyst, all incoming photons with energies greater than the band gap contribute to the catalytic reaction. Accordingly, the absorption efficiency η^{abs} is given by the expression, [236]

$$\eta^{abs} = \frac{\int_{E_g}^{\infty} P(\hbar\omega)d(\hbar\omega))}{\int_{0}^{\infty} P(\hbar\omega)d(\hbar\omega)}, \tag{4.2}$$

where $P(\hbar\omega)$ is the AM1.5G solar energy flux at the photon energy $\hbar\omega$. The fraction of photons that are absorbed depends on the band gap E_g and as a consequence, materials with small band gaps have large absorption efficiency. The carrier utilization efficiency η^{CU} takes into account the energy E required to overcome the OER/HER redox potential barriers. ΔG is the potential energy difference (1.23 eV)

between redox potentials of H_2O/O_2 and H^+/H_2.

$$\eta^{CU} = \frac{\Delta G \int_E^\infty \frac{P(\hbar\omega)}{\hbar\omega} d(\hbar\omega))}{\int_{E_g}^\infty P(\hbar\omega) d(\hbar\omega)} \tag{4.3}$$

For $\chi_{O_2} \geq 0.6$ eV and $\chi_{H_2} \geq 0.2$ eV, no energy loss occurs for the photocarriers contributing to water splitting. For lower overpotentials, a fraction of carriers upto energy E are consumed in overcoming the barriers. Here, E is estimated by the below expression.

$$\begin{aligned} E &= E_g, \text{ if } \chi_{H_2} \geqslant 0.2, \chi_{O_2} \geqslant 0.6 \\ &= E_g + 0.2 - \chi_{H_2} \text{ if } \chi_{H_2} < 0.2, \chi_{O_2} \geqslant 0.6 \\ &= E_g + 0.6 - \chi_{O_2} \text{ if } \chi_{H_2} \geqslant 0.2, \chi_{O_2} < 0.6 \\ &= E_g + 0.8 - \chi_{H_2} - \chi_{O_2} \text{ if } \chi_{H_2} < 0.2, \chi_{O_2} < 0.6 \end{aligned} \tag{4.4}$$

The solar-to-hydrogen efficiency η^{STH} is defined as,

$$\eta^{STH} = \eta^{abs} \times \eta^{CU} \tag{4.5}$$

Further, the contribution of internal electric field towards electron-hole separation is considered in the following expression. Here, $\Delta\Phi$ is the potential difference across the surfaces.

$$\eta^{STH'} = \frac{\eta^{STH} \int_0^\infty P(\hbar\omega) d(\hbar\omega)}{\int_0^\infty P(\hbar\omega) d(\hbar\omega) + \Delta\Phi \int_{E_g}^\infty \frac{P(\hbar\omega)}{\hbar\omega} d(\hbar\omega)} \tag{4.6}$$

The absorption effieciency η^{abs}, carrier utilizationn η^{CU}, solar-to-hydrogen η^{STH} and corrected solar-to-hydrogen $\eta^{STH'}$ are tabulated (Table 4.2) for MoSSe/TGCN,

MoSTe/TGCN heterostructures.

4.3.5 Exciton in heterostructures

The Coulomb interaction between the photoexcited electron and hole pairs is attractive, and the strength of this interaction in the quasiparticle called exciton is an important quantity, which directly affects the photocatalytic efficiency. Lower exciton binding indicates an easy charge separation, and concurrently be consumed in the redox reactions. Due to the substantial reduction in electron screening in two-dimension, the exciton binding in 2D semiconductors is exceedingly enhanced. A theoretical investigation in this regard and within the first-principles approach is difficult since the formalism in which the many-body perturbation theory is coupled with the Bethe-Salpeter equation is computationally very expensive. This difficulty necessitates modelling exciton within the Keldysh formalism, [238] where the parameters for exciton binding can be calculated using a much less expensive first-principles calculations. Within the Keldysh formalism, the hydrogenic effective exciton Hamiltonian is expressed as, $H_{\mathrm{x}} = -\frac{\hbar^2}{2\mu}\nabla_r^2 + V_{2\mathrm{D}}(r)$, where μ is the exciton reduced mass, and r is the electron-hole separation. The two-dimensional and non-locally screened electron-hole interaction is described using the Struve H_0 and Bessel Y_0 function as, $V_{2\mathrm{D}}(r) = -\frac{e^2}{4(\varepsilon_1+\varepsilon_2)\varepsilon_0 r_0}[H_0(\frac{r}{r_0}) + Y_0(\frac{r}{r_0})]$, where ε_1 and ε_2 are the dielectric constant of the upper and lower media; and ε_0 is the vacuum permittivity. [190, 201, 239] The screening length $r_0 = 2\pi\chi_{2\mathrm{D}}$ with $\chi_{2\mathrm{D}}$ the 2D polarizability, which is calculated using the static dielectric constant ε of the 2D system, $\varepsilon(L_{\mathrm{v}}) = 1 + 4\pi\chi_{2\mathrm{D}}/L_{\mathrm{v}}$, where L_{v} is the transverse vacuum size. [240] The ε is calculated from the real part of the complex dielectric tensor $\epsilon(\omega)$ at zero frequency. Thus, the present model following Keldysh formalism requires the effective masses of the photoexcited electron and hole along with the static dielectric constant. In the present calculations, these parameters are calculated using the

hybrid HSE functional. Previously, we have used a similar approach to describe exciton binding in anisotropic phosphorene derivatives, which also correctly described the exciton renormalization in the few-layer phosphorene and heterostructures. [201]

Table 4.3: The parameters for the two-dimensional hydrogenic exciton model, the effective carrier mass m_e^*, m_h^*, and the static dielectric constant ε that is calculated using 30 Å vacuum perpendicular the surface. Exciton binding E_x^b in the heterostructure nanocomposites show renormalization with an isotropic extension ξ of 1 nm.

System	m_e^*/m_e	m_h^*/m_e	ε	E_x^b (eV)	ξ (Å)
MoSSe/TGCN					
S-facing	0.63	0.68	3.81	0.51	9.20
Se-facing	0.50	0.68	3.81	0.50	9.52
MoSTe/TGCN					
S-facing	0.44	1.81	4.53	0.44	9.75
Te-facing	0.43	1.84	4.53	0.44	8.83

To establish the applicability of the hydrogenic model of exciton for the composite systems, we first calculated the exciton binding for the single-layer MoXY by considering the explicit electron-hole interaction within the many-body perturbation-theory-based GW method plus Bethe-Salpeter equation (BSE) formalism, [121, 123, 241, 242] and compare the results with the model calculations. Model calculations of 0.58 and 0.57 eV exciton binding for the Janus MoSSe and MoSTe are in excellent agreement with the present BSE calculations of 0.53 and 0.59 eV, respectively. Due to better electron screening in the MoXY/TGCN heterostructure nanocomposites, the calculated E_x^b shows strong renormalization indicating easier charge separation (Table 4.3), which is favourable for photocatalysis. It is important to note that, while X/Y-facing interaction with TGCN differently impacts the electronic band structure leading to differential over-potentials χ_{H_2} and χ_{O_2} (Table 4.1 and Figure 4.3), however, it does not alter the E_x^b. Further, owing to the type I band

alignment, the exciton is localized in the MoXY layer with an extension ξ about 1 nm.

4.4 Conclusions

Within the first-principles calculations, we have investigated the van der Waals Janus MoXY/g-C_3N_4 heterostructures in the context of photocatalysis. While the overall electronic band structure for the nanocomposites are type I, due to the internal electric field the photogenerated electrons and holes are separated in the two-sides of MoXY. The high overpotentials indicate efficient hydrogen and oxygen evolution reactions. High optical absorption above 10^5 cm^{-1} in the entire visible region including near ultraviolet regime indicates excellent utilization of the solar spectrum. Further, we have calculated the exciton binding within a simplistic two-dimensional hydrogenic model as the BSE approach is impossible for the nanocomposites studied here. Compared to the single-layer MoXY, in the heterostructures, we observe strong exciton renormalization due to increased electron screening indicating efficient charge separation. The present results open up an enormous tunability and design opportunity in van der Waals heterostructures.

CHAPTER 5

EXCITON IN PHOSPHORENE: STRAIN, IMPURITY, THICKNESS AND HETEROSTRUCTURE

Reduced electron screening in two-dimension plays a fundamental role in determining exciton properties, which dictates optoelectronic and photonic device performances. Considering the explicit electron-hole interaction within the *GW*-Bethe-Salpeter formalism, we first study the excitonic properties of pristine phosphorene and investigate the effects of strain and impurity coverage. The calculations reveal strongly bound exciton in these systems with anisotropic spatial delocalization. Further, we present a simplified hydrogenic model with anisotropic exciton mass and effective electron screening as parameters, and the corresponding results are in excellent agreement with the present *GW*-BSE calculations. The simplified model is then used to investigate exciton renormalization in few-layer and heterostructure phosphorene. The changes in carrier effective mass along with increasing electron screening renormalizes the exciton binding in these systems. We establish that the present model, where the parameters are calculated within computationally less expensive first-principles calculations, can predict exciton properties with excellent accuracy for larger two-dimensional systems, where the many-body *GW*-BSE calculations are impossible. These results are published in the Physical Review B, 99, 045432 (2019).

5.1 Introduction

Excitonic properties in reduced dimensions are markedly different due to the fundamental difference in electron screening, and has attracted much attention conceptually in recent times. [175, 191, 243–246] Weaker electron screening in one-dimensional systems, such as carbon and boron nitride nanotubes, results in high exciton binding. [243–245] Likewise, the two-dimensional (2D) materials interact strongly with light, and the concurrently generated electron-hole pairs interact strongly due to reduced screening. [199, 247–251] For example, while exciton binding is small, 84 meV, in bulk MoS_2, [252] due to reduced screening in monolayer MoS_2, it is measured to be in 220 – 570 meV range. [249–251] Moreover, unlike the Frenkel excitons, the excitons in 2D materials can be delocalized in space and extend over 1 nm. [199, 248, 253] Further, the widely varying exciton binding has been reported in the different class of materials and has important implications in device applications. For applications in solar cells, photodetectors, and catalytic devices, exciton with weak binding leading to easy dissociation is desirable. In contrast, the materials with strong exciton binding are ideal to study plausible exciton-polariton condensate and for applications such as polariton lasing. [254]

Phosphorene has attracted a lot of attention due to its many plausible technological applications, [145, 255–258] and has become an interesting proving ground for many-body physics.[259–261] The Dirac semimetal state has been experimentally realized in few-layer phosphorene under adatom absorption. [260] We have recently reported an intrinsic, robust and high-temperature Kondo state in defected phosphorene doped with a transition-metal impurity. [261] In the present context, phosphorene has unique optical properties that are mainly determined by the quasiparticle band structure and screening. Originating from a puckered honeycomb network, the electronic band structure is highly asymmetric in phospho-

rene and consequently, the optical properties are also found to be highly anisotropic. [175, 200, 255, 256] The quasiparticle and optical gaps of single-layer phosphorene (SLP) are experimentally measured to be 2.2 $\pm$ 0.1 eV and 1.3 $\pm$ 0.02 eV, respectively, through photo-luminescence excitation spectroscopy (PLE). [200] This results in a very high exciton binding energy of 0.9 $\pm$ 0.12 eV due to reduced screening in 2D quantum confinement.

Studying quasiparticle band structure and the corresponding optical properties is a non-trivial and computationally expensive task. The conventional density functional approach fails to reproduce the correct experimental results which involve excited states. [262] In contrast, the many-body perturbation theory based *GW* method produces the correct quasiparticle energies. [121] In this approach, the electron self-energies are expressed in terms of Green's function G and screened Coulomb interaction W. Further, the optical properties of semiconductors and insulators are strongly affected by interacting electron-hole pairs, which is described through the Bethe-Salpeter equation (BSE). [123, 241, 242] These theoretical descriptions lead to an excellent agreement with the experimental results. [262]

Here, we study the quasiparticle and optical properties of SLP and its derivatives within the *GW* and BSE formalisms, and also investigate the effects of strain. Results on the pristine SLP are in excellent agreement with those obtained from the transmission and photoluminescence spectroscopies. [200, 263] The optical absorption and the corresponding excitons are found to be highly anisotropic. Due to the 2D confinement of photogenerated electron-hole pairs, the exciton binding is exceptionally strong, which is in accordance with the experimental measurements. [200]

While a rigorous treatment of electron-hole interaction within the BSE formalism provides an excellent description of exciton binding, [199, 253, 262, 264, 265] it is computationally very expensive and thus restricted to the systems with small

size. In this context, we describe a hydrogenic effective exciton mass model in which the parameters, the effective carrier masses and the static dielectric constant, are calculated within the conventional density functional theory (DFT) calculations. [190, 239] The results of this simplified model are in excellent agreement with those calculated within the BSE formalism for the pristine and strained SLP along with the SLPs with 1 ML impurity coverage. Further, the anisotropic hydrogenic model is extended for larger systems with low impurity coverages that are earlier predicted to be good candidate materials for water redox reactions. [258]

The quantum confinement of exciton should be extraordinarily affected by the varied thickness of the 2D material, which alters electron screening. This picture is well captured within the present model through the renormalization of exciton binding in few-layer phosphorene. Furthermore, the practical applications of phosphorene are limited due to its fast degradation in ambient conditions resulting in a severe alteration in the corresponding electronic properties. [266–268] Thus to avoid degradation, phosphorene is encapsulated with a capping layer and substrate, and the devices restore the intrinsic carrier mobility of phosphorene. [145, 200, 266, 269–271] In this regard, we investigate the electronic and exciton properties in SLP encapsulated with atomically thin hexagonal boron-nitride (h-BN), which is often used to protect phosphorene from degradation. [269–271]

5.2 Methodology

The structural optimizations were carried out within the conventional DFT formalism [162, 163] and the electrons are treated within the projector augmented wave method. [164] The Kohn-Sham orbitals were expanded in plane-wave basis with 400 eV energy cutoff. The exchange-correlation energy was described with Perdew-Burke-Ernzerhof (PBE) functional. [165] The Brillouin-zone was sampled

using Γ-centred 17×13×1 Monkhorst-Pack k-grid. [166] Complete structural optimization was carried until the forces exerted on each atom are less than 0.01 eV/Å threshold. In phosphorene, three electrons participate in the covalent σ-bonding with three neighboring P atoms, whereas the remaining two electrons occupy a lone pair orbital. Thus, for phosphorene and its derivatives such as P_4X (X=O and S), we considered van der Waals interaction through the non-local correlation functional optB88-vdW during the structural optimization, [230, 272] while for the larger systems in few-layer and heterostructure phosphorene we used the D3 functional with zero damping. [169] The obtained lattice parameters for SLP are a = 4.58 and b = 3.32 Å along the armchair and zigzag directions, respectively, are consistent with the previous reports and experimental black phosphorus. [150, 263, 266, 273, 274]

The optimized structures with the PBE exchange-correlation functional are then used for the subsequent GW-BSE calculations. The quasiparticle (QP) picture is investigated within the partially self-consistent GW_0 approach by iterating the one-electron energies in the Green's function G. [121, 122] Two self-consistent updates for the Green's function (G_2W_0) are found to be sufficient to converge the QP band gap. The convergence of QP gap as a function of unoccupied bands was found to be much faster for phosphorene, [175] and we find that 158 such bands to be sufficient in this regard. Further, the electron-hole interactions are incorporated within the BSE formalism, which provides the optical gap and the corresponding exciton binding energy. [123, 242, 262]

The optical properties are calculated using frequency dependent complex dielectric tensor, $\varepsilon(\omega) = \varepsilon'(\omega) + i\varepsilon''(\omega)$. The imaginary part $\varepsilon''(\omega)$ of the linear

dielectric tensor is calculated in the long-wavelength $\mathbf{q} \to \mathbf{0}$ limit, [188]

$$\begin{aligned} \varepsilon''_{\alpha\beta}(\omega) &= \frac{4\pi^2 e^2}{\Omega} \lim_{q\to 0} \frac{1}{q^2} \sum_{c,v,\mathbf{k}} 2w_{\mathbf{k}} \delta(\epsilon_{c\mathbf{k}} - \epsilon_{v\mathbf{k}} - \omega) \\ &\times \langle u_{c\mathbf{k}+\mathbf{e}_\alpha q} | u_{v\mathbf{k}} \rangle \langle u_{c\mathbf{k}+\mathbf{e}_\beta q} | u_{v\mathbf{k}} \rangle^*, \end{aligned} \tag{5.1}$$

where Ω is the volume of the primitive cell, $\omega_{\mathbf{k}}$ are k-point weights, and the factor 2 inside the summation accounts for the spin degeneracy. The $\epsilon_{c\mathbf{k}}$ ($\epsilon_{v\mathbf{k}}$) are $\mathbf{k}$-dependent conduction (valence) band energies, $u_{c\mathbf{k},v\mathbf{k}}$ are cell periodic part of the pseudo-wave-function, and $\mathbf{e}_{\alpha,\beta}$ are unit vectors along the Cartesian directions. The real part $\varepsilon'(\omega)$ is calculated using Kramers-Kronig transformation, and the absorption co-efficient is calculated as $\Lambda_{\alpha\alpha}(\omega) = \frac{2\omega}{c}[|\varepsilon_{\alpha\alpha}(\omega)| - \varepsilon'_{\alpha\alpha}(\omega)]^{\frac{1}{2}}$.

Within the BSE formalism, an exciton state $|S\rangle$ can be written as, [123]

$$|S\rangle = \sum_{\mathbf{k}}^{\text{hole}} \sum_{v}^{\text{elec}} \sum_{c} A^S_{vc\mathbf{k}} |vc\mathbf{k}\rangle; \tag{5.2}$$

where $|vc\mathbf{k}\rangle = \hat{a}^\dagger_{v\mathbf{k}} \hat{b}^\dagger_{c\mathbf{k}+\mathbf{q}} |0\rangle$ with $|0\rangle$ being the ground state, and $\hat{a}^\dagger(\hat{b}^\dagger)$ is hole (electron) creation operator. $\mathbf{q}$ is the momentum of the absorbed photon, and $A^S_{vc\mathbf{k}}$ are electron-hole amplitudes. The corresponding excitation energies E_S are determined via BSE, [275]

$$\begin{aligned} \left(\epsilon^{\text{QP}}_{c\mathbf{k}+\mathbf{q}} - \epsilon^{\text{QP}}_{v\mathbf{k}}\right) A^S_{vc\mathbf{k}} &+ \sum_{v'c'\mathbf{k}'} A^S_{v'c'\mathbf{k}'} \langle vc\mathbf{k} | K^{eh} | v'c'\mathbf{k}' \rangle \\ &= E_S A^S_{vc\mathbf{k}}, \end{aligned} \tag{5.3}$$

where ϵ^{QP} are quasiparticle energies, and K^{eh} is the electron-hole interaction. The imaginary part of the dielectric function $\varepsilon''(\omega)$ is calculated by the optical transition matrix element of the excitations.

Such a rigorous treatment within the many-body theory coupled with BSE scheme provides an excellent description of QP and optical gaps; and exciton bind-

ing, which all compare well with the experimental results. [199, 253, 262, 264, 265] However, such treatment is restricted to the systems with small size due to its exceptional computational cost. Thus, one needs to develop simplified models to investigate excitons in realistic systems with appreciable accuracy. For three-dimensional materials, the simplistic Mott-Wannier model predicts the exciton binding energy as, $E_{\mathrm{x}}^{\mathrm{3D}} = (\mu/\varepsilon^2)R_\infty$, where R_∞ is the Rydberg constant. The excitonic effective mass μ and the static dielectric constant ε can easily be calculated within the standard electronic structure calculations. [276]

In contrast, the excitonic properties of two-dimensional materials are fundamentally different from their 3D counterpart, and cannot be described within the Mott-Wannier approach. In 2D materials, excitons are strongly confined and the dielectric screening is considerably reduced. [199, 247–251] There have been recent efforts to develop excitonic models for 2D materials, however, the significant effort has been devoted to the isotropic materials such as transition metal dichalcogenides. [189–191, 198, 239] Here, we present a generalized scheme appropriate for the anisotropic electronic materials such as phosphorene and its various derivatives. [190, 239]

For 2D semiconducting systems, the effective exciton Hamiltonian can be written as,

$$H_{\mathrm{x}} = -\hbar^2 \frac{\nabla_r^2}{2\mu} + V_{\mathrm{2D}}(r), \tag{5.4}$$

where $\mu^{-1} = m_e^{-1} + m_h^{-1}$ is the exciton reduced mass, and r is the electron-hole separation. Following Keldysh, the non-locally screened electron-hole interaction is described by, [238]

$$V_{\mathrm{2D}}(r) = -\frac{e^2}{4(\varepsilon_1+\varepsilon_2)\varepsilon_0 r_0}\left[H_0\left(\frac{r}{r_0}\right) - Y_0\left(\frac{r}{r_0}\right)\right], \tag{5.5}$$

where ε_1 and ε_2 are the dielectric constant of the upper and lower media (air) and

thus $\varepsilon_1 = \varepsilon_2$; and ε_0 is the vacuum permittivity. H_0 and Y_0 are Struve and Bessel functions. The screening length r_0 is related to the 2D polarizability χ_{2D} as $r_0 = 2\pi\chi_{2D}$, [240] where χ_{2D} is calculated using the static dielectric constant ε of the concerned 2D material, $\varepsilon(L_v) = 1 + 4\pi\chi_{2D}/L_v$, where L_v is the transverse vaccuum size. The ε is calculated from the real part of complex dielectric tensor $\varepsilon(\omega)$ at zero frequency. Note that the interaction V_{2D} at large separation $r >> r_0$ follow the $1/r$ Coulomb interaction, whereas at the $r << r_0$ limit, the interaction reduces to a weaker $\log(r)$ dependence.

The variational excitonic wave function, for an anisotropic electronic material such as phosphorene with $m_e^x \neq m_e^y$ and $m_h^x \neq m_h^y$, is written as,

$$\psi(x,y) = 2\sqrt{\frac{2}{\pi\lambda a_x^2}} \exp\left[-\left\{(x/a_x)^2 + (y/a_y)^2\right\}^{\frac{1}{2}}\right], \tag{5.6}$$

where $a_y = \lambda a_x$ is the anisotropic exciton extension along the x (armchair) and y (zigzag) directions, respectively, and treated as variational parameters. Using this form of excitonic wave function $\psi(x,y)$, the expectation value of the kinetic energy is calculated to be,

$$E_k(\lambda, a_x) = \frac{\hbar^2}{4a_x^2}\left[\frac{1}{\mu_x} + \frac{1}{\lambda^2\mu_y}\right]. \tag{5.7}$$

Here μ_x and μ_y are the reduced exciton mass along the x and y directions, respectively. The corresponding potential energy is given by, [190]

$$E_p(\lambda, a_x) = \int\int V_{2D}(x,y)|\psi(x,y)|^2 dxdy. \tag{5.8}$$

The variational exciton binding energy, $E_x^{2D}(\lambda, a_x) = E_k(\lambda, a_x) + E_p(\lambda, a_x)$, is minimized with respect to the variational parameters λ and a_x to obtain the exciton binding energy, and (anisotropic) exciton extension. The parameters in the above model, effective electron and hole masses in different crystallographic direc-

tions and the static dielectric constant are then calculated from the first-principles calculations. In principle, these parameters can be calculated using any level of approximation to the exchange-correlation functional, and here we have used the Heyd-Scuseria-Ernzerhof (HSE06) hybrid functional. [167, 168]

5.3 Results and Discussion

First, we discuss the optical and excitonic properties of pristine phosphorene and investigate the effect of uniaxial strain along the different crystallographic directions. Here, we compare the computationally expensive *GW*-BSE results for these systems with the simplified model calculations. Once we demonstrate an excellent agreement between these methods, we extend our investigation within the simplified model for the realistically large systems, where *GW*-BSE calculations are practically impossible.

We have studied the structural analysis of single layer, bilayer, trilayer, tetra layer, quinta layer, and bulk of prisptine phosphorene. The band gap energy is layer dependendent, it reduces from single layer to bulk phosphorene. The lattice constant b is not layer dependent but a is reducing from single layer to bulk phosphorene.

5.3.1 Pristine phosphorene

We start with the electronic and optical properties of single-layer pristine phosphorene [Figure 5.1(a)] within the *GW*-BSE approach. Due to the long-range Coulomb interactions, these properties of 2D materials are strongly influenced by the vertical separation L_z between the periodic images. [175, 244] As it was shown earlier that the QP band gap converges as $1/L_z$, we extrapolate the gap to $L_z \to \infty$ limit, which we found to be 2.14 eV [Figure 5.1(b) and Table 5.1]. This extrapolated E_g^{QP}

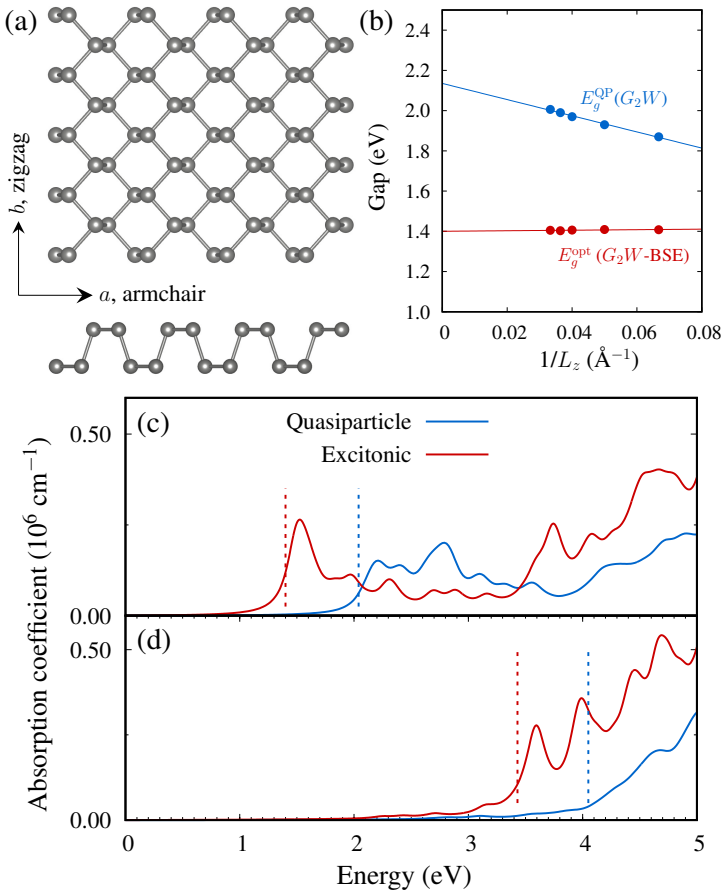

Figure 5.1: (a) The top and side view of single-layer phosphorene is shown indicating the armchair and zigzag crystallographic directions. (b) The QP and optical gaps are calculated with varied vertical separation L_z between the layers and extrapolated to $L_z \to \infty$. The results are in excellent agreement with the experimental results. [200, 255, 263] Absorption coefficient calculated without and with the electron-hole interaction for L_z=30 Å. $\Lambda(\omega)$ shows strong absorption anisotropy between the light polarization along the (c) armchair and (d) zigzag directions. The vertical lines indicate the band edges corresponding to the first absorption peak. The energy difference between the QP and optical gaps indicates strongly bound exciton.

is in excellent agreement with the previous theoretical, [175] and with the two experimental results that are available to date. [200, 263] The high-resolution transmission spectroscopy predicted a transport gap of 2.05 eV, [263] while the photoluminescence excitation spectroscopy suggests a QP gap of 2.2 $\pm$ 0.1 eV. [200] Comparing the present G_2W_0 results with earlier G_0W_0 calculations, [174, 277] we

argue that the self-consistent correction to the self-energy ($\Sigma = iGW$), through the Green's function update, is essential to predict the QP gap correctly. It is important to note here that the optical gap converges much faster than the QP gap with varying L_z [Figure 5.1(b)].

The absorption coefficient $\Lambda(\omega)$ calculated without and with the electron-hole interaction shows strong anisotropy for the light polarizations along the armchair and zigzag directions [Figures 5.1(c)-(d)]. The $L_z \rightarrow \infty$ extrapolated optical gap of 1.40 eV [Figure 5.1(b) and Table 5.1] along the armchair direction is in excellent agreement with the experimental range of 1.30 – 1.45 eV. [200, 255] The large exciton binding energy of 0.74 eV indicates strongly bound exciton in SLP, which is in excellent agreement with the previous GW-BSE calculations [174, 175] and the experimental prediction of 0.9 ± 0.12 eV. [200] Note the absorption edge corresponding to light absorption along the zigzag crystallographic direction lies at a much higher energy, and thus SLP shows linear dichroism. [150]

We calculate the exciton binding within the hydrogenic effective exciton mass model, where the parameters are calculated from a relatively less computationally expensive treatment of the electron exchange and correlation, namely within the HSE06 hybrid functional. The effective carrier masses are highly anisotropic (Table 5.2) as estimated by fitting the HSE06 bands to the parabolic dispersion $E(k) = \hbar^2 k^2 / 2m^*$. The estimated m_e^* is much smaller $0.16m_e$ along the armchair direction than the same along the zigzag direction with $1.40m_e$, where m_e is the electron rest mass. The qualitative picture is the same for the hole, as m_h^* along the armchair direction is much lighter $0.12m_e$ compared to $4.69m_e$ along the zigzag direction. Thus, the effective exciton mass along the armchair direction is much lighter compared to the same along the zigzag direction ($\mu_x << \mu_y$). These results are in good agreement with the previous results. [150, 278] The other parameter of the model, static dielectric constant is calculated from the real part of the complex

dielectric function at zero frequency. The average of static ε along the armchair and zigzag directions is used to calculate the 2D polarizability χ_{2D} (Table 5.1). Using these parameters, the effective exciton mass model predicts an exciton binding energy of 0.79 eV, which is in excellent agreement with the present *GW*-BSE prediction and the experimental estimation (Table 5.1).

The spatial distribution of exciton at the ground state is found to be anisotropic and extended along the armchair direction (a_x=12.26 and a_y=4.90 Å), with spatial anisotropy satisfying the relation, $\lambda = a_y/a_x \sim (\mu_x/\mu_y)^{1/3}$, that was analytically predicted earlier. [190] In an agreement, such elliptic spatial structure of bound hole has recently been observed in black phosphorus through STM tomographic imaging. [279]

5.3.2 Effect of uniaxial strain

The effect of uniaxial strain on the electronic structure of SLP has been studied earlier within the conventional exchange-correlation functional. [154, 261, 278, 280] However, the considerations of self-energy correction and electron-hole interaction are scarce in this regard. Here, we investigate the QP and optical gaps; and the corresponding exciton binding for SLP under $\varepsilon_s^{a/z} = \pm 5\%$ uniaxial strain [Table 5.1 and Figure 5.3(a)-(b)], while the strained lattice is relaxed along the transverse direction.

We earlier reported that the strain energy along the zigzag direction is much higher compared to the same along the armchair direction and thus, straining the SLP along the armchair direction is comparatively easier. [261] Within $-5\% \leqslant \varepsilon_s^{a/z} \leqslant +5\%$ strain range, the $L_z \to \infty$ interpolated gaps E_g^{QP} and E_g^{opt} decrease with uniaxial compressive strain, while they increase with tensile strain (Table 5.1). Clearly, the many-body interaction is comparatively more affected by the uniaxial strain along the armchair direction. Further, the compressive strain triggers a stronger

Table 5.1: With varied L_z, the quasiparticle E_g^{QP} and optical E_g^{opt} gaps are calculated within the G_2W_0 and G_2W_0-BSE approaches, respectively, which are subsequently interpolated to $L_z \to \infty$. The parameters for the simplified exciton model. The uniaxial strain severely affects the many-body interaction in phosphorene, and thus the E_g^{QP}, E_g^{opt}, and E_{x} are altered. The effect of high impurity coverage is also investigated. The exciton binding energies E_{x} calculated within the hydrogenic exciton model compares excellently with those from the accurate but computationally expensive GW-BSE formalism, and available experimental results.

System	E_g^{QP} (eV)	E_g^{opt} (eV)	E_{x} (eV)		$\chi_{2\mathrm{D}}$(Å)
			BSE	model	
SLP	2.05 [263]	1.45 [255]			
Experiment	2.2 ± 0.1 [200]	1.30 [200]	0.9 ± 0.12 [200]		
SLP ($L_z \to \infty$)	2.14	1.40	0.74	0.79	3.55
SLP, $\varepsilon_s^a = -5\%$	1.78	1.03	0.75	0.72	3.95
SLP, $\varepsilon_s^a = +5\%$	2.38	1.51	0.87	0.80	3.36
SLP, $\varepsilon_s^z = -5\%$	1.89	1.12	0.77	0.78	3.77
SLP, $\varepsilon_s^z = +5\%$	2.20	1.41	0.79	0.78	3.79
P_4O	3.22	2.31	0.91	0.81	3.17
P_4S	2.74	1.87	0.87	0.67	4.63

Table 5.2: The effective carrier masses m_e^* and m_h^* along the armchair and zigzag directions; and the average static dielectric constant are calculated within the HSE06 hybrid functional.

System	armchair (x)		zigzag (y)		ε
	m_e^*/m_e	m_h^*/m_e	m_e^*/m_e	m_h^*/m_e	
SLP	0.16	0.12	1.40	4.69	2.60
SLP, $\varepsilon_s^a = -5\%$	0.14	0.12	1.35	3.10	2.78
SLP, $\varepsilon_s^a = +5\%$	0.13	0.12	1.45	3.28	2.51
SLP, $\varepsilon_s^z = -5\%$	0.23	0.13	1.39	2.64	2.70
SLP, $\varepsilon_s^z = +5\%$	0.20	0.14	1.39	2.76	2.71
P_4O	0.76	0.24	0.17	3.42	2.48
P_4S	0.63	0.24	0.80	0.40	3.19

gap renormalization than the tensile strain of equal magnitude. The absorption anisotropy in different crystallographic directions remains intact [Figure 5.3(a)]. Within the applied strain range, the first absorption peak appears within $1-1.50$ eV for light polarization along the armchair direction. In contrast, for the light

polarization along the zigzag direction, the first peak appears above 3 eV and in general shows higher absorbance. Applied uniaxial strain changes the oscillator strength significantly [Figure 5.3(a)]. While the oscillator strength corresponding to the ground state exciton changes by $\pm$10% for $\varepsilon_s^a = \pm$5% strain along the armchair direction, the change is even more significant, $\mp$30% for applied strain $\varepsilon_s^z = \pm$5% along the zigzag direction. Interestingly, for ε_s^z =5%, we observe a competing absorption peak just below its QP gap. Such strain dependent E_g^{QP} and E_g^{opt} may explain the variation observed in photoluminescence peak on different substrates. [200, 255]

The excitons remain strongly bound under applied strain and the G_2W_0-BSE calculated E_{x} varies between 700–900 meV within the investigated strain range. The subsequent excited states reflect a sensitive dependence on the strain dependent dielectric screening [Figure 5.3(b)]. Thus, strain engineering in phosphorene leads to widely tunable photoluminescence energy, enhanced absorption, and multiple exciton formation.

Band gap energy is analyzed using uniaxial strain along armcair and zigzag directions, which is tabulated in Table 5.3. Compressive uniaxial strain reduces the band gap energy, while the tensile strain increases the band gap .

Table 5.3: The effect of uniaxial strain along the armchair and zigzag directions in pristine SLP. The bandgap decreases (increases) with compressive (tensile) strain in the studied strain range of $\varepsilon_{a/z} \leqslant 5\%$. The anisotropy in the exciton extension λ is in excellent agreement with the analytical prediction of $(\mu_x/\mu_y)^{1/3}$, and largely remains unaltered under strain.

System	HSE06 Gap(eV)	λ	$(\mu_x/\mu_y)^{1/3}$	a_x (Å)	a_y (Å)
SLP	1.54	0.40	0.40	12.26	4.90
SLP, ε_a =$-$5%	1.30	0.41	0.41	13.20	5.40
SLP, ε_a =+5%	1.73	0.39	0.39	12.59	4.91
SLP, ε_z =$-$5%	1.39	0.45	0.45	11.62	5.19
SLP, ε_z =+5%	1.65	0.44	0.44	11.65	5.17

Next, we investigate the effective carrier masses with a varied uniaxial strain within the HSE06 functional. In agreement with an earlier report, [278] the effective electron and hole masses are severely affected by strain (Table 5.2), however their qualitative anisotropic nature remains intact with $\mu_x << \mu_y$. These m_e^* and m_h^* are used to estimate E_x for the strained SLP within the hydrogenic model, which are in excellent agreement with the more accurate *GW*-BSE results (Table 5.1). Further, the spatial anisotropy of exciton $\lambda \sim (\mu_x/\mu_y)^{1/3}$ remain similar under strain as in pristine SLP (Table 5.3). These results essentially validate the applicability of the present hydrogenic model for the anisotropic 2D phosphorene.

Figure 5.2 represents the band gaps of pristine SLP, strained SLP are calculated with different functionals, such as HSE06, GW and BSE formalism. The excitonic binding energy is calculated. The variation in band gap energy is more when the strain applied along the armchair direction than that of zigzag direction.

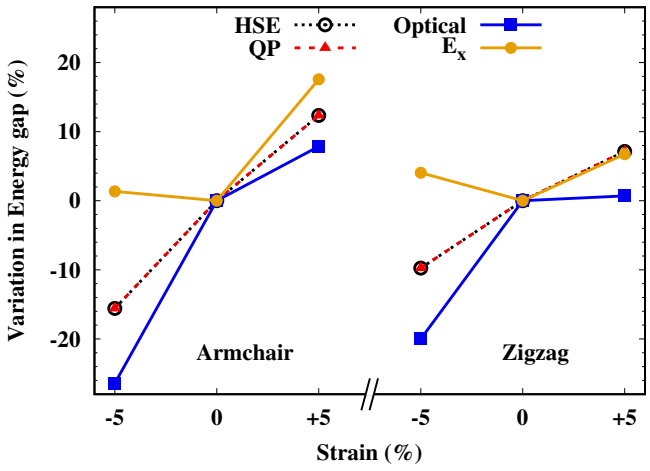

Figure 5.2: Differential response of energy gaps on the applied uniaxial strain calculated at the various theoretical hierarchy. The relative variation in the exciton binding is also tracked. In comparison, the strain along the armchair direction and a compressive strain have greater effects.

5.3.3 Effect of impurity coverage

The presence of lone-pair electrons in phosphorene makes it reactive and can easily absorb impurities with a strong binding energy resulting from the P to impurity change transfer. We have earlier discussed O, S and N chemisorption with varied impurity coverage and it was concluded that 0.25–0.5 monolayer (ML) O/S coverages become conducive to both water redox reactions. [258] While the exciton binding energy plays an important role in efficient charge separation and in turn affects the performance of a catalytic device, the SLP derivatives with such low impurity coverages are very difficult to investigate within the *GW*-BSE formalism. Thus at first, we investigate the derivatives with high 1 ML O/S coverages, P_4O and P_4S that can be represented by a small cell, and compare the *GW*-BSE results with the effective mass model. The SLPs with 1 ML O and S coverage are found to be indirect gap semiconductors, and both QP and optical gaps are severely altered (Table 5.1). While for the 1 ML O-covered SLP the extrapolated E_g^{QP} and E_g^{opt} increase upon impurity coverage, the picture is reversed for the 1 ML S-covered SLP. The absorption edge, calculated by considering the electron-hole interaction, lies at a much lower energy than the same calculated without the interaction (Figure 5.3). This observation indicates strongly bound excitons in these derivatives similar to the pristine SLP (Table 5.1). The qualitative anisotropic feature in the carrier effective masses are intact but are severely altered in all crystallographic directions (Table 5.5). However, the anisotropy in effective exciton mass disappears with $\lambda \sim 1$, and thus the corresponding exciton extension becomes isotropic with 1 ML coverage (Table 5.5).

The effective masses of charge carriers are calculated for O/S coverages on SLP. The charge carriers are heavier along zigzag direction than that of armchair direction, which are tabulated in Table 5.4.

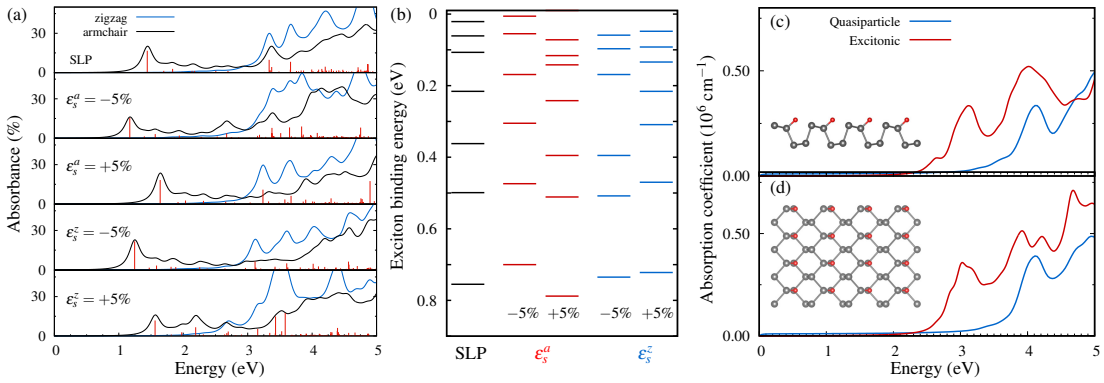

Figure 5.3: (a) The effects of strain on the absorbance and dipole oscillator strength calculated including the electron-hole interaction within the *GW*-BSE formalism (L_z = 30 Å). The vertical lines indicate the relative dipole oscillator strengths and are significantly affected by the applied uniaxial strain. (b) The corresponding exciton spectra for the pristine and uniaxially strained SLP. Strain-dependent dielectric screening influences the spectra. The $E = 0$ eV refers to the quasiparticle gap, and excitons generated from the transitions with non-vanishing dipole oscillator strengths are shown. The relative oscillator strengths are shown in (a). Absorption coefficient calculated without and with the electron-hole interaction (L_z = 30 Å) for the light polarization along (c) armchair and (d) zigzag directions, shown for 1 ML O coverage. The absorption edges are calculated from the corresponding E vs $(E\Lambda)^{1/2}$ plot for this indirect gap semiconductor. The absorption anisotropy along the armchair and zigzag directions is greatly reduced due to monolayer impurity coverage. The insets show the side and top views of SLP with 1ML O coverage.

Table 5.4: Effective carrier masses for SLP with O/S impurity coverages calculated within HSE06 functional. These parameters will be used with the hydrogenic model to calculate the exciton binding energy E_x and the corresponding exciton extension anisotropy λ.

System	armchair		zigzag	
	m_e^*/m_e	m_h^*/m_e	m_e^*/m_e	m_h^*/m_e
0.33 ML O	0.31	0.16	0.43	3.15
0.50 ML O	0.19	1.48	0.46	3.71
1 ML O	0.76	0.24	0.17	3.42
0.33 ML S	0.60	0.16	0.94	2.61
0.50 ML S	0.33	1.16	0.52	1.27
1 ML S	0.63	0.24	0.80	0.40

Table 5.5 explores the excitonic binding energy trends, which are calculated for O/S coverages on SLP. In case of O coverage on SLP, exciton binding energy increases from 0.33 ML to 0.50 ML coverage, and reduces from 0.50 to 1.0 ML coverage on SLP. The excitonic binding energy is increased from 0.33 to 1.0 ML coverage of S on SLP.

Table 5.5: The dielectric constant ε (avg) and χ_{2D} calculated for SLP with O/S impurity coverages within HSE06 functional. These parameters are used with the hydrogenic model to calculate the exciton binding energy E_x and the corresponding exciton extension anisotropy λ.

System	ε (avg)	χ_{2D} (Å)	E_x (eV)	λ
0.33 ML O	2.56	3.33	0.81	0.65
0.50 ML O	2.66	3.54	0.85	0.74
1 ML O	2.48	3.17	0.81	1.04
0.33 ML S	2.74	3.62	0.85	0.56
0.50 ML S	2.82	3.81	0.86	0.88
1 ML S	3.19	4.63	0.67	0.86

Furthermore, the E_x calculated within the *GW*-BSE formalism are in excellent agreement with those calculated using the hydrogenic model (Table 5.1), which implies the applicability of this simplistic model to investigate exciton in such phosphorene derivatives with impurity coverage.

The SLPs with sub-monolayer coverages are both thermodynamically and kinetically stable. Further, the band edges align with the redox potentials for water splitting reactions for SLPs with 0.33−0.5 ML oxygen/sulfur coverages. [258] Carrier effective masses in all directions are severely affected by the impurity coverage, and the resulting exciton binding energies are found to be high (Table 5.5). The calculated E_x within the hydrogenic model is found to be 0.81 and 0.85 eV (0.85 and 0.86 eV) for 0.33 and 0.5ML oxygen (sulfur) coverages. Such high exciton binding makes charge separation difficult in optoelectronic and catalytic devices. Thus, although the conduction and valence bands in these derivatives align with

the redox potentials, the catalytic activity is expected to be negatively impacted due to high exciton binding. On the other hand, the high absorption coefficient [Figure 5.3(c)-(d)] and robust exciton with high binding energy are desirable features for light emitting device applications. In this regard, the impurity covered phosphorene can extend such application to green-light emission.[281, 282] The anisotropy in exciton extension is in agreement with the analytical estimation of $\lambda \sim (\mu_x/\mu_y)^{1/3}$ and monotonically decreases with increasing coverage (Table 5.5).

5.3.4 Exciton renormalization in few-layer, heterostructure phosphorene

While the layer-dependent evolution of gaps has been studied in few-layer phosphorene, [150, 174, 283, 284] we have studied the structural analysis of single layer, bilayer, trilayer, tetra layer, penta layer, and bulk of prisptine phosphorene. From the Table 5.6, we can conclude that the band gap energy is layer dependendent, it reduces from single layer to bulk phosphorene. The lattice constant along the armchair direction (b) is not layer dependent, but along the zigzag direction(a) is reducing from single layer to bulk phosphorene.

It is intriguing to investigate the layer-dependent exciton binding. The effective screening increases with layer thickness and in addition, the carrier masses along different crystallographic directions are also expected to be modified. The evolution in lattice parameters with increasing layer thickness agrees well with the previous prediction and converges to the bulk values (Table 5.6). [150] Further, the bandgap in few-layer phosphorene decreases with thickness and converges to the value for black phosphorus [Figure 5.4(b)]. The calculated bulk gap of 0.26 eV agrees reasonably well with the experimental measurement of 0.33 eV. [285] Considering the fact that the gaps are underestimated within the HSE06 functional, it is imperative to investigate its qualitative dependence on thickness. A power-law fit

Table 5.6: Evolution of lattice parameters with layer thickness in few-layer phosphorene. Results are in good agreement with the experimental lattice parameters of bulk black phosphorus (BP). Lattice parameters slightly differ within different treatment of van der Waals interaction. For the vdW-D3 correction we used the zero damping method. The optimized structures with optB88 and D3 vdW corrections have been used to calculate the HSE06 bandstructure.

		Lattice parameter (Å)		E_g (eV)
		a	b	
1L	vdW-optB88	4.58	3.32	1.54
	vdW-D3	4.59	3.30	1.53
2L	vdW-D3	4.51	3.30	1.03
3L	vdW-D3	4.49	3.30	0.78
4L	vdW-D3	4.47	3.30	0.64
5L	vdW-D3	4.45	3.30	0.51
Bulk BP	vdW-D3	a=4.42, b=3.31, c=10.67		0.26
	vdW-optB88	a=4.48, b=3.34, c=10.72		0.26
	Experiment [273, 274]	a=4.37, b=3.31, c=10.47		0.33 [285]

$E_g = aN_\ell^{-\alpha} + c$, with N_ℓ being the number of layers, indicates that E_g decays much slower as $\alpha = 0.83$ than the usual quantum confinement with $\alpha = 2$. While $\alpha < 2$ is generic in weak van der Waals stacked two-dimensional materials, calculated α in few-layer phosphorene is much smaller compared to MoS_2, where $\alpha = 1.10$. [286]

The effective electron screening increases with thickness N_ℓ, and the static dielectric constant ε in few-layer phosphorene increases with the number of layers. The anisotropic ε in black phosphorus (ε_x = 14.75, ε_y = 10.87, ε_z = 8.68) are consistent with the experimental measurement of 16.5, 13 and 8.3 along the armchair, zigzag and perpendicular directions, respectively. [287] The dependence of χ_{2D}, calculated using the average of anisotropic static ε, indicates increasing screening with thickness [Figure 5.4(a)]. Figure 5.5 represents the electronic band structure of bulk phosphorene, which has direct band gap at Γ point.

The carrier effective masses of bulk phosphorous are calculated and compared with the references in the Table 5.7.

Effective carrier masses are mostly unaffected in few-layer phosphorene except

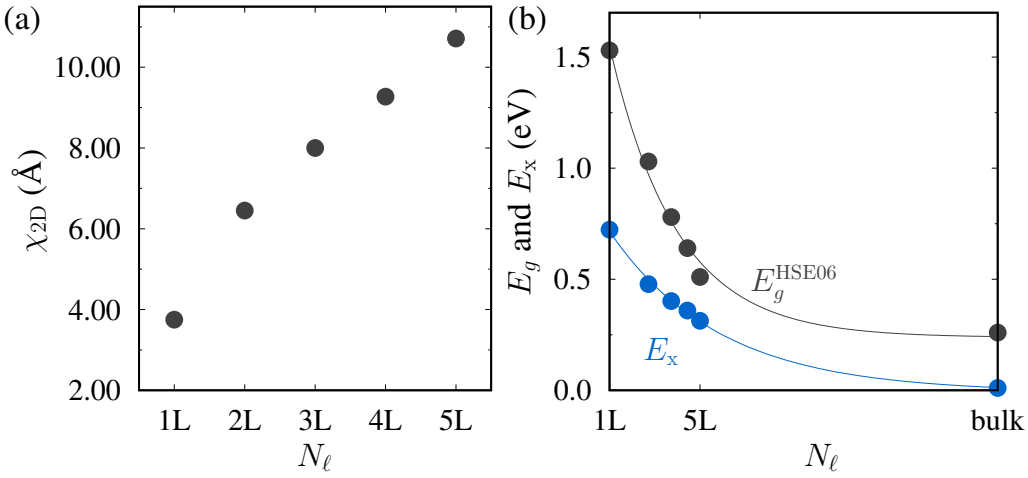

Figure 5.4: (a) Calculated $\chi_{2D} = (\varepsilon - 1)L_v/4\pi$ increases with layer thickness N_ℓ indicating an increase in electron screening. (b) The renormalization of bandgap E_g and exciton binding E_x in few-layer phosphorene shows a power-law dependence with the layer thickness and both quantities converge very slowly to the corresponding bulk value. The variation in exciton binding is largely determined by the effective hole mass m_h^* along the zigzag direction, in addition to the change in effective electron screening.

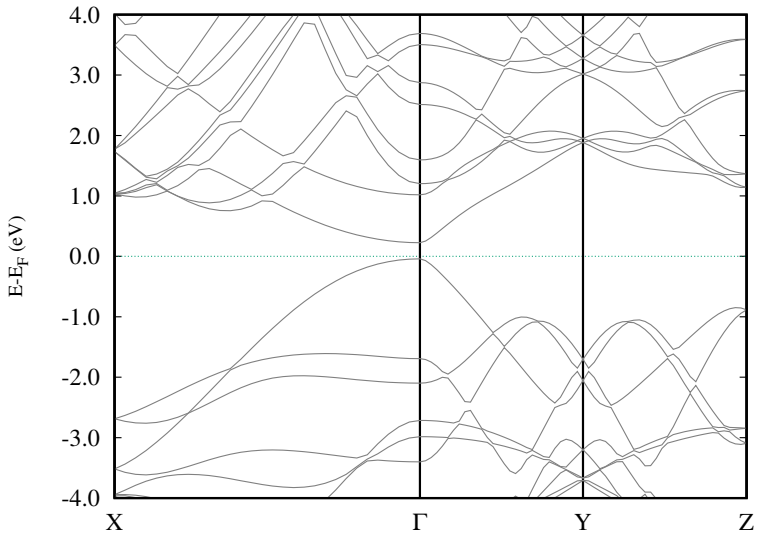

Figure 5.5: Electronic band structure for bulk phosphorene with in the HSE06 function.

for the hole mass along the zigzag direction, which exhibits a strong layer dependence (Table 5.8). The calculated m_h^* along this direction decreases sharply with

Table 5.7: Calculated carrier effective masses calculated for bulk BP within the HSE06 hybrid functional. Present results compare well with an earlier theoretical calculation and experimental estimation.

Bulk P	a, armchair		b, zigzag		c, perpendicular	
	m_e^*/m_e	m_h^*/m_e	m_e^*/m_e	m_h^*/m_e	m_e^*/m_e	m_h^*/m_e
Present	0.12	0.10	1.39	0.82	0.17	0.30
Ref. [150]	0.12	0.11	1.15	0.71	0.15	0.30
Experiment [288]	0.082	0.078	1.027	0.648	0.128	0.28

thickness N_ℓ, which is in agreement with a previous prediction. [150] To confirm the evolution of effective carrier masses with N_ℓ, we calculated the same for the bulk black phosphorus, which compares well with the experimental values (Table 5.7). [288]

The excitonic binding energy is layer dependent, it decreases from single layer to bulk phosphorous. The dielectric constant and 2D polarizability increases from single layer to bulk phosphorous, which are tabulated in the Table 5.8.

Consequently, the renormalization of exciton binding in few-layer phosphorene [Figure 5.4(a)] is dictated by the strong dependence of effective hole mass along the zigzag direction and the increase in effective screening with layer thickness. This result is in contrast to the assumption that the exciton binding and thus its variation is independent of carrier effective mass. [191, 289] The large exciton binding sharply decreases from 0.72 eV in 1L to 0.48 eV in 2L and 0.31 eV in 5L phosphorene, which is still much higher than the corresponding bulk value. We estimated the Mott-Wannier exciton binding in black phosphorus $E_{\rm x}^{\rm 3D} = (\mu/\varepsilon^2)R_\infty$ to be about 11 meV, which is much smaller than k_BT at room temperature, and also much smaller than the same in bulk transition-metal dichalcogenides. [252] A similar power-law fit with $\alpha = 0.53$ indicates a much slower dependence of $E_{\rm x}$ on thickness than for E_g. Further, the exciton extension in few-layer phosphorene remains anisotropic while the degree of anisotropy decreases (λ increases) mono-

Table 5.8: Effective carrier masses and χ_{2D} for few-layer phosphorene calculated within HSE06 functional. These parameters are used with the hydrogenic model to calculate the exciton binding energy E_x and the corresponding exciton extension anisotropy λ. Exciton binding for the bulk BP is calculated within the Mott-Wannier model.

System	vdW	armchair		zigzag	
		m_e^*/m_e	m_h^*/m_e	m_e^*/m_e	m_h^*/m_e
1L	optB88	0.16	0.12	1.40	4.69
1L	D3	0.12	0.10	1.38	5.34
2L	D3	0.12	0.11	1.45	1.95
3L	D3	0.12	0.11	1.43	1.76
4L	D3	0.13	0.12	1.42	1.25
5L	D3	0.13	0.12	1.41	1.03
BP	D3	0.12	0.10	1.39	0.82
System	vdW	ε (avg)	χ_{2D} (Å)	E_x (eV)	λ
1L	optB88	2.60	3.55	0.793	0.40
1L	D3	2.69	3.75	0.723	0.37
2L	D3	4.59	6.45	0.478	0.42
3L	D3	5.98	8.00	0.402	0.46
4L	D3	6.86	9.27	0.359	0.49
5L	D3	7.51	10.71	0.313	0.57
BP	D3	11.43	–	0.011	–

tonically with thickness (Table 5.8).

Black phosphorous is often encapsulated to avoid degradation and restore the intrinsic electronic properties. [145, 200, 266] The hexagonal boron nitride (h-BN) was demonstrated to be a good candidate material for this purpose. [269–271] Thus, it would be worth investigating that how the electronic structure and effective dielectric screening are affected due to the substrate and capping. In this regard, we investigate the h-BN/SLP and h-BN/SLP/h-BN heterostructures [Figure 5.6(a) and (b)]. To minimize the lattice strain in the phosphorene layer, we used a 1×3 supercell of phosphorene with an orthorhombic 1×4 cell of h-BN. Due to its puckered structure, the phosphorene lattice is relatively much softer than the h-BN and can easily sustain a large strain. Thus, in relaxed geometry, the strain is

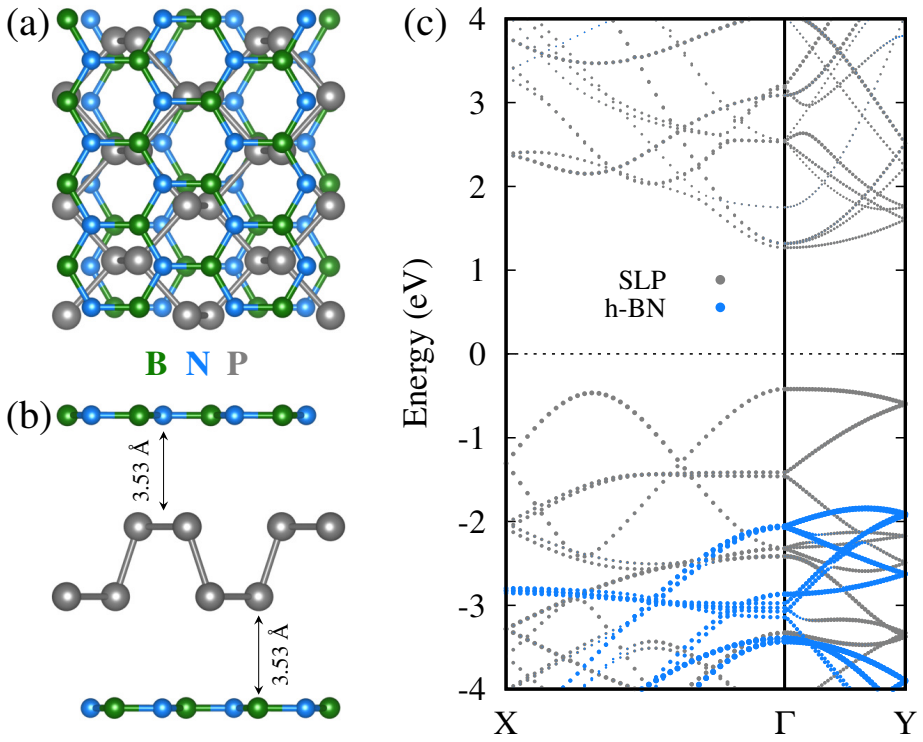

Figure 5.6: (a)-(b) The top and side view of the h-BN/SLP/h-BN van der Waals encapsule. The structure is optimized using the PBE+D3-vdW functional with zero damping. The encapsulation induces a compressive (tensile) strain of 5.2% (1.3%) in the phosphorene layer along the armchair (zigzag) direction. (c) The valence band maxima and conduction band minima originate from the SLP and thus indicate a type I band alignment. While the apparent band structure looks similar to the pristine SLP, the corresponding carrier effective masses are severely altered, which in turn modifies the exciton character.

induced in the phosphorene layer while the h-BN lattice is mostly unaltered (Table 5.9). The bandgap of SLP in these heterostructures is only slightly modified compared to the pristine case (Table 5.10). We attribute this small change in the gap to the induced strain in the phosphorene layer in the heterostructure. These results are consistent with the previous calculations. [290, 291]

We studied the heterostructures of h-BN/SLP, and h-BN/SLP/h-BN. The SLP is compressed along the armchair direction, and expanded along the zigzag direction. The band gap is decreases in h-BN/SLP, and increases in h-BN/SLP/h-BN, which can be concluded from Table 5.9.

Table 5.9: Lattice parameter for the h-BN/SLP heterostructure and the h-BN/SLP/h-BN encapsulate. The strain along armchair direction(a), and strain along zigzag direction (b)in phosphorene are tabulated .

System	Lattice parameters (Å)		Strain in SLP	
	a	b	$\varepsilon_a(\%)$	$\varepsilon_z(\%)$
Pristine SLP	4.59	9.90	–	–
Pristine h-BN	4.35	10.05	–	–
SLP/h-BN	4.36	10.02	−5.01	1.21
h-BN/SLP/h-BN	4.35	10.03	−5.23	1.31

Heterostructure of SLP and hBN are studied, where SLP/h-BN and h-BN/SLP/h-BN induce strain in the SLP. Due to the induced strain, the band gap energy differs from pristine SLP, which are tabulated in the Table 5.10.

Table 5.10: HSE06 band gap of the h-BN/SLP heterostructure and the h-BN/SLP/h-BN encapsulate. The gap is mostly unaffected, while the slight change in gap is attributed to the strain induced in the SLP layer in the heterostructures. Note that, while the SLP layer in both the heterostructures have similar lattice parameters(Table 5.9), they produce different bandgaps. This is largely due to the change in the distance between the two-half layers of SLP (Figure 5.7).

System	Bandgap (eV)
Pristine SLP	1.53
Pristine h-BN	5.71
SLP/h-BN	1.45
SLP in SLP/h-BN	1.34
h-BN/SLP/h-BN	1.73
SLP in h-BN/SLP/h-BN	1.65

Figure 5.7 shows that there is a tiny difference in the distance between SLP and h-BN of SLP/h-BN and h-BN/SLP/h-BN heterostructures, which leads to different band gap for SLP/h-BN and h-BN/SLP/h-BN heterostructures (Table 5.10).

The carrier effective masses of h-BN/SLP, h-BN/SLP/h-BN are calculated, 2D polarizability, exciton binding energy are tabulated (Table 5.11). The effective masses

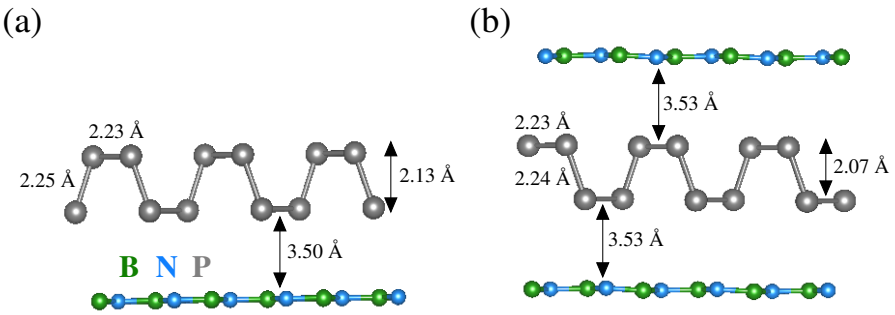

Figure 5.7: (a) SLP/h-BN and (b) h-BN/SLP/h-BN heterostructures. The vertical separation between the layers changes slightly in these heterostructure. While the strain induced in the SLP layer for both these heterostructures are very similar, the distance between the two half-layers of phosphorene differs substantially by about 0.06 Å, which in turn is responsible for very different bandgap.

are not ultered much in the heterostructures, and 2D polarizability, exciton binding energy are decreased from h-BN/SLP, h-BN/SLP/h-BN.

Table 5.11: Carrier effective masses, χ_{2D}, exciton binding E_x and spatial anisotropy λ for phosphorene heterostructures with h-BN.

Heterostructure	a, armchair		b, zigzag	
	m_e^*/m_e	m_h^*/m_e	m_e^*/m_e	m_h^*/m_e
SLP/h-BN	0.26	0.23	0.68	4.51
h-BN/SLP/h-BN	0.23	0.32	0.28	4.60
Heterostructure	ε (avg)	χ_{2D} (Å)	E_x (eV)	λ
SLP/h-BN	3.29	3.71	0.55	0.59
h-BN/SLP/h-BN	3.08	3.44	0.53	0.81

Previously, the exciton binding energy was proposed to be independent of the effective mass. [191] In contrast, within the present model, E_x is determined by the effective mass and 2D polarizability. Moreover, the spatial anisotropic structure is directly related to the carrier effective masses, $\lambda \sim (\mu_x/\mu_y)^{1/3}$. Thus, in addition to the dielectric environment, any change in the intrinsic electronic structure in phosphorene due to the substrate and capping layer is important to consider for a correct description of the exciton. Indeed, the effective carrier mass

in the phosphorene layer is affected by h-BN (Table 5.9), which along with the electron screening from the h-BN layer reduces the exciton binding. The exciton binding is renormalized to 0.55 eV for the SLP/h-BN heterostructure, while the presence of a second h-BN layer in the h-BN/SLP/h-BN encapsulation does not alter the exciton binding further (0.53 eV). The excitons in these heterostructures are generated in the phosphorene layer, and no interlayer exciton is possible [Figure 5.6(c)]. Further, the spatial anisotropy of excitons in these heterostructures is reduced (Table 5.11). Similar renormalization of exciton binding was predicted earlier for Al_2O_3/phosphorene/h-BN encapsulation, and phosphorene on SiO_2 or PDMS substrates. [289, 292, 293]

In this context, it should be noted here that both SLP/h-BN and h-BN/SLP/h-BN represent a special case of intralayer exciton owing to the band structure in Figure 5.6(c), which is well described within the present model. Moreover, the present model can be extended to the interlayer excitons as was discussed earlier for the MoS_2/h-BN/WSe_2 heterostructures. [294]

5.4 Summary

We have studied the quasiparticle and optical properties of phosphorene and investigated the role of uniaxial strain, and impurity coverages. The excitonic properties described within a tractable anisotropic hydrogenic model exhibit excellent agreements with those calculated by explicitly considering the electron-hole interaction within the *GW*-BSE formalism. In contrast to the previous assumption, the exciton binding strongly depends on effective carrier masses, which further determines the anisotropic spatial extension of excitons. Similar to the pristine SLP, exciton in strained and impurity covered phosphorene remain strongly bound. However, the absorption edge, the corresponding dipole oscillator strength and

the anisotropy in spatial extension are severely altered. Owing to a severe alteration in the effective hole mass along the zigzag direction and increase in the electron screening, the exciton binding is greatly renormalized in few-layer phosphorene. In contrast, the exciton binding is relatively less affected in the h-BN and phosphorene heterostructures. The robust large exciton binding energy and tunable photoluminescence in encapsulated and impurity covered phosphorene derivatives raise their prospective applications in light-emitting devices. Further, the results indicate that the present model will be applicable to other phosphorene based superstructures and other two-dimensional anisotropic materials.

CHAPTER 6

JANUS TRANSITION-METAL DICHALCOGENIDE MONOLAYERS AS PHOTOCATALYSTS

Transition metal dichalcogenides have attracted much attention due to their promise in photocatalysis. Here, within the first-principles calculations and a hydrogenic exciton model, we demonstrate that the Janus counterparts have superior properties in this regard. We observe the required band alignment with the redox potentials, high optical absorption in the visible region, and low exciton binding, all pointing toward superior quantum efficiency. Present results are in good agreement with the available experimental data. The internal electric field in this Janus materials, which is not otherwise present in the natural transition-metal dichalcogenides, is responsible for the current observations. Our primary goal is to establish the applicability of the hydrogenic exciton model in a variety of natural and Janus dichalcogenides through rigorous comparisons with more accurate $GW+$ BSE method and experimental data. These results will be published in future.

6.1 Introduction

Photocatalysis attracted much interest of researchers due to its eco-friendly nature, where photocatalytic water splitting into hydrogen and oxygen is one of the optimistic and emerging technology. Two-dimensional (2D) materials, in this regard, have attracted much attention due to their large active surface, superior optical absorption, and concurrently tunable electronic structure. The electronic and optical properties of 2D materials are very sensitive to the external perturbations. [8, 37, 295–297] Due to the quantum confinement, the physical and chemical properties of these 2D materials differ much from their bulk counterparts.

Transition metal dichalcogenides (TMDCs) have showed great potential in this regard. The general chemical formula of TMDCs is MX_2, where M = Transition metal, X = halogen, its three sub-layers are composed with one metal layer sandwiched between the two halogen layers. The intra-layer has covalent M−X bonding, whereas the individual layers are held together by the weak van der Waals interactions. The single-layers of these TMDCs have been also synthesized and their electronic and optical properties are throughly investigated. [8, 298–305] Interestingly, the asymmetric counterparts of the TMDCs known as Janus TMDCs (JTMDCs) (MXY, where M = Mo/W, X/Y = S, Se, Te) have recently been synthesized, which inherit the advantages of 2D TMDCs. Moreover, these new materials provide an additional degree of freedom to tune their electronic, optical and thus photocatalytic properties. Due to the broken inversion-symmetry induced by the difference in Pauling electronegativity on both sides of the TM-layer, the JTMDCs experience an internal electric field, which breaks the band gap criteria for photocatalytic for water splitting. Thus, while TMDCs have been exhaustively investigated in this context, it is imperative to study the electronic, optical and excitonic properties of JTMDCs and compare them with the TMDCs. It is also expected that

the he photo-generated charge carriers may be separated easily due to the presence of intrinsic electric field, which can reduce the recombination rate of charge carriers and promotes the efficiency of photocatalyst. Recently, the Janus MoSSe in the 2H-phase has been successfully synthesized by fully replacing one of the S (Se) layers with Se (S) atoms within MoS_2 ($MoSe_2$) through the chemical vapor deposition (CVD) method. [306, 307] The intrinsic dipole-moment induces a vertical piezoelectric response in MXY, which is absent in the pristine single layer of MoS_2. The piezoelectric response in Janus MoSSe can be improved under the uniaxial or biaxial strains. [308] Further, JTMDCs are reported as photocatalysts for water splitting. [309, 310]

Within the first-principles calculations, in this Chapter, we report the structural, electronic, and optical properties of JTMDCs and compare them with their respective TMDCs. Following the success of our previous two-dimensional hydrogenic exciton model, we also investigate the excitonic properties. The parameters of the model, effective carrier mass and 2D polarizability, are derived from the first-principles calculations. Results of this model are compared with more accurate but expensive *GW*-BSE calculations, which show excellent agreement. Due to the intrinsic electric field, the exciton binding is renormalized, and these JTMDCs show excellent applicability in photocataytic applications.

6.2 Methodology

All the calculations were done by Vienna ab-initio simulation package (VASP) [162, 163] based on the projected augmented wave (PAW) method. [164] The electronic exchange-correlation energy was treated by generalized-gradient approximation of Perdew-Burke-Ernzerhof (GGA-PBE) for structure relaxation. [165] The kinetic energy cut-off is 500 eV, and all the structures are relaxed until the force acts

on the atom is 0.01 eV/Å. To consider the weak vdW interactions vdW-DF-optB86 was used. [230, 231] A Γ centred 17×17×1 k-mesh was used with 30Å vacuum. The electronic and optical properties were calculated by hybrid Heyd-Scuseria-Ernzerhof (HSE06 + SOC) functional. [167] The spin-orbit coupling was treated in electronic and optical properties calculations. The optimized structures with the PBE exchange-correlation functional are used for *GW*-BSE calculations. Two self-consistent updates for the Green's function G_2W_0 are found to be sufficient to converge the quasiparticle electronic structure. [121, 122] Electron-hole interactions are incorporated within the BSE formalism [123, 242, 262] to calculate the corresponding optical gaps.

6.3 Results and Discussion

In this study, we have considered Mo and W based TMDCs (MoS_2, $MoSe_2$, $MoTe_2$, WS_2, WSe_2, WTe_2,) and their combinatorial Janus counterparts (MoSSe, MoSTe, MoSeTe, WSSe, WSTe, and WSeTe). First we discuss the evolution of their structural, and electronic properties; and subsequently move on to their optical, excitonic and photocatalytic properties.

6.3.1 Single-layer of TMDCs and JTMDCs

In MX_2 TMDCs, one metal layer (M = Mo and W) is sandwiched between two chemically identical chalcogen layers (X = S, Se, Te). Similarly, the Janus TMDCs monolayers have trigonal prismatic symmetry, however, the metal layer is sandwiched between two different chalcogen atom in MXY (Figure 6.1). Calculated lattice parameters are tabulated in Table 6.1, where we make a few observations. (a) The lattice parameters increases as the chalcogen size increase. Since the Janus TMD is formed by replacing one of the X layer with the Y atoms in pristine MX_2,

the lattice parameters of the resulting MXY monolayer is about the average of MoX_2 and MoY_2. Overall the present results are in good agreement with the available experimental results. (b) Due to the difference in electronegativity and atomic number of X and Y atoms, there are inequivalent M−X and M−Y bonds. (c) The bond lengths of JTMDCs monolayers follow the order of d(M-Te)> d(M-Se)> d(M-S), which results in a planar bending strain. For example, the Mo−Te bond is 0.16 Å larger than that of the Mo-Se in MoSeTe, that results in bending from Te plane to Se plane. The bending strain (ε_d) of the JTMDCs monolayers can be defined as, $\varepsilon_d = [(d_{M-Y} - d_{M-X})/d_{M-X}] \times 100\%$. Calculated ε_d is tabulated in Table 6.1, which increases with increasing mismatch between the ionic radii of chalcogen atoms in MXY. Therefore, MoSSe has the lowest bending strain (4.6%) compared to MoSeTe (6.27%) and MoSTe (11.5%). WXY monolayers also show a similar trend.

Table 6.1: Calculated lattice parameter a, and bond lengths d for the TMDCs and JTMDCs are listed and lattice parameters are compared with the available experimental data. The bending strain (ε) is calculated for the MXY monolayers.

MX_2/MXY	a(Å)	Experimental a(Å)	d_{M-X} (Å)	d_{M-Y} (Å)	ε_d(%)
MoS_2	3.16	3.16 [311]	2.41	-	-
MoSSe	3.23	3.22 [306]	2.42	2.53	4.55
$MoSe_2$	3.30	3.29 [312]	2.54	-	-
MoSTe	3.34	-	2.43	2.71	11.52
MoSeTe	3.41	-	2.55	2.71	6.27
$MoTe_2$	3.52	3.52 [313]	2.72	-	-
WS_2	3.17	3.15 [314]	2.41	-	-
WSSe	3.23	-	2.42	2.54	4.96
WSe_2	3.29	-	2.54	-	-
WSTe	3.34	-	2.44	2.72	11.48
WSeTe	3.41	-	2.56	2.72	6.25
WTe_2	3.53	3.48 [315]	2.73	-	-

As shown in the Figure 6.1(c) and discussed earlier, an electrostatic potential difference is generated in the MXY monolayers due to different electronegativity of the surfaces. Charge density redistribution induces an intrinsic dipole in the

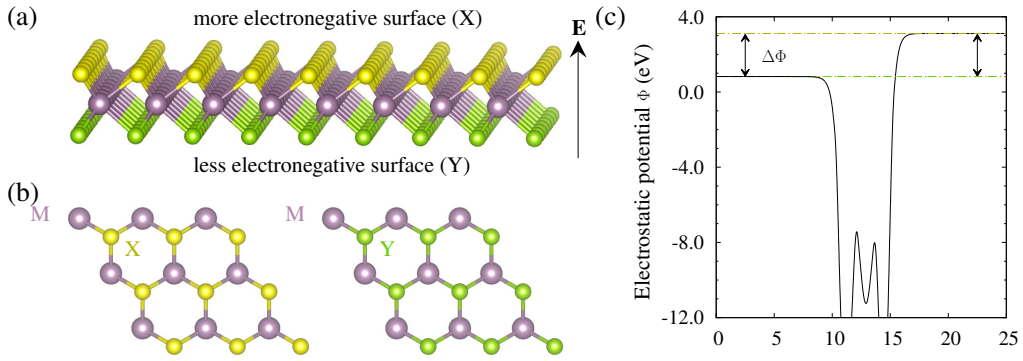

Figure 6.1: (a) The side view of the single-layer Janus JTMDCs (M= Mo, W, X/Y = S, Se and Te), where the out-of-plane symmetry is broken, and an internal electric field **E** is generated due to the difference in electronegativity of chalcogen atoms. (b)Top view of JTMDCs with two different chalcogen atoms X and Y. (c) Electrostatic potential difference is produced between the two different halogen atoms in JTMDCs. Figure adopted from reference. [316]

out-of-plane direction, which gives rise to an internal electric field pointing from the less electronegative surface to the more electronegative surface as shown in Figure 6.1. We calculate this electrostatic potential difference ($\Delta\Phi$) within the first-principles method, which is 0.76, 1.49, 0.80, 0.68, 1.45, and 0.87 for MoSSe, MoSTe, MoSeTe, WSSe, WSTe, and WSeTe, respectively. In the context of photocatalytic water splitting, this $\Delta\Phi$ relaxes the strict band gap criterion. [309]

Now we turn our attention to the electronic structure of the TMDC and JTMDCs (Figure 6.2 and Figure 6.3). First we discuss the results within the conventional DFT, where the exchange-correlation is treated within the hybrid HSE06 functional and the spin-orbit coupling is explicitly treated. All Mo and W based MX_2 monolayers are found to be semiconducting with a direct gap at the K-valley. In agreement with the available experimental and earlier theoretical results, we observe 2.10, 1.84, 1.43, 2.10, 1.78, and 1.19 eV gaps for MoS_2, $MoSe_2$, $MoTe_2$, WS_2, WSe_2, and WTe_2, respectively. [303–305] Notice, that the gap monotonically decreases as we move along S $\rightarrow$ Se $\rightarrow$ Te. We also observe a spin-orbit splitting at the top of the valence band at the K-point.

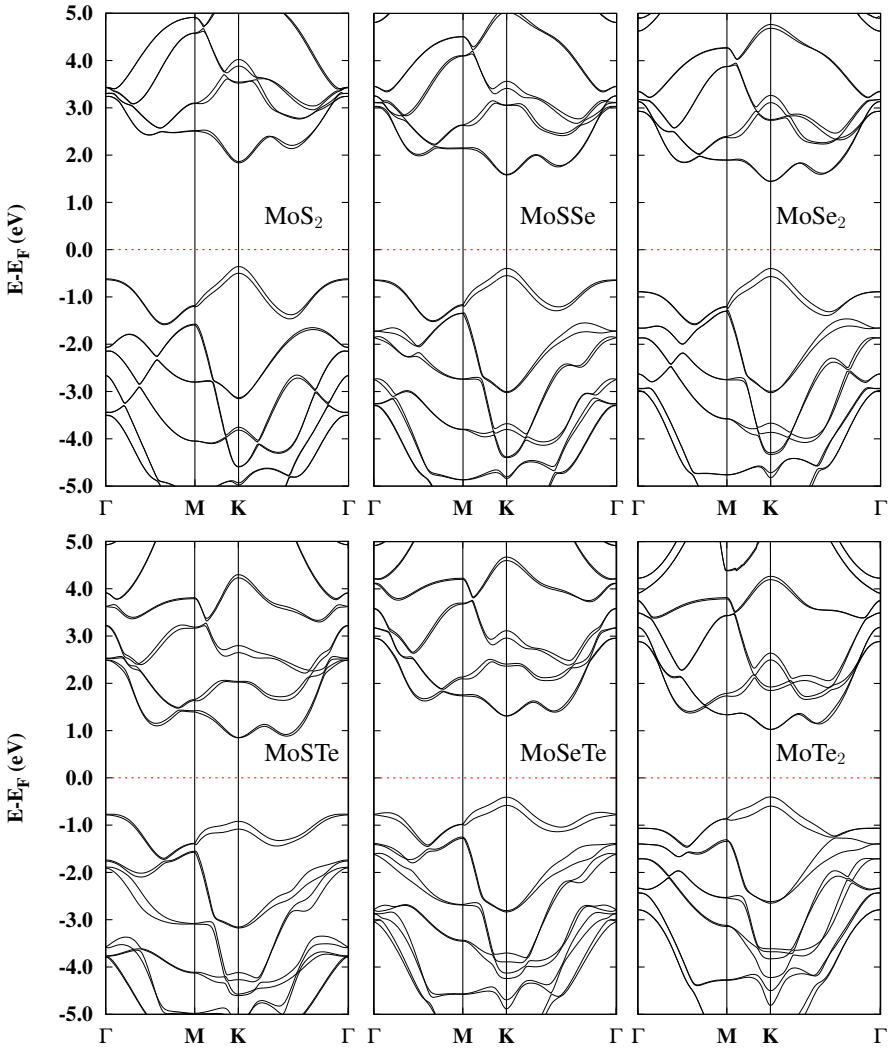

Figure 6.2: Band structures of MoS_2, MoSSe, $MoSe_2$, MoSTe, MoSeTe, and $MoTe_2$ which have direct band gap at K-point except MoSTe. MoSTe has indirect gap, where VBM lies at Γ and CBM is at K-point.

The electronic structures of the JTMDCs are qualitatively similar with a few minor exceptions (Figure 6.2 and Figure 6.3). All of the studied JTMDC monolayers are semiconducting, and nature of the gap at the K-point is direct, as in the MX_2 monolayers. Only exception is found for the cases of MoSTe, and WSTe, where we observe an indirect gap. While the valence band maximum (VBM) moves to the Γ-point in both these monolayers, the conduction band minima appears at the K-point for MoSTe, which lies between K-Γ points in WSTe. The HSE06 + SOC gaps

are found to be 1.98, 1.61, 1.64, 1.94, 1.70, and 1.51 eV for MoSSe, MoSTe, MoSeTe, WSSe, WSTe, and WSeTe, respectively.

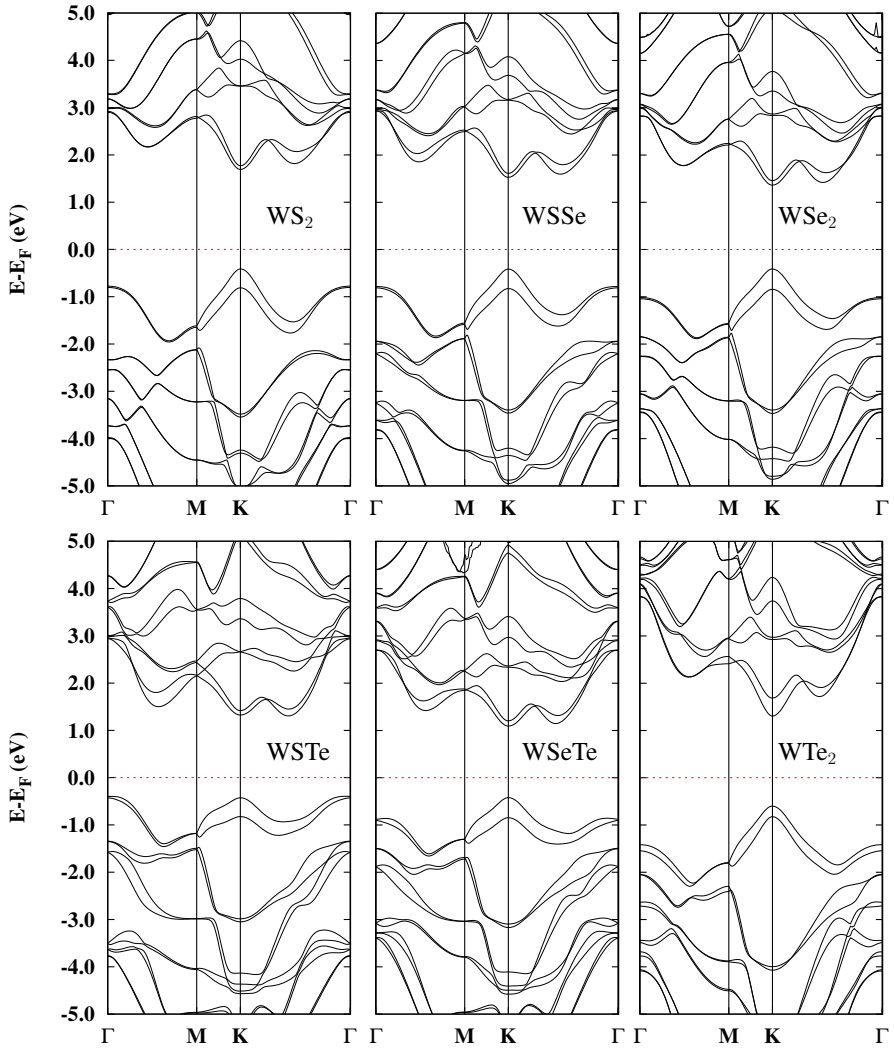

Figure 6.3: Band structures of WS_2, WSSe, WSe_2, WSTe, WSeTe, and WTe_2 which have direct band gap at K-point except WSTe. WSTe has indirect gap, where VBM lies at Γ and CBM lies between K-Γ.

Calculated results are in good agreement with the available photoluminescence (PL) spectrum that measures the optical gap for the direct gap semiconductors. Note that the calculated gap of MXY monolayer is about the average of their natural MX_2 and MY_2 layers. For example, the 1.98 eV gap of MoSSe lies in between MoS_2 (2.10 eV) and $MoSe_2$ (1.84 eV). The present results is in agreement with the

experimental photoluminescence peak of the MoSSe monolayer, which is located at 1.68 eV. [306, 307, 317] Thus, the PL spectrum redshifts (blueshifts) when the MoSSe is synthesized by selenizing (sulfurizing) the MoS_2 ($MoSe_2$) monolayer. However, one should take a note that the PL intensity in MoSSe is much lower then the natural MoX_2 counterparts.

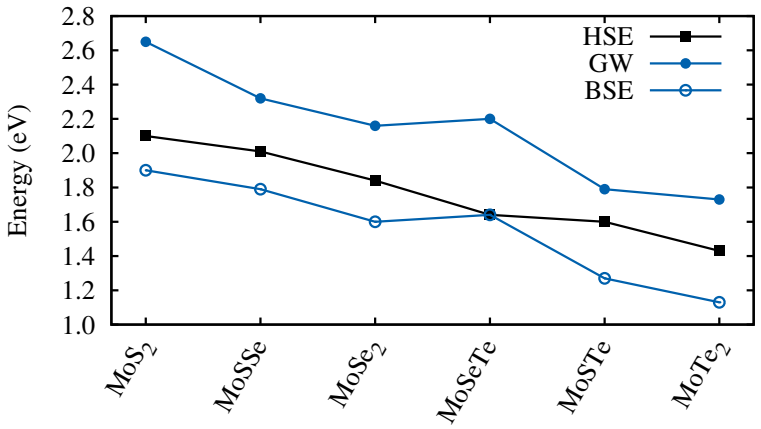

Figure 6.4: Calculated band gaps of the MoX_2 and MoXY monolayers. Results from different hierarchical theories, hybrid HSE06, *GW* and *GW*+ BSE, are compared.

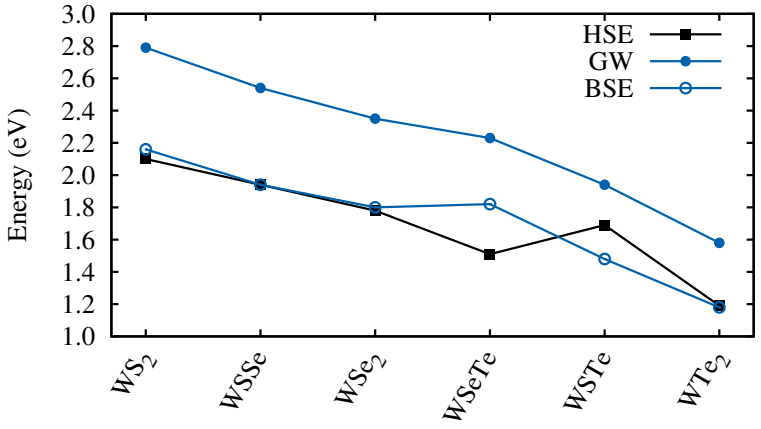

Figure 6.5: Calculated band gaps of the WX_2 and WXY monolayers. Results from different hierarchical theories, hybrid HSE06, *GW* and *GW*+ BSE, are compared.

Now we discuss the electronic structure within the various theoretical hierarchy (Figure 6.4 and Figure 6.5) in the context of available experimental results. It

is known that, conventional exchange-correlation functionals underestimate the band gap in semiconductors and insulators, and a hybrid functional improves the result. A fraction f of the exact Hartree-Fock exchange is considered in hybrid functional, while the correlation part remains entirely parameterized. In general, $f = 0.25$ is considered, the gap monotonically varies with f, leading to the uncertainty in the prediction. On the other hand, the many-body perturbation theory, where electron self-energy is expressed in terms of Green's function G and screened Coulomb interaction W, provides an excellent account of the quasiparticle (QP) gap E_g^{QP}, however, the method is computationally very expensive. The calculated QP gaps are experimentally measured with scanning tunneling spectroscopy (STS), and the theoretical values are reported in Table 6.2. Overall, we observe a good agreement between the GW calculation and STS measurements. We calculate a QP gap of 2.65 eV for monolayer MoS_2, which is in close proximity to the experimental data of 2.40 eV. [318, 319] It must be pointed here, that the QP gap value slightly depend on the nature of the substrate, and it is expected that the QP is slightly renormalized due to the substrate-monolayer interaction. It was found that the QP bandgap of $MoSe_2$ on hBN/Ru(0001) is about 0.25 eV smaller than those on graphene or graphite substrates. [320] The calculated gap of 2.16 eV for $MoSe_2$ is in excellent agreement with the experimental data of 1.90 - 2.15 eV, depending on the substrate. A similar comparison could be drawn for WX_2 monolayers, and the QP gap decreases in the S $\rightarrow$ Se $\rightarrow$ Te direction. The QP gaps for the single-layers of WX_2 calculated within the GW approach (Table 6.2) compare well with the experimental data. It was inferred that the gap in bare WS_2 decreases from 2.4 to 2.27 eV, while the monolayer is capped the bilayer graphene. [321] The QP gap in WSe_2 is lower at 2.35 eV, which compares well with the STS data, 2.18 $\pm$ 0.03 eV. [322]

Having discussed the QP gap, now we turn our attention to the optical gap,

which is renormalized by the exciton binding energy (Table 6.2), which is expected to be substantial due to poor electron screening in the 2D materials. The optical gap is experimentally measured by photoluminescence (PL) spectroscopy measurements, while the the optical gaps are theoretically calculated with the GW+BSE approach. The PL peak is observed at 1.88 eV for MoS_2 monolayer, and a weak temperature dependance of the peak position is also identified. [10, 323] Calculated result is in excellent agreement, $E_g^{\text{opt}} = 1.90$ eV for MoS_2. Likewise, the comparison between the theoretical and experimental results remain for the other monolayers. compared to MoS_2, the optical gap is much lower in single-layer $MoSe_2$, 1.60 eV, which is in excellent agreement with the position of the PL peak at 1.55 eV. [324] The trend is similar in WX_2 monolayers. The calculated E_g^{opt} for WS_2 and WSe_2 are in good agreement with he experimental values of 1.95 [325] and 1.65 eV [16], respectively.

It is now understood that since the electronic structure for the MX_2 monolayers are correctly reproduced within the $GW+$ BSE calculations - (a) it is expected to predict well for the Janus counterparts, and (b) the the exciton binding with in the same theoretical framework, which is defined as $E_{\text{x}} = E_g^{\text{QP}} - E_g^{\text{opt}}$, will also be practical. The optical gap for the MoSSe monolayer (1.79 eV) is about the average of MoS_2 and $MoSe_2$, which is in excellent agreement with the PL peak at 1.7 eV. [306, 307] The WSSe monolayer has been recently synthesised via pulsed laser deposition method, and the corresponding optical gap of 1.83 eV is in agreement with the present calculation (Table 6.2).

6.3.2 Photocatalytic activity of TMD and JTMD

To investigate the photocatalytic activity of TMDC and JTMDC monolayers, we study the band alignment with the water redox potentials. The alignments for the natural MX_2 monolayers are shown in Figure 6.6, and compare them with the redox potentials of hydrogen evolution (H^+/H_2) and oxygen evolution (O_2/H_2O) at pH= 0. We find that MoS_2, $MoSe_2$, and WS_2 have the band edges that straddle with the redox potentials and make them promising candidates for photocatalytic water splitting. However, $MoTe_2$, WSe_2, and WTe_2 are found to be favourable only to the water reduction reaction. The reduction over-potentials (χ_{H_2}) are 0.07, 0.48, 0.66, 0.46, 0.82, and 0.82 eV for MoS_2, $MoSe_2$, $MoTe_2$, WS_2, WSe_2, and WTe_2, respectively. While the oxidation over-potentials (χ_{O_2}) are 0.80, 0.13, and 0.41 eV for MoS_2, $MoSe_2$, and WS_2, respectively. Besides the favourable band positioning, exciton dissociation is also crucial for the photocatalytic process, which is relatively difficult in these natural monolayers, owing to their high exciton binding energy (Table 6.2).

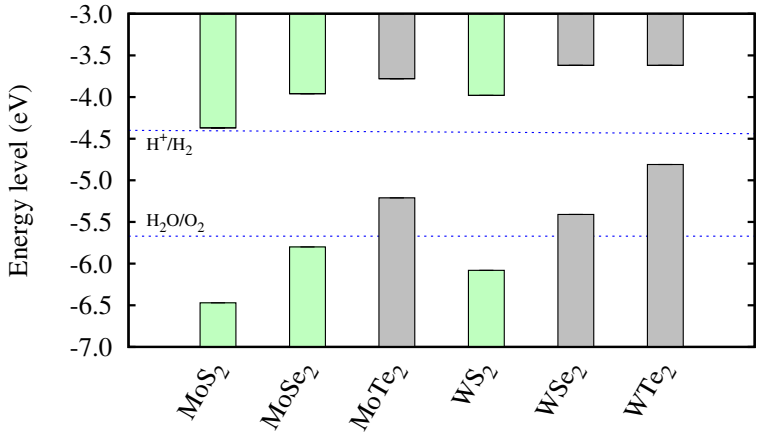

Figure 6.6: Band-edge positions of the natural MX_2 monolayers that are calculated within the hybrid HSE06 exchange-correlation functional, which are drawn along with the redox potentials.

In contrast, the Janus TMDCs have remarkable advantages over the natural

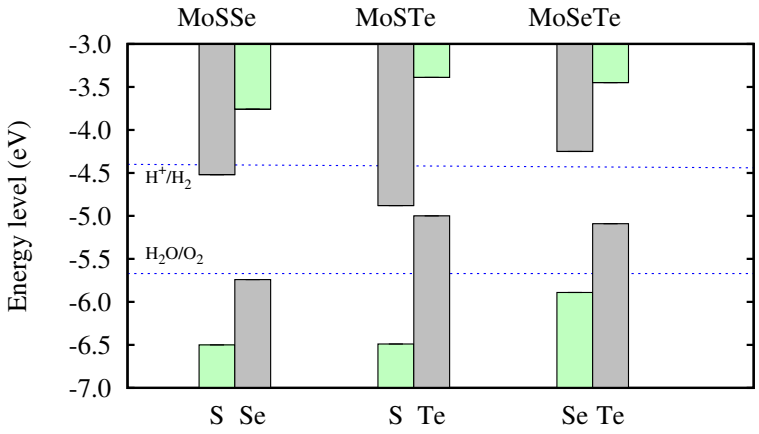

Figure 6.7: Band-edge positions of the Janus MoXY monolayers that are calculated within the hybrid HSE06 exchange-correlation functional, which are drawn along with the redox potentials.

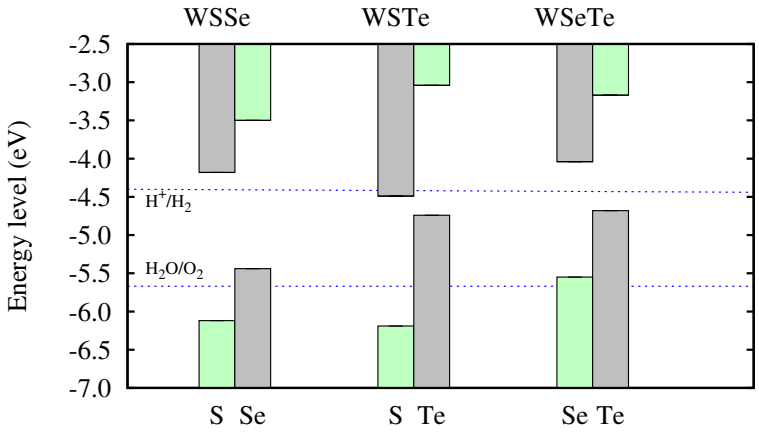

Figure 6.8: Band-edge positions of the Janus WXY monolayers that are calculated within the hybrid HSE06 exchange-correlation functional, which are drawn along with the redox potentials.

TMDCs due to the presence of an internal electric field. [309, 310] The band-edge energy alignments of VBM and CBM are calculated and shown in Figure 6.7 and Figure 6.8. The fundamental criteria of photocatalysis, band gap restriction (> 1.23) is broken, and the redox potential difference of the two chalcogen layers is equal to the electrostatic potential difference ($\Delta\Phi$). As the electrons and holes are separated on the two different layers, the efficiency of the catalyst can be en-

hanced. All JTMDCs are favorable for photocatalytic water splitting reactions as shown (Figure 6.7 and Figure 6.8). In the case of Janus MoSSe single-layer, the photogenerated electrons and holes accumulate on the Se, and S layer, respectively. Similarly, electrons accumulate on Te layer for MoSTe, and MoSeTe, while holes accumulate on S, and Se layer for MoSTe, and MoSeTe, respectively. These results are consistent with previous reported literature. [309] In the case of W based Janus TMDCs, the photogenerated electrons accumulate on the Se, Te, and Te layer for WSSe, WSTe, and WSeTe, respectively. Conversely, the photogenerated holes accumulate on S, S, and Se layer for WSSe, WSTe, and WSeTe, respectively. Apart from the proper band edge positions, exciton dissociation is also an important factor, that dictates the photocatalytic efficiency. A large internal electric field facilitate the easier exciton pairs dissociate. In Janus TMDCs, the corresponding exciton binding is renormalized due to the internal electric field, that makes easier dissociation and utilization of the photogenerated carriers (Table 6.2), and cause the free electron and hole to migrate in the opposite directions to facilitate the photocatalytic reaction with high efficiency.

6.3.3 Modeling exciton in TMDCs and JTMDCs

The photogenerated electron and hole pairs have the attractive Coulomb interaction, and this interaction in the quasiparticle is called an exciton, as we have discussed in earlier Chapters. Charge separation can happen easily as the exciton binding energy decreases and the separated charge carriers can participate in the corresponding redox reactions. We adopt two distinct ways to calculate the exciton binding energy E_x. One within the GW+BSE formalism, which correctly describe the quasiparticle and optical spectra. However, the the same is computationally very expensive. On the other hand, following Keldysh formalism [238] one can adopt a hydrogenic model of excitons, where the parameters are calculated from

the conventional DFT calculations, which are relatively much less expensive. The model has been described in an earlier Chapter in details, here we describe the main ingredients of the same for convenience.

The 2D electron-hole interaction is described within the Keldysh formalism [238], $V_{2D}(r) = -\frac{e^2}{4(\varepsilon_1+\varepsilon_2)\varepsilon_0 r_0}[H_0(\frac{r}{r_0}) + Y_0(\frac{r}{r_0})]$, where ε_1 and ε_2 are the dielectric constant of the surrounding media(vacuum); and ε_0 is the vacuum permittivity. [190, 201, 239] H_0 and Y_0 are Struve and Bessel functions, respectively. With this potential $V_{2D}(r)$, the hydrogenic Hamilltonian is developed, $H_x = -\frac{\hbar^2}{2\mu}\nabla_r^2 + V_{2D}(r)$, where μ is the exciton reduced mass, and r is the electron-hole separation. The screening length $r_0 = 2\pi\chi_{2D}$, where χ_{2D} is the 2D polarizability, which is calculated from the static dielectric constant ε of the 2D system, $\varepsilon(L_v) = 1 + 4\pi\chi_{2D}/L_v$, where L_v is the transverse vacuum size. [240] The effective carrier masses, which are the parameters of the model, are estimated by fitting the HSE06 bands to the parabolic dispersion $E(k) = \hbar^2k^2/2m^*$, and tabulated in Table 6.3. The static dielectric constant is calculated from the real part of the complex dielectric function at zero frequency. The variational exciton binding energy $E_x = E_K(a) + E_P(a)$ is then calculated for an optimal value to the exciton radius a, where E_K and E_P is kinetic and potential energies of the exciton. We find that the calculated E_x within this simple model are in excellent agreement with the GW+ BSE data (Table 6.2) that reestablishes a broader applicability of the hydrogenic model.

6.3.4 Optical properties

The frequency-dependent complex dielectric tensor $\varepsilon(\omega) = \varepsilon'(\omega) + i\varepsilon''(\omega)$ is used to evaluate the optical properties. The imaginary part $\varepsilon''(\omega)$ is calculated in the

Table 6.2: The quasiparticle E_g^{QP} and optical E_g^{opt} gaps are calculated within the G_2W_0 and G_2W_0 + BSE, respectively. The exciton binding energies E_{x} are calculated within the hydrogenic exciton model, which is in good agreement with the more accurate GW + BSE formalism. Model parameter, $\chi_{2\mathrm{D}}$ is calculated within the HSE06.

System	E_g^{QP}(eV)	E_g^{opt}(eV)	E_{x} (eV)		$\chi_{2\mathrm{D}}$(Å)
			BSE	model	
MoS_2	2.65	1.90	0.75	0.66	5.41
MoSSe	2.32	1.79	0.53	0.58	5.98
$MoSe_2$	2.16	1.60	0.56	0.55	6.55
MoSTe	1.79	1.27	0.52	0.57	7.47
MoSeTe	2.20	1.64	0.56	0.51	7.79
$MoTe_2$	1.73	1.13	0.60	0.44	8.77
WS_2	2.79	2.16	0.63	0.63	4.91
WSSe	2.54	1.94	0.60	0.61	5.45
WSe_2	2.35	1.80	0.55	0.58	5.93
WSTe	1.94	1.48	0.46	0.59	6.84
WSeTe	2.23	1.82	0.41	0.51	7.21
WTe_2	1.58	1.18	0.40	0.41	8.37

Table 6.3: The effective carrier masses m_e^* and m_h^*, and the average static dielectric constant (ε) are calculated within the HSE06 hybrid functional. The corresponding exciton extension, a, is calculated within the hydrogenic model.

System	m_e^*/m_e	m_h^*/m_e	ε	a (Å)
MoS_2	0.54	0.69	3.53	8.42
MoSSe	0.47	0.55	3.81	9.54
$MoSe_2$	0.44	0.48	4.05	9.94
MoSTe	0.65	1.30	4.53	8.04
MoSeTe	0.71	0.62	4.69	9.25
$MoTe_2$	0.47	0.58	5.18	11.30
WS_2	0.41	0.40	3.30	9.75
WSSe	0.45	0.47	3.56	9.60
WSe_2	0.48	0.49	3.80	9.68
WSTe	0.53	1.64	4.23	8.00
WSeTe	0.53	0.51	4.42	10.06
WTe_2	0.36	0.37	4.99	12.54

long-wavelength $\mathbf{q} \to \mathbf{0}$ limit, [188]

$$\begin{aligned} \varepsilon''_{\alpha\beta}(\omega) &= \frac{4\pi^2 e^2}{\Omega} \lim_{q\to 0} \frac{1}{q^2} \sum_{c,v,\mathbf{k}} 2w_{\mathbf{k}} \delta(\epsilon_{c\mathbf{k}} - \epsilon_{v\mathbf{k}} - \omega) \\ &\times \langle u_{c\mathbf{k}+\mathbf{e}_\alpha q} | u_{v\mathbf{k}} \rangle \langle u_{c\mathbf{k}+\mathbf{e}_\beta q} | u_{v\mathbf{k}} \rangle^*. \end{aligned} \tag{6.1}$$

Here, the factor 2 inside the summation accounts for the spin degeneracy, Ω is the volume of the primitive cell, and $\omega_{\mathbf{k}}$ are k-point weights. The $\epsilon_{c\mathbf{k}}$ ($\epsilon_{v\mathbf{k}}$) are $\mathbf{k}$-dependent conduction (valence) band energies, $u_{c\mathbf{k},v\mathbf{k}}$ are cell periodic part of the pseudo-wave-function, and $\mathbf{e}_{\alpha,\beta}$ are unit vectors along the Cartesian directions. The real part $\varepsilon'(\omega)$ of the frequency dependent complex dielectric tensor $\varepsilon(\omega)$ is evaluated using the Kramers-Kronig transformation, and the absorption co-efficient is calculated as $\Lambda_{\alpha\alpha}(\omega) = \frac{2\omega}{c}[|\varepsilon_{\alpha\alpha}(\omega)| - \varepsilon'_{\alpha\alpha}(\omega)]^{\frac{1}{2}}$. The optical absorption co-efficients are calculated for the TMDCs, and JTMDCs using *GW* and *GW*+BSE formalism (Figure 6.9), that is, without and with the electron-hole interaction. We observe that both TMDCs and JTMDCs show strong photoabsorption in the visible region, which is an important criterion for good photocatalyst.

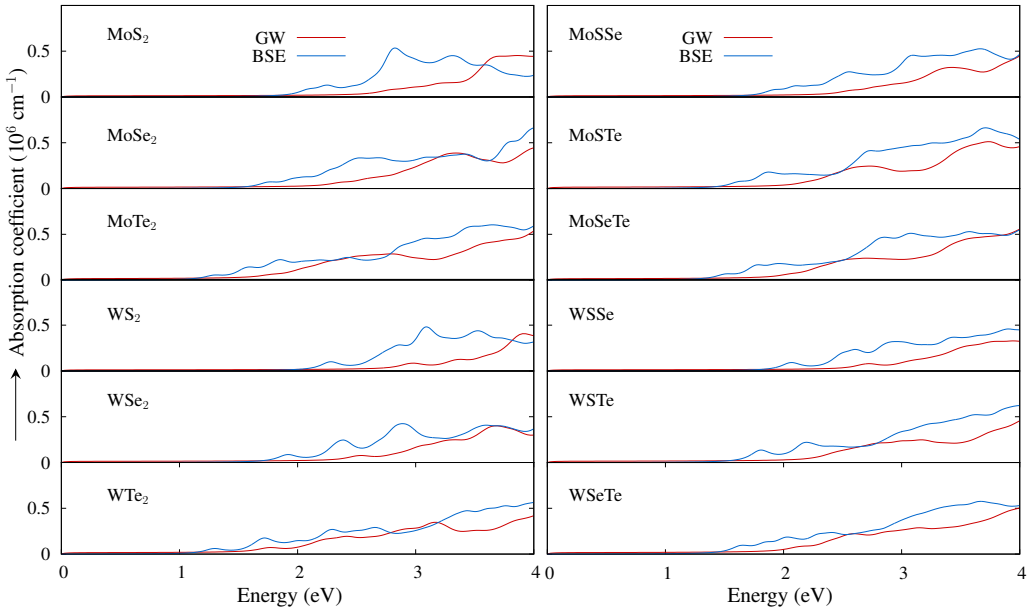

Figure 6.9: Absorption coefficient for the natural TMDCs and JTMDCs are calculated without and with the electron-hole interaction using *GW* + BSE formalism. The left (right) panel refers to the TMDCs (JTMDCs). Excitonic contributions are significant for all monolayers.

6.4 Conclusion

In this Chapter, we illustrate two conclusions. First, the Janus TMDCs are promising candidate materials as photocatalyst and may have better quantum efficiencies than the natural TMDCs. This fact is demonstrated via their superior band alignment with the redox potentials, high optical absorption and low exciton binding promoting easy dissociation and concurrent utilization of photogenerated carriers. The presence of the internal electric field due to the difference in Pauling electronegativity on both sides is responsible for this prediction. The second point is rather theoretical. With a comprehensive comparison with the *GW*+ BSE results, we demonstrate that the hydrogenic model with parameters calculated from the conventional DFT calculation provides an excellent account of exciton binding

these materials and general application to other 2D semiconductors.

CHAPTER 7

SUMMARY AND FUTURE OUTLOOK

Owing to large specific surface area and excellent charge transfer performance electronic properties, a variety of two-dimensional materials have been successfully investigated for photocatalysis. In this thesis, we theoretically studied the optical and excitonic properties of a few important 2D materials such as phosphorene, graphene nitride and transition-metal dichalcogenides along with their heterostructures.

In the context of metal-free 2D photocatalyst, we propose that chemical derivatives of phosphorene have an outstanding potential. Here, we utilize the chemical instability of phosphorene in ambient condition, which readily react with O, S, and N due to the presence of lone-pair electrons. While, the 2D phosphorene does not catalyze the complete water splitting reactions, under O, S, and N coverages the derivatives become susceptible to trigger the complete reaction at certain coverages. The derivative are thermodynamically stable and these dopants do not introduce the midgap defect states, and at particular coverages the conduction and valence bands are properly aligned. Additionally, the optical absorption remain very high 10^5 cm^2 within the visible light excitation. The present results along with their excitonic properties will hopefully open up new avenues to take advantage of phosphorene derivatives in metal-free photocatalysis.

The van der Waals heterostructures pose enormous tunability of the photocatalytic properties, which should attract tremendous attention. In this context, we combined two interesting 2D materials – Janus transition-metal dichalcogenides (MoXY, X/Y = S, Se, Te) and graphitic carbon nitride. Due to the internal electric

field, the photogenerated electrons and holes are easily separated in the MoXY layers, which also creates high overpotentials for the redox reactions. The high optical absorptions span throughout the entire visible and near ultraviolet regime in these nanocomposites. Combining the these results along with comparatively smaller exciton binding, we propose that the studied heterostructure may be good candidate materials for photocatalysis. Further, we hope such vertical 2D heterostructures will attract increased attention experimentally.

An important aspect of studying photocatalytic properties of the 2D materials is to investigate excitons, and a quantitative prediction of binding energy in photogenerated electron-hole pairs. The exciton binding indicates how easily or difficult is to separate the photogenerated electron-hole pairs, that in turn, affect the efficiency. The excitonic properties in the reduced dimensions are markedly different from the materials in three-dimension due to the fundamental difference in electron screening. However, a first-principles description is tremendously expensive, which necessitates an alternate approach to be developed without a compromise in accuracy. In this context, we describe a hydrogenic effective exciton mass model in which the parameters, the effective carrier masses and the static dielectric constant, are calculated within the conventional density functional theory (DFT). The results within this simplified model are in excellent agreement with those calculated within the *GW*-BSE formalism. Using this model, we investigated how excitons are affected in phosphorene derivatives and exciton renormalization in the few-layer and heterostructure phosphorene. We also extend this approach to investigate exciton in pristine and Janus transition metal dichalcogenides. In principle, the present methodology is applicable to any 2D semiconductors.

We believe that these 2D materials and specially the van der Waals 2D heterostructures will play a crucial role in designing new and efficient photocatalysts and attract further experimental attention.

BIBLIOGRAPHY

[1] Kostya S Novoselov, Andre K Geim, Sergei V Morozov, D Jiang, Y_ Zhang, Sergey V Dubonos, Irina V Grigorieva, and Alexandr A Firsov. Electric field effect in atomically thin carbon films. *Science*, 306:666–669, 2004.

[2] Hideyuki Nakano, Takuya Mitsuoka, Masashi Harada, Kayo Horibuchi, Hiroshi Nozaki, Naoko Takahashi, Takamasa Nonaka, Yoshiki Seno, and Hiroshi Nakamura. Soft synthesis of single-crystal silicon monolayer sheets. *Angew. Chem. Int. Ed.*, 45:6303–6306, 2006.

[3] Linfei Li, Shuang-zan Lu, Jinbo Pan, Zhihui Qin, Yu-qi Wang, Yeliang Wang, Geng-yu Cao, Shixuan Du, and Hong-Jun Gao. Buckled germanene formation on pt (111). *Adv. Mater.*, 26:4820–4824, 2014.

[4] D Pacile, JC Meyer, ÇÖ Girit, and AJAPL Zettl. The two-dimensional phase of boron nitride: Few-atomic-layer sheets and suspended membranes. *Appl. Phys. Lett.*, 92:133107, 2008.

[5] Guoxing Li, Yuliang Li, Xuemin Qian, Huibiao Liu, Haowei Lin, Nan Chen, and Yongjun Li. Construction of tubular molecule aggregations of graphdiyne for highly efficient field emission. *J. Phys. Chem. C*, 115:2611–2615, 2011.

[6] Dattatray J Late. Temperature dependent phonon shifts in few-layer black phosphorus. *ACS Appl. Mater. Interfaces*, 7:5857–5862, 2015.

[7] Xianfen Wang, Satoshi Kajiyama, Hiroki Iinuma, Eiji Hosono, Shinji Oro, Isamu Moriguchi, Masashi Okubo, and Atsuo Yamada. Pseudocapacitance

of mxene nanosheets for high-power sodium-ion hybrid capacitors. *Nat. Commun.*, 6:1–6, 2015.

[8] Qing Hua Wang, Kourosh Kalantar-Zadeh, Andras Kis, Jonathan N Coleman, and Michael S Strano. Electronics and optoelectronics of two-dimensional transition metal dichalcogenides. *Nat. Nanotechnol.*, 7:699–712, 2012.

[9] Kin Fai Mak and Jie Shan. Photonics and optoelectronics of 2d semiconductor transition metal dichalcogenides. *Nat. Photon.*, 10:216, 2016.

[10] Kin Fai Mak, Changgu Lee, James Hone, Jie Shan, and Tony F Heinz. Atomically thin mos 2: a new direct-gap semiconductor. *Phys. Rev. Lett.*, 105:136805, 2010.

[11] Tawinan Cheiwchanchamnangij and Walter RL Lambrecht. Quasiparticle band structure calculation of monolayer, bilayer, and bulk mos 2. *Phys. Rev. B*, 85:205302, 2012.

[12] Kin Fai Mak, Keliang He, Jie Shan, and Tony F Heinz. Control of valley polarization in monolayer mos 2 by optical helicity. *Nat. Nanotechnol.*, 7:494–498, 2012.

[13] Hualing Zeng, Junfeng Dai, Wang Yao, Di Xiao, and Xiaodong Cui. Valley polarization in mos_2 monolayers by optical pumping. *Nat. Nanotechnol.*, 7:490–493, 2012.

[14] Edbert J. Sie, James W. McIver, Yi-Hsien Lee, Liang Fu, Jing Kong, and Nuh Gedik. Valley-selective optical stark effect in monolayer ws_2. *Nat. Mater.*, 14:290–294, 2015.

[15] Liam Britnell, RM Ribeiro, A Eckmann, R Jalil, BD Belle, A Mishchenko, Y-J Kim, RV Gorbachev, T Georgiou, SV Morozov, et al. Strong light-matter interactions in heterostructures of atomically thin films. *Science*, 340:1311–1314, 2013.

[16] Hui Fang, Corsin Battaglia, Carlo Carraro, Slavomir Nemsak, Burak Ozdol, Jeong Seuk Kang, Hans A Bechtel, Sujay B Desai, Florian Kronast, Ahmet A Unal, et al. Strong interlayer coupling in van der waals heterostructures built from single-layer chalcogenides. *Proc. Natl. Acad. Sci. U.S.A.*, 111:6198–6202, 2014.

[17] Xiaoze Liu, Tal Galfsky, Zheng Sun, Fengnian Xia, Erh-chen Lin, Yi-Hsien Lee, Stéphane Kéna-Cohen, and Vinod M Menon. Strong light–matter coupling in two-dimensional atomic crystals. *Nat. Photon.*, 9:30, 2015.

[18] Ashwin Ramasubramaniam. Large excitonic effects in monolayers of molybdenum and tungsten dichalcogenides. *Phys. Rev. B*, 86:115409, 2012.

[19] Hannu-Pekka Komsa and Arkady V Krasheninnikov. Effects of confinement and environment on the electronic structure and exciton binding energy of mos 2 from first principles. *Phys. Rev. B*, 86:241201, 2012.

[20] Miguel M Ugeda, Aaron J Bradley, Su-Fei Shi, H Felipe, Yi Zhang, Diana Y Qiu, Wei Ruan, Sung-Kwan Mo, Zahid Hussain, Zhi-Xun Shen, et al. Giant bandgap renormalization and excitonic effects in a monolayer transition metal dichalcogenide semiconductor. *Nat. Mater.*, 13:1091–1095, 2014.

[21] Alexey Chernikov, Timothy C Berkelbach, Heather M Hill, Albert Rigosi, Yilei Li, Ozgur Burak Aslan, David R Reichman, Mark S Hybertsen, and Tony F Heinz. Exciton binding energy and nonhydrogenic rydberg series in monolayer ws 2. *Phys. Rev. Lett.*, 113:076802, 2014.

[22] Keliang He, Charles Poole, Kin Fai Mak, and Jie Shan. Experimental demonstration of continuous electronic structure tuning via strain in atomically thin mos2. *Nano Lett.*, 13:2931–2936, 2013.

[23] Andres Castellanos-Gomez, Rafael Roldán, Emmanuele Cappelluti, Michele Buscema, Francisco Guinea, Herre SJ van der Zant, and Gary A Steele. Local strain engineering in atomically thin mos2. *Nano Lett.*, 13:5361–5366, 2013.

[24] Ashwin Ramasubramaniam, Doron Naveh, and Elias Towe. Tunable band gaps in bilayer transition-metal dichalcogenides. *Phys. Rev. B*, 84:205325, 2011.

[25] Karel-Alexander N Duerloo, Yao Li, and Evan J Reed. Structural phase transitions in two-dimensional mo-and w-dichalcogenide monolayers. *Nat. Commun.*, 5:1–9, 2014.

[26] Fengnian Xia, Han Wang, Di Xiao, Madan Dubey, and Ashwin Ramasubramaniam. Two-dimensional material nanophotonics. *Nat. Photon.*, 8:899, 2014.

[27] Diana Y Qiu, H Felipe, and Steven G Louie. Optical spectrum of mos 2: many-body effects and diversity of exciton states. *Phys. Rev. Lett.*, 111:216805, 2013.

[28] Marco Bernardi, Maurizia Palummo, and Jeffrey C Grossman. Extraordinary sunlight absorption and one nanometer thick photovoltaics using two-dimensional monolayer materials. *Nano Lett.*, 13:3664–3670, 2013.

[29] Giuseppe Franco Bassani and Giuseppe Pastori Parravicini. *Electronic states and optical transitions in solids*, volume 8. Pergamon, 1975.

[30] Marco Bernardi, Can Ataca, Maurizia Palummo, and Jeffrey C Grossman. Optical and electronic properties of two-dimensional layered materials. *Nanophotonics*, 6:479–493, 2017.

[31] Xi Ling, Han Wang, Shengxi Huang, Fengnian Xia, and Mildred S Dresselhaus. The renaissance of black phosphorus. *Proc. Natl. Acad. Sci. U.S.A.*, 112:4523–4530, 2015.

[32] Vy Tran, Ryan Soklaski, Yufeng Liang, and Li Yang. Layer-controlled band gap and anisotropic excitons in few-layer black phosphorus. *Phys. Rev. B*, 89:235319, 2014.

[33] Fengnian Xia, Han Wang, and Yichen Jia. Rediscovering black phosphorus as an anisotropic layered material for optoelectronics and electronics. *Nat. Commun.*, 5:1–6, 2014.

[34] Jingsi Qiao, Xianghua Kong, Zhi-Xin Hu, Feng Yang, and Wei Ji. High-mobility transport anisotropy and linear dichroism in few-layer black phosphorus. *Nat. Commun.*, 5:1–7, 2014.

[35] Xiaomu Wang, Aaron M Jones, Kyle L Seyler, Vy Tran, Yichen Jia, Huan Zhao, Han Wang, Li Yang, Xiaodong Xu, and Fengnian Xia. Highly anisotropic and robust excitons in monolayer black phosphorus. *Nat. Nanotechnol.*, 10:517, 2015.

[36] Guowei Zhang, Andrey Chaves, Shenyang Huang, Fanjie Wang, Qiaoxia Xing, Tony Low, and Hugen Yan. Determination of layer-dependent exciton binding energies in few-layer black phosphorus. *Sci. Adv.*, 4:eaap9977, 2018.

[37] Mingsheng Xu, Tao Liang, Minmin Shi, and Hongzheng Chen. Graphene-like two-dimensional materials. *Chem. Rev.*, 113:3766–3798, 2013.

[38] Cory R Dean, Andrea F Young, Inanc Meric, Chris Lee, Lei Wang, Sebastian Sorgenfrei, Kenji Watanabe, Takashi Taniguchi, Phillip Kim, Kenneth L Shepard, et al. Boron nitride substrates for high-quality graphene electronics. *Nat. Nanotechnol.*, 5:722–726, 2010.

[39] Gwan-Hyoung Lee, Young-Jun Yu, Xu Cui, Nicholas Petrone, Chul-Ho Lee, Min Sup Choi, Dae-Yeong Lee, Changgu Lee, Won Jong Yoo, Kenji Watanabe, et al. Flexible and transparent mos2 field-effect transistors on hexagonal boron nitride-graphene heterostructures. *ACS Nano.*, 7:7931–7936, 2013.

[40] Xu Cui, Gwan-Hyoung Lee, Young Duck Kim, Ghidewon Arefe, Pinshane Y Huang, Chul-Ho Lee, Daniel A Chenet, Xian Zhang, Lei Wang, Fan Ye, et al. Multi-terminal transport measurements of mos 2 using a van der waals heterostructure device platform. *Nat. Nanotechnol.*, 10:534, 2015.

[41] Xiaobo Chen, Shaohua Shen, Liejin Guo, and Samuel S Mao. Semiconductor-based photocatalytic hydrogen generation. *Chem. Rev.*, 110:6503–6570, 2010.

[42] Mohammad Ziaur Rahman, Kenneth Davey, and Shi-Zhang Qiao. Carbon, nitrogen and phosphorus containing metal-free photocatalysts for hydrogen production: progress and challenges. *J. Mater. Chem. A*, 6:1305–1322, 2018.

[43] Michael G Walter, Emily L Warren, James R McKone, Shannon W Boettcher, Qixi Mi, Elizabeth A Santori, and Nathan S Lewis. Solar water splitting cells. *Chem. Rev.*, 110:6446–6473, 2010.

[44] Mohammad Ziaur Rahman, Chi Wai Kwong, Kenneth Davey, and Shi Zhang Qiao. 2d phosphorene as a water splitting photocatalyst: fundamentals to applications. *Energy Environ. Sci.*, 9:709–728, 2016.

[45] Shanshan Chen, Tsuyoshi Takata, and Kazunari Domen. Particulate photocatalysts for overall water splitting. *Nat. Rev. Mater.*, 2:17050, 2017.

[46] Takashi Hisatomi, Kazuhiro Takanabe, and Kazunari Domen. Photocatalytic water-splitting reaction from catalytic and kinetic perspectives. *Catal. Lett.*, 145:95–108, 2015.

[47] Jean Francois Reber and Kurt Meier. Photochemical production of hydrogen with zinc sulfide suspensions. *J. Phys. Chem.*, 88:5903–5913, 1984.

[48] T Ohmori, H Mametsuka, and E Suzuki. Photocatalytic hydrogen evolution on inp suspension with inorganic sacrificial reducing agent. *Int. J. Hydrog. Energy*, 25:953–955, 2000.

[49] Meng Ni, Michael KH Leung, Dennis YC Leung, and K Sumathy. A review and recent developments in photocatalytic water-splitting using tio2 for hydrogen production. *Renew. Sustain. Energy Rev.*, 11:401–425, 2007.

[50] Michael R St. John, Alan J Furgala, and Anthony F Sammells. Hydrogen generation by photocatalytic oxidation of glucose by platinized n-titania powder. *J. Phys. Chem.*, 87:801–805, 1983.

[51] Gratian R Bamwenda, Susumu Tsubota, Toshiko Nakamura, and Masatake Haruta. Photoassisted hydrogen production from a water-ethanol solution: a comparison of activities of au-tio2 and pt-tio2. *J. Photochem. Photobiol., A*, 89:177–189, 1995.

[52] S Sakthivel, MV Shankar, M Palanichamy, Banumathi Arabindoo, DW Bahnemann, and V Murugesan. Enhancement of photocatalytic activity by metal deposition: characterisation and photonic efficiency of pt, au and pd deposited on tio2 catalyst. *Water Research*, 38:3001–3008, 2004.

[53] SX Liu, ZP Qu, XW Han, and CL Sun. A mechanism for enhanced photocatalytic activity of silver-loaded titanium dioxide. *Catal. Today*, 93:877–884, 2004.

[54] Nae-Lih Wu and Min-Shuei Lee. Enhanced tio2 photocatalysis by cu in hydrogen production from aqueous methanol solution. *Int. J. Hydrog. Energy*, 29:1601–1605, 2004.

[55] A. Tanaka, K. Teramura, S. Hosokawa, H. Kominami, and T. Tanaka. Visible light-induced water splitting in an aqueous suspension of a plasmonic au/tio2 photocatalyst with metal co-catalysts. *Chem. Sci.*, 8:2574–2580, 2017.

[56] Xiukai Li, Naoki Kikugawa, and Jinhua Ye. Nitrogen-doped lamellar niobic acid with visible light-responsive photocatalytic activity. *Adv. Mater.*, 20:3816–3819, 2008.

[57] Qin Li, Huan Meng, Peng Zhou, Yingqiu Zheng, Juan Wang, Jiaguo Yu, and JianRu Gong. Zn1–x cd x s solid solutions with controlled bandgap and enhanced visible-light photocatalytic h2-production activity. *Acs Catal.*, 3:882–889, 2013.

[58] Fan Zuo, Le Wang, Tao Wu, Zhenyu Zhang, Dan Borchardt, and Pingyun Feng. Self-doped ti3+ enhanced photocatalyst for hydrogen production under visible light. *J. Am. Chem. Soc.*, 132:11856–11857, 2010.

[59] Yongfu Sun, Zhihu Sun, Shan Gao, Hao Cheng, Qinghua Liu, Junyu Piao, Tao Yao, Changzheng Wu, Shuanglin Hu, Shiqiang Wei, et al. Fabrication of flexible and freestanding zinc chalcogenide single layers. *Nat. Commun.*, 3:1057, 2012.

[60] Damien Voiry, Hisato Yamaguchi, Junwen Li, Rafael Silva, Diego CB Alves, Takeshi Fujita, Mingwei Chen, Tewodros Asefa, Vivek B Shenoy, Goki Eda, et al. Enhanced catalytic activity in strained chemically exfoliated ws 2 nanosheets for hydrogen evolution. *Nat. Mater.*, 12:850, 2013.

[61] Arunima K Singh, Kiran Mathew, Houlong L Zhuang, and Richard G Hennig. Computational screening of 2d materials for photocatalysis. *J. Phys. Chem. Lett.*, 6:1087–1098, 2015.

[62] Guohui Dong, Kun Zhao, and Lizhi Zhang. Carbon self-doping induced high electronic conductivity and photoreactivity of gc 3 n 4. *Chem. Commun.*, 48:6178–6180, 2012.

[63] Xinchen Wang, Kazuhiko Maeda, Arne Thomas, Kazuhiro Takanabe, Gang Xin, Johan M Carlsson, Kazunari Domen, and Markus Antonietti. A metal-free polymeric photocatalyst for hydrogen production from water under visible light. *Nat. Mater.*, 8:76, 2009.

[64] Tongming Su, Qian Shao, Zuzeng Qin, Zhanhu Guo, and Zili Wu. Role of interfaces in two-dimensional photocatalyst for water splitting. *Acs Catal.*, 8:2253–2276, 2018.

[65] Yu-Peng Yuan, Li-Sha Yin, Shao-Wen Cao, Li-Na Gu, Geng-Sheng Xu, Pingwu Du, Hua Chai, Yu-Sen Liao, and Can Xue. Microwave-assisted heating synthesis: a general and rapid strategy for large-scale production of highly crystalline gc 3 n 4 with enhanced photocatalytic h 2 production. *Green Chem.*, 16:4663–4668, 2014.

[66] Chunmei Li, You Xu, Wenguang Tu, Gang Chen, and Rong Xu. Metal-free photocatalysts for various applications in energy conversion and environmental purification. *Green Chem.*, 19:882–899, 2017.

[67] Xinchen Wang, Siegfried Blechert, and Markus Antonietti. Polymeric graphitic carbon nitride for heterogeneous photocatalysis. *Acs Catal.*, 2:1596–1606, 2012.

[68] David James Martin, Philip James Thomas Reardon, Savio JA Moniz, and Junwang Tang. Visible light-driven pure water splitting by a nature-inspired organic semiconductor-based system. *J. Am. Chem. Soc.*, 136:12568–12571, 2014.

[69] Shaowen Cao and Jiaguo Yu. g-c3n4-based photocatalysts for hydrogen generation. *J. Phys. Chem. Lett.*, 5:2101–2107, 2014.

[70] You Xu, Markus Kraft, and Rong Xu. Metal-free carbonaceous electrocatalysts and photocatalysts for water splitting. *Chem. Soc. Rev.*, 45:3039–3052, 2016.

[71] Jianghua Li, Biao Shen, Zhenhua Hong, Bizhou Lin, Bifen Gao, and Yilin Chen. A facile approach to synthesize novel oxygen-doped g-c 3 n 4 with superior visible-light photoreactivity. *Chem. Commun.*, 48:12017–12019, 2012.

[72] Yong Wang, Jinshui Zhang, Xinchen Wang, Markus Antonietti, and Haoran Li. Boron-and fluorine-containing mesoporous carbon nitride polymers: metal-free catalysts for cyclohexane oxidation. *Angew. Chem. Int. Ed.*, 49(19):3356–3359, 2010.

[73] Yuanjian Zhang, Toshiyuki Mori, Jinhua Ye, and Markus Antonietti. Phosphorus-doped carbon nitride solid: enhanced electrical conductivity and photocurrent generation. *J. Am. Chem. Soc.*, 132:6294–6295, 2010.

[74] Gang Liu, Ping Niu, Chenghua Sun, Sean C Smith, Zhigang Chen, Gao Qing Lu, and Hui-Ming Cheng. Unique electronic structure induced high photoreactivity of sulfur-doped graphitic c3n4. *J. Am. Chem. Soc.*, 132:11642–11648, 2010.

[75] Chen Ye, Jia-Xin Li, Zhi-Jun Li, Xu-Bing Li, Xiang-Bing Fan, Li-Ping Zhang, Bin Chen, Chen-Ho Tung, and Li-Zhu Wu. Enhanced driving force and

charge separation efficiency of protonated g-c3n4 for photocatalytic o2 evolution. *Acs Catal.*, 5:6973–6979, 2015.

[76] Xiaobo Li, Gareth Hartley, Antony J Ward, Pamela A Young, Anthony F Masters, and Thomas Maschmeyer. Hydrogenated defects in graphitic carbon nitride nanosheets for improved photocatalytic hydrogen evolution. *J. Phys. Chem. C*, 119:14938–14946, 2015.

[77] Jianhua Sun, Jinshui Zhang, Mingwen Zhang, Markus Antonietti, Xianzhi Fu, and Xinchen Wang. Bioinspired hollow semiconductor nanospheres as photosynthetic nanoparticles. *Nat. Commun.*, 3:1139, 2012.

[78] Katharina Schwinghammer, Maria B Mesch, Viola Duppel, Christian Ziegler, Jurgen Senker, and Bettina V Lotsch. Crystalline carbon nitride nanosheets for improved visible-light hydrogen evolution. *J. Am. Chem. Soc.*, 136:1730–1733, 2014.

[79] Yun Zheng, Lihua Lin, Xiangju Ye, Fangsong Guo, and Xinchen Wang. Helical graphitic carbon nitrides with photocatalytic and optical activities. *Angew. Chem. Int. Ed.*, 53(44):11926–11930, 2014.

[80] Shubin Yang, Yongji Gong, Jinshui Zhang, Liang Zhan, Lulu Ma, Zheyu Fang, Robert Vajtai, Xinchen Wang, and Pulickel M Ajayan. Exfoliated graphitic carbon nitride nanosheets as efficient catalysts for hydrogen evolution under visible light. *Adv. Mater.*, 25:2452–2456, 2013.

[81] Manish Chhowalla, Hyeon Suk Shin, Goki Eda, Lain-Jong Li, Kian Ping Loh, and Hua Zhang. The chemistry of two-dimensional layered transition metal dichalcogenide nanosheets. *Nat. Chem.*, 5:263, 2013.

[82] Xiao Huang, Zhiyuan Zeng, and Hua Zhang. Metal dichalcogenide

nanosheets: preparation, properties and applications. *Chem. Soc. Rev.*, 42:1934–1946, 2013.

[83] Rajesh Kappera, Damien Voiry, Sibel Ebru Yalcin, Brittany Branch, Gautam Gupta, Aditya D Mohite, and Manish Chhowalla. Phase-engineered low-resistance contacts for ultrathin mos 2 transistors. *Nat. Mater.*, 13:1128, 2014.

[84] Kai Xu, Fengmei Wang, Zhenxing Wang, Xueying Zhan, Qisheng Wang, Zhongzhou Cheng, Muhammad Safdar, and Jun He. Component-controllable ws2 (1–x) se2 x nanotubes for efficient hydrogen evolution reaction. *Acs Nano*, 8:8468–8476, 2014.

[85] CK Sumesh and Sebastian C Peter. Two-dimensional semiconductor transition metal based chalcogenide based heterostructures for water splitting applications. *Dalton Trans.*, 48:12772–12802, 2019.

[86] H Tributsch and JC Bennett. Electrochemistry and photochemistry of mos2 layer crystals. i. *J. Electroanal. Chem. Interf. Electrochem.*, 81:97–111, 1977.

[87] Yang Yang, Huilong Fei, Gedeng Ruan, Yilun Li, and James M Tour. Vertically aligned ws2 nanosheets for water splitting. *Adv. Funct. Mater.*, 25:6199–6204, 2015.

[88] Zhihao Yu, Zhun-Yong Ong, Songlin Li, Jian-Bin Xu, Gang Zhang, Yong-Wei Zhang, Yi Shi, and Xinran Wang. Analyzing the carrier mobility in transition-metal dichalcogenide mos2 field-effect transistors. *Adv. Funct. Mater.*, 27:1604093, 2017.

[89] Haining Wang, Changjian Zhang, and Farhan Rana. Surface recombination limited lifetimes of photoexcited carriers in few-layer transition metal dichalcogenide mos2. *Nano Lett.*, 15:8204–8210, 2015.

[90] Yu-Peng Yuan, Shao-Wen Cao, Li-Sha Yin, Lin Xu, and Can Xue. Nis2 co-catalyst decoration on cdla2s4 nanocrystals for efficient photocatalytic hydrogen generation under visible light irradiation. *nt. J. Hydrog. Energy*, 38:7218–7223, 2013.

[91] Yidong Hou, Anders B Laursen, Jinshui Zhang, Guigang Zhang, Yongsheng Zhu, Xinchen Wang, Søren Dahl, and Ib Chorkendorff. Layered nanojunctions for hydrogen-evolution catalysis. *Angew. Chem. Int. Ed.*, 52:3621–3625, 2013.

[92] Xu Zong, Jingfeng Han, Guijun Ma, Hongjian Yan, Guopeng Wu, and Can Li. Photocatalytic h2 evolution on cds loaded with ws2 as cocatalyst under visible light irradiation. *J. Phys. Chem. C*, 115:12202–12208, 2011.

[93] Houlong L Zhuang and Richard G Hennig. Computational search for single-layer transition-metal dichalcogenide photocatalysts. *J. Phys. Chem. C*, 117:20440–20445, 2013.

[94] Si Zhou, Nanshu Liu, and Jijun Zhao. Phosphorus quantum dots as visible-light photocatalyst for water splitting. *Comput. Mater. Sci.*, 130:56–63, 2017.

[95] A Morita. Semiconducting black phosphorus. *Appl. Phys. A*, 39:227–242, 1986.

[96] Yan Li, Shengxue Yang, and Jingbo Li. Modulation of the electronic properties of ultrathin black phosphorus by strain and electrical field. *J. Phys. Chem. C*, 118:23970–23976, 2014.

[97] Hyun Uk Lee, Soon Chang Lee, Jonghan Won, Byung-Chul Son, Saehae Choi, Yooseok Kim, So Young Park, Hee-Sik Kim, Young-Chul Lee, and Jouhahn Lee. Stable semiconductor black phosphorus (bp)@ titanium dioxide (tio 2) hybrid photocatalysts. *Sci. Rep.*, 5:8691, 2015.

[98] Jun Hu, Zhenkun Guo, Peter E Mcwilliams, John E Darges, Daniel L Druffel, Andrew M Moran, and Scott C Warren. Band gap engineering in a 2d material for solar-to-chemical energy conversion. *Nano Lett.*, 16:74–79, 2015.

[99] Xianjun Zhu, Taiming Zhang, Zijun Sun, Huanlin Chen, Jian Guan, Xiang Chen, Hengxing Ji, Pingwu Du, and Shangfeng Yang. Black phosphorus revisited: a missing metal-free elemental photocatalyst for visible light hydrogen evolution. *Adv. Mater.*, 29:1605776, 2017.

[100] Max Born and Robert Oppenheimer. Zur quantentheorie der molekeln. *Ann. Phys.*, 389:457–484, 1927.

[101] Max Born, Kun Huang, and M Lax. Dynamical theory of crystal lattices. *Am. J. Phys.*, 23:474–474, 1955.

[102] Douglas R Hartree. The wave mechanics of an atom with a non-coulomb central field. part i. theory and methods. In *Mathematical Proceedings of the Cambridge Philosophical Society*, volume 24, pages 89–110. Cambridge university press, 1928.

[103] John C Slater. A simplification of the hartree-fock method. *Phys. Rev.*, 81:385, 1951.

[104] Vladimir Fock. Näherungsmethode zur lösung des quantenmechanischen mehrkörperproblems. *Z. Phys.*, 61:126–148, 1930.

[105] Llewellyn H Thomas. The calculation of atomic fields. In *Math. Proc. Camb. Philos. Soc.*, volume 23, pages 542–548. Cambridge University Press, 1927.

[106] Enrico Fermi. Statistical method to determine some properties of atoms. *Rend. Accad. Naz. Lincei*, 6(602-607), 1927.

[107] P. Hohenberg and W. Kohn. Inhomogeneous electron gas. *Phys. Rev.*, 136:B864–B871, Nov 1964.

[108] John P. Perdew, Kieron Burke, and Yue Wang. Generalized gradient approximation for the exchange-correlation hole of a many-electron system. *Phys. Rev. B*, 54:16533–16539, 1996.

[109] JP Perdew. Jp perdew and a. zunger, phys. rev. b 23, 5048 (1981). *Phys. Rev. B*, 23:5048, 1981.

[110] Lars Hedin and Bengt I Lundqvist. Explicit local exchange-correlation potentials. *J. Phys. C: Solid State Phys.*, 4:2064, 1971.

[111] Eugene Wigner. On the interaction of electrons in metals. *Phys. Rev.*, 46:1002, 1934.

[112] John P Perdew, Kieron Burke, and Matthias Ernzerhof. Generalized gradient approximation made simple. *Phys. Rev. Lett.*, 77:3865, 1996.

[113] Jochen Heyd, Gustavo E Scuseria, and Matthias Ernzerhof. Hybrid functionals based on a screened coulomb potential. *J. Chem. Phys.*, 118:8207–8215, 2003.

[114] Jochen Heyd and Gustavo E Scuseria. Efficient hybrid density functional calculations in solids: Assessment of the heyd–scuseria–ernzerhof screened coulomb hybrid functional. *J. Chem. Phys.*, 121:1187–1192, 2004.

[115] Jochen Heyd and Gustavo E Scuseria. Assessment and validation of a screened coulomb hybrid density functional. *J. Chem. Phys.*, 120:7274–7280, 2004.

[116] Juan E. Peralta, Jochen Heyd, Gustavo E. Scuseria, and Richard L. Martin. Spin-orbit splittings and energy band gaps calculated with the heyd-scuseria-ernzerhof screened hybrid functional. *Phys. Rev. B*, 74:073101, 2006.

[117] John P Perdew, Matthias Ernzerhof, and Kieron Burke. Rationale for mixing exact exchange with density functional approximations. *J. Chem. Phys.*, 105(22):9982–9985, 1996.

[118] S. Lebègue, B. Arnaud, M. Alouani, and P. E. Bloechl. Implementation of an all-electron gw approximation based on the projector augmented wave method without plasmon pole approximation: Application to si, sic, alas, inas, nah, and kh. *Phys. Rev. B*, 67:155208, 2003.

[119] M. Shishkin and G. Kresse. Implementation and performance of the frequency-dependent *gw* method within the paw framework. *Phys. Rev. B*, 74:035101, 2006.

[120] M. van Schilfgaarde, Takao Kotani, and S. Faleev. Quasiparticle self-consistent *gw* theory. *Phys. Rev. Lett.*, 96:226402, 2006.

[121] Lars Hedin. New method for calculating the one-particle green's function with application to the electron-gas problem. *Phys. Rev.*, 139:A796–A823, 1965.

[122] M. Shishkin and G. Kresse. Self-consistent *gw* calculations for semiconductors and insulators. *Phys. Rev. B*, 75:235102, 2007.

[123] Michael Rohlfing and Steven G. Louie. Electron-hole excitations in semiconductors and insulators. *Phys. Rev. Lett.*, 81:2312–2315, 1998.

[124] Michael Rohlfing, Peter Krüger, and Johannes Pollmann. Quasiparticle band structure of cds. *Phys. Rev. Lett.*, 75:3489–3492, 1995.

[125] Michael Rohlfing and Steven G. Louie. Excitonic effects and the optical absorption spectrum of hydrogenated si clusters. *Phys. Rev. Lett.*, 80:3320–3323, 1998.

[126] George W. Crabtree, Mildred S. Dresselhaus, and Michelle V. Buchanan. The hydrogen economy. *Phys. Today*, 57:39–44, 2004.

[127] AKIRA Fujishima and KENICHI Honda. Electrochemical photolysis of water at a semiconductor electrode. *Nature*, 238:37–38, 1972.

[128] Xiaobo Chen, Shaohua Shen, Liejin Guo, and Samuel S. Mao. Semiconductor-based photocatalytic hydrogen generation. *Chem. Rev.*, 110:6503–6570, 2010.

[129] Arunima K. Singh, Kiran Mathew, Houlong L. Zhuang, and Richard G. Hennig. Computational screening of 2d materials for photocatalysis. *J. Phys. Chem. Lett.*, 6:1087–1098, 2015.

[130] Akio Ishikawa, Tsuyoshi Takata, Junko N. Kondo, Michikazu Hara, Hisayoshi Kobayashi, and Kazunari Domen. Oxysulfide $sm_2ti_2s_2o_5$ as a stable photocatalyst for water oxidation and reduction under visible light irradiation ($\lambda \leq 650$ nm). *J. Am. Chem. Soc.*, 124:13547–13553, 2002.

[131] Issei Tsuji, Hideki Kato, Hisayoshi Kobayashi, and Akihiko Kudo. Photocatalytic h_2 evolution reaction from aqueous solutions over band structure-controlled $(agin)_x zn_{2(1-x)}s_2$ solid solution photocatalysts with visible-light response and their surface nanostructures. *J. Am. Chem. Soc.*, 126:13406–13413, 2004.

[132] Issei Tsuji, Hideki Kato, and Akihiko Kudo. Visible-light-induced h_2 evolution from an aqueous solution containing sulfide and sulfite over

a znscuins$_2$agins$_2$ solid-solution photocatalyst. *Angew. Chem., Int. Ed.*, 44:3565–3568, 2005.

[133] Kazuhiko Maeda, Kentaro Teramura, Daling Lu, Tsuyoshi Takata, Nobuo Saito, Yasunobu Inoue, and Kazunari Domen. Photocatalyst releasing hydrogen from water. *Nature*, 440:295–295, 2006.

[134] Yungi Lee, Hiroaki Terashima, Yoshiki Shimodaira, Kentaro Teramura, Michikazu Hara, Hisayoshi Kobayashi, Kazunari Domen, and Masatomo Yashima. Zinc germanium oxynitride as a photocatalyst for overall water splitting under visible light. *J. Phys. Chem. C*, 111:1042–1048, 2007.

[135] Yongfu Sun, Hao Cheng, Shan Gao, Zhihu Sun, Qinghua Liu, Qin Liu, Fengcai Lei, Tao Yao, Jingfu He, Shiqiang Wei, and Yi Xie. Freestanding tin disulfide single-layers realizing efficient visible-light water splitting. *Angew. Chem., Int. Ed.*, 51:8727–8731, 2012.

[136] Yongjing Lin, Guangbi Yuan, Rui Liu, Sa Zhou, Stafford W. Sheehan, and Dunwei Wang. Semiconductor nanostructure-based photoelectrochemical water splitting: A brief review. *Chem. Phys. Lett.*, 507:209 – 215, 2011.

[137] Maggie Paulose, Karthik Shankar, Sorachon Yoriya, Haripriya E. Prakasam, Oomman K. Varghese, Gopal K. Mor, Thomas A. Latempa, Adriana Fitzgerald, and Craig A. Grimes. Anodic growth of highly ordered tio2 nanotube arrays to 134 μm in length. *J. Phys. Chem. B*, 110:16179–16184, 2006.

[138] Yongfu Sun, Zhihu Sun, Shan Gao, Hao Cheng, Qinghua Liu, Junyu Piao, Tao Yao, Changzheng Wu, Shuanglin Hu, Shiqiang Wei, and Yi Xie. Fabrication of flexible and freestanding zinc chalcogenide single layers. *Nature Commun.*, 3:1057 –, 2012.

[139] Damien Voiry, Hisato Yamaguchi, Junwen Li, Rafael Silva, Diego C. B. Alves, Takeshi Fujita, Mingwei Chen, Tewodros Asefa, Vivek B. Shenoy, Goki Eda, and Manish Chhowalla. Enhanced catalytic activity in strained chemically exfoliated ws2 nanosheets for hydrogen evolution. *Nat. Mater.*, 12:850–855, 2013.

[140] Yongfu Sun, Zhihu Sun, Shan Gao, Hao Cheng, Qinghua Liu, Fengcai Lei, Shiqiang Wei, and Yi Xie. All-surface-atomic-metal chalcogenide sheets for high-efficiency visible-light photoelectrochemical water splitting. *Adv. Energy Mater.*, 4:1300611–n/a, 2014.

[141] Xinchen Wang, Kazuhiko Maeda, Arne Thomas, Kazuhiro Takanabe, Gang Xin, Johan M. Carlsson, Kazunari Domen, and Markus Antonietti. A metal-free polymeric photocatalyst for hydrogen production from water under visible light. *Nat. Mater.*, 8:76–80, 2009.

[142] Juan Liu, Yang Liu, Naiyun Liu, Yuzhi Han, Xing Zhang, Hui Huang, Yeshayahu Lifshitz, Shuit-Tong Lee, Jun Zhong, and Zhenhui Kang. Metal-free efficient photocatalyst for stable visible water splitting via a two-electron pathway. *Science*, 347:970–974, 2015.

[143] Wee-Jun Ong, Lling-Lling Tan, Yun Hau Ng, Siek-Ting Yong, and Siang-Piao Chai. Graphitic carbon nitride (g-c3n4)-based photocatalysts for artificial photosynthesis and environmental remediation: Are we a step closer to achieving sustainability? *Chem. Rev.*, 116:7159–7329, 2016.

[144] David James Martin, Kaipei Qiu, Stephen Andrew Shevlin, Albertus Denny Handoko, Xiaowei Chen, Zhengxiao Guo, and Junwang Tang. Highly efficient photocatalytic h2 evolution from water using visible light and

structure-controlled graphitic carbon nitride. *Angew. Chem., Int. Ed.*, 53:9240–9245, 2014.

[145] Likai Li, Yijun Yu, Guo Jun Ye, Qingqin Ge, Xuedong Ou, Hua Wu, Donglai Feng, Xian Hui Chen, and Yuanbo Zhang. Black phosphorus field-effect transistors. *Nat. Nano.*, 9:372–377, 2014.

[146] Steven P. Koenig, Rostislav A. Doganov, Hennrik Schmidt, A. H. Castro Neto, and Barbaros Özyilmaz. Electric field effect in ultrathin black phosphorus. *Appl. Phys. Lett.*, 104:103106, 2014.

[147] Han Liu, Adam T. Neal, Zhen Zhu, Zhe Luo, Xianfan Xu, David Tománek, and Peide D. Ye. Phosphorene: An unexplored 2d semiconductor with a high hole mobility. *ACS Nano*, 8:4033–4041, 2014.

[148] Alexandra Carvalho, Min Wang, Xi Zhu, Aleksandr S. Rodin, Haibin Su, and Antonio H. Castro Neto. Phosphorene: From theory to applications. *Nat. Rev. Mater.*, 1:16061 –, 2016.

[149] Rohit Babar and Mukul Kabir. Transition metal and vacancy defect complexes in phosphorene: A spintronic perspective. *J. Phys. Chem. C*, 120:14991–15000, 2016.

[150] Jingsi Qiao, Xianghua Kong, Zhi-Xin Hu, Feng Yang, and Wei Ji. High-mobility transport anisotropy and linear dichroism in few-layer black phosphorus. *Nature Commun.*, 5:4475 –, 2014.

[151] Xiaomu Wang, Aaron M. Jones, Kyle L. Seyler, Vy Tran, Yichen Jia, Huan Zhao, Han Wang, Li Yang, Xiaodong Xu, and Fengnian Xia. Highly anisotropic and robust excitons in monolayer black phosphorus. *Nat. Nano.*, 10:517–521, 2015.

[152] Hongtao Yuan, Xiaoge Liu, Farzaneh Afshinmanesh, Wei Li, Gang Xu, Jie Sun, Biao Lian, Alberto G. Curto, Guojun Ye, Yasuyuki Hikita, Zhixun Shen, Shou-Cheng Zhang, Xianhui Chen, Mark Brongersma, Harold Y. Hwang, and Yi Cui. Polarization-sensitive broadband photodetector using a black phosphorus vertical p–n junction. *Nat. Nano.*, 10:707–713, 2015.

[153] Mohammad Ziaur Rahman, Chi Wai Kwong, Kenneth Davey, and Shi Zhang Qiao. 2d phosphorene as a water splitting photocatalyst: fundamentals to applications. *Energy Environ. Sci.*, 9:709–728, 2016.

[154] Baisheng Sa, Yan-Ling Li, Jingshan Qi, Rajeev Ahuja, and Zhimei Sun. Strain engineering for phosphorene: The potential application as a photocatalyst. *J. Phys. Chem. C*, 118:26560–26568, 2014.

[155] Hongyan Guo, Ning Lu, Jun Dai, Xiaojun Wu, and Xiao Cheng Zeng. Phosphorene nanoribbons, phosphorus nanotubes, and van der waals multilayers. *J. Phys. Chem. C*, 118:14051–14059, 2014.

[156] Le Huang, Nengjie Huo, Yan Li, Hui Chen, Juehan Yang, Zhongming Wei, Jingbo Li, and Shu-Shen Li. Electric-field tunable band offsets in black phosphorus and mos2 van der waals p-n heterostructure. *J. Phys. Chem. Lett.*, 6:2483–2488, 2015.

[157] Hyun Uk Lee, Soon Chang Lee, Jonghan Won, Byung-Chul Son, Saehae Choi, Yooseok Kim, So Young Park, Hee-Sik Kim, Young-Chul Lee, and Jouhahn Lee. Stable semiconductor black phosphorus (bp)@titanium dioxide (tio2) hybrid photocatalysts. *Sci. Rep.*, 5:8691, 2015.

[158] Jun Hu, Zhenkun Guo, Peter E. Mcwilliams, John E. Darges, Daniel L. Druffel, Andrew M. Moran, and Scott C. Warren. Band gap engineering in a 2d material for solar-to-chemical energy conversion. *Nano Lett.*, 16:74–79, 2016.

[159] Joshua D. Wood, Spencer A. Wells, Deep Jariwala, Kan-Sheng Chen, EunKyung Cho, Vinod K. Sangwan, Xiaolong Liu, Lincoln J. Lauhon, Tobin J. Marks, and Mark C. Hersam. Effective passivation of exfoliated black phosphorus transistors against ambient degradation. *Nano Lett.*, 14:6964–6970, 2014.

[160] Jiajie Pei, Xin Gai, Jiong Yang, Xibin Wang, Zongfu Yu, Duk-Yong Choi, Barry Luther-Davies, and Yuerui Lu. Producing air-stable monolayers of phosphorene and their defect engineering. *Nature Commun.*, 7:10450, 2016.

[161] Xianjun Zhu, Taiming Zhang, Zijun Sun, Huanlin Chen, Jian Guan, Xiang Chen, Hengxing Ji, Pingwu Du, and Shangfeng Yang. Black phosphorus revisited: A missing metal-free elemental photocatalyst for visible light hydrogen evolution. *Adv. Mater.*, 29:1605776–n/a, 2017.

[162] G. Kresse and J. Hafner. Ab initio molecular dynamics for liquid metals. *Phys. Rev. B*, 47:558–561, 1993.

[163] G. Kresse and J. Furthmüller. Efficient iterative schemes for ab initio total-energy calculations using a plane-wave basis set. *Phys. Rev. B*, 54:11169–11186, 1996.

[164] P. E. Blöchl. Projector augmented-wave method. *Phys. Rev. B*, 50:17953–17979, 1994.

[165] John P. Perdew, Kieron Burke, and Matthias Ernzerhof. Generalized gradient approximation made simple. *Phys. Rev. Lett.*, 77:3865–3868, 1996.

[166] Hendrik J. Monkhorst and James D. Pack. Special points for brillouin-zone integrations. *Phys. Rev. B*, 13:5188–5192, 1976.

[167] Jochen Heyd, Gustavo E. Scuseria, and Matthias Ernzerhof. Hybrid functionals based on a screened coulomb potential. *J. Chem. Phys.*, 118:8207–8215, 2003.

[168] Aliaksandr V. Krukau, Oleg A. Vydrov, Artur F. Izmaylov, and Gustavo E. Scuseria. Influence of the exchange screening parameter on the performance of screened hybrid functionals. *J. Chem. Phys.*, 125(22):224106, 2006.

[169] Stefan Grimme, Jens Antony, Stephan Ehrlich, and Helge Krieg. A consistent and accurate ab initio parametrization of density functional dispersion correction (dft-d) for the 94 elements h-pu. *J. Chem. Phys.*, 132:154104, 2010.

[170] Stefan Grimme, Stephan Ehrlich, and Lars Goerigk. Effect of the damping function in dispersion corrected density functional theory. *J. Comp. Chem.*, 32:1456–1465, 2011.

[171] Liangbo Liang, Jun Wang, Wenzhi Lin, Bobby G. Sumpter, Vincent Meunier, and Minghu Pan. Electronic bandgap and edge reconstruction in phosphorene materials. *Nano Lett.*, 14:6400–6406, 2014.

[172] Yuanyue Liu, Fangbo Xu, Ziang Zhang, Evgeni S. Penev, and Boris I. Yakobson. Two-dimensional mono-elemental semiconductor with electronically inactive defects: The case of phosphorus. *Nano Lett.*, 14:6782–6786, 2014.

[173] Yan Li, Shengxue Yang, and Jingbo Li. Modulation of the electronic properties of ultrathin black phosphorus by strain and electrical field. *J. Phys. Chem. C*, 118:23970–23976, 2014.

[174] Vy Tran, Ryan Soklaski, Yufeng Liang, and Li Yang. Layer-controlled band gap and anisotropic excitons in few-layer black phosphorus. *Phys. Rev. B*, 89:235319, 2014.

[175] Jin-Ho Choi, Ping Cui, Haiping Lan, and Zhenyu Zhang. Linear scaling of the exciton binding energy versus the band gap of two-dimensional materials. *Phys. Rev. Lett.*, 115:066403, 2015.

[176] A. Brown and S. Rundqvist. Refinement of the Crystal Structure of Black Phosphorus. *Acta Crystallogr.*, 19:684–685, 1965.

[177] A. Ziletti, A. Carvalho, D. K. Campbell, D. F. Coker, and A. H. Castro Neto. Oxygen defects in phosphorene. *Phys. Rev. Lett.*, 114:046801, 2015.

[178] Xavier Gonze and Changyol Lee. Dynamical matrices, born effective charges, dielectric permittivity tensors, and interatomic force constants from density-functional perturbation theory. *Phys. Rev. B*, 55:10355–10368, 1997.

[179] A Togo and I Tanaka. First principles phonon calculations in materials science. *Scr. Mater.*, 108:1–5, 2015.

[180] Qun Wei and Xihong Peng. Superior mechanical flexibility of phosphorene and few-layer black phosphorus. *Appl. Phys. Lett.*, 104:251915, 2014.

[181] Vidhya Chakrapani, John C. Angus, Alfred B. Anderson, Scott D. Wolter, Brian R. Stoner, and Gamini U. Sumanasekera. Charge transfer equilibria between diamond and an aqueous oxygen electrochemical redox couple. *Science*, 318:1424–1430, 2007.

[182] Junfeng Gao, Gang Zhang, and Yong-Wei Zhang. Vastly enhancing the chemical stability of phosphorene by employing an electric field. *Nanoscale*, 9:4219–4226, 2017.

[183] L. Shulenburger, A.D. Baczewski, Z. Zhu, J. Guan, and D. Tománek. The nature of the interlayer interaction in bulk and few-layer phosphorus. *Nano Lett.*, 15:8170–8175, 2015.

[184] Jun Dai and Xiao Cheng Zeng. Bilayer phosphorene: Effect of stacking order on bandgap and its potential applications in thin-film solar cells. *J. Phys. Chem. Lett.*, 5:1289–1293, 2014.

[185] J. Tersoff. Theory of semiconductor heterojunctions: The role of quantum dipoles. *Phys. Rev. B*, 30:4874–4877, 1984.

[186] Yongqing Cai, Qingqing Ke, Gang Zhang, and Yong-Wei Zhang. Energetics, charge transfer, and magnetism of small molecules physisorbed on phosphorene. *J. Phys. Chem. C*, 119(6):3102–3110, 2015.

[187] Yuan Huang, Jingsi Qiao, Kai He, Stoyan Bliznakov, Eli Sutter, Xianjue Chen, Da Luo, Fanke Meng, Dong Su, Jeremy Decker, Wei Ji, Rodney S. Ruoff, and Peter Sutter. Interaction of black phosphorus with oxygen and water. *Chem. Mater.*, 28(22):8330–8339, 2016.

[188] M. Gajdoš, K. Hummer, G. Kresse, J. Furthmüller, and F. Bechstedt. Linear optical properties in the projector-augmented wave methodology. *Phys. Rev. B*, 73:045112, 2006.

[189] Timothy C. Berkelbach, Mark S. Hybertsen, and David R. Reichman. Theory of neutral and charged excitons in monolayer transition metal dichalcogenides. *Phys. Rev. B*, 88:045318, 2013.

[190] Elsa Prada, J. V. Alvarez, K. L. Narasimha-Acharya, F. J. Bailen, and J. J. Palacios. Effective-mass theory for the anisotropic exciton in two-dimensional crystals: Application to phosphorene. *Phys. Rev. B*, 91:245421, 2015.

[191] Thomas Olsen, Simone Latini, Filip Rasmussen, and Kristian S. Thygesen. Simple screened hydrogen model of excitons in two-dimensional materials. *Phys. Rev. Lett.*, 116:056401, 2016.

[192] Deniz Çakır, Cem Sevik, and Francois M. Peeters. Significant effect of atacking on the electronic and optical properties of few-layer black phosphorus. *Phys. Rev. B*, 92:165406, 2015.

[193] Francesco Bonaccorso, Luigi Colombo, Guihua Yu, Meryl Stoller, Valentina Tozzini, Andrea C. Ferrari, Rodney S. Ruoff, and Vittorio Pellegrini. Graphene, related two-dimensional crystals, and hybrid systems for energy conversion and storage. *Science*, 347, 2015.

[194] Chaoliang Tan and Hua Zhang. Wet-chemical synthesis and applications of non-layer structured two-dimensional nanomaterials. *Nat. Commun.*, 6:7873, 2015.

[195] Bin Luo, Gang Liu, and Lianzhou Wang. Recent advances in 2d materials for photocatalysis. *Nanoscale*, 8:6904–6920, 2016.

[196] Chaoliang Tan, Xiehong Cao, Xue-Jun Wu, Qiyuan He, Jian Yang, Xiao Zhang, Junze Chen, Wei Zhao, Shikui Han, Gwang-Hyeon Nam, Melinda Sindoro, and Hua Zhang. Recent advances in ultrathin two-dimensional nanomaterials. *Chem. Rev.*, 117:6225–6331, 2017.

[197] Jun Di, Jun Xiong, Huaming Li, and Zheng Liu. Ultrathin 2d photocatalysts: Electronic-structure tailoring, hybridization, and applications. *Adv. Mater.*, 30:1704548, 2018.

[198] Alexey Chernikov, Timothy C. Berkelbach, Heather M. Hill, Albert Rigosi, Yilei Li, Ozgur Burak Aslan, David R. Reichman, Mark S. Hybertsen, and Tony F. Heinz. Exciton binding energy and nonhydrogenic rydberg series in monolayer ws_2. *Phys. Rev. Lett.*, 113:076802, 2014.

[199] Miguel M. Ugeda, Aaron J. Bradley, Su-Fei Shi, Felipe H. da Jornada, Yi Zhang, Diana Y. Qiu, Wei Ruan, Sung-Kwan Mo, Zahid Hussain, Zhi-

Xun Shen, Feng Wang, Steven G. Louie, and Michael F. Crommie. Giant bandgap renormalization and excitonic effects in a monolayer transition metal dichalcogenide semiconductor. *Nat. Mater.*, 13:1091–1095, 2014.

[200] Xiaomu Wang, Aaron M. Jones, Kyle L. Seyler, Vy Tran, Yichen Jia, Huan Zhao, Han Wang, Li Yang, Xiaodong Xu, and Fengnian Xia. Highly anisotropic and robust excitons in monolayer black phosphorus. *Nat. Nano.*, 10:517–521, 2015.

[201] Srilatha Arra, Rohit Babar, and Mukul Kabir. Exciton in phosphorene: Strain, impurity, thickness, and heterostructure. *Phys. Rev. B*, 99:045432, 2019.

[202] Mollie R. Waller, Troy K. Townsend, Jing Zhao, Erwin M. Sabio, Rachel L. Chamousis, Nigel D. Browning, and Frank E. Osterloh. Single-crystal tungsten oxide nanosheets: Photochemical water oxidation in the quantum confinement regime. *Chem. Mater.*, 24:698–704, 2012.

[203] Jixin Zhu, Zongyou Yin, Dan Yang, Ting Sun, Hong Yu, Harry E. Hoster, Huey Hoon Hng, Hua Zhang, and Qingyu Yan. Hierarchical hollow spheres composed of ultrathin fe2o3 nanosheets for lithium storage and photocatalytic water oxidation. *Energy Environ. Sci.*, 6:987–993, 2013.

[204] Di Liu, Yanhui Lv, Mo Zhang, Yanfang Liu, Yanyan Zhu, Ruilong Zong, and Yongfa Zhu. Defect-related photoluminescence and photocatalytic properties of porous zno nanosheets. *J. Mater. Chem. A*, 2:15377–15388, 2014.

[205] Jiao Yang, Yi-Lin Jiang, Lin-Jie Li, Elisée Muhire, and Mei-Zhen Gao. High-performance photodetectors and enhanced photocatalysts of two-dimensional tio2 nanosheets under uv light excitation. *Nanoscale*, 8:8170–8177, 2016.

[206] Huajie Yin and Zhiyong Tang. Ultrathin two-dimensional layered metal hydroxides: an emerging platform for advanced catalysis, energy conversion and storage. *Chem. Soc. Rev.*, 45:4873–4891, 2016.

[207] Yongfu Sun, Zhihu Sun, Shan Gao, Hao Cheng, Qinghua Liu, Junyu Piao, Tao Yao, Changzheng Wu, Shuanglin Hu, Shiqiang Wei, and Yi Xie. Fabrication of flexible and freestanding zinc chalcogenide single layers. *Nat. Commun.*, 3:1057, 2012.

[208] Yongfu Sun, Hao Cheng, Shan Gao, Zhihu Sun, Qinghua Liu, Qin Liu, Fengcai Lei, Tao Yao, Jingfu He, Shiqiang Wei, and Yi Xie. Freestanding tin disulfide single-layers realizing efficient visible-light water splitting. *Angew. Chem. Int. Ed.*, 124:8857–8861, 2012.

[209] Damien Voiry, Hisato Yamaguchi, Junwen Li, Rafael Silva, Diego C. B. Alves, Takeshi Fujita, Mingwei Chen, Tewodros Asefa, Vivek B. Shenoy, Goki Eda, and Manish Chhowalla. Enhanced catalytic activity in strained chemically exfoliated ws2 nanosheets for hydrogen evolution. *Nat. Mater.*, 12:850, 2013.

[210] Eric Parzinger, Bastian Miller, Benno Blaschke, Jose A. Garrido, Joel W. Ager, Alexander Holleitner, and Ursula Wurstbauer. Photocatalytic stability of single- and few-layer mos2. *ACS Nano*, 9:11302–11309, 2015.

[211] Xinchen Wang, Kazuhiko Maeda, Arne Thomas, Kazuhiro Takanabe, Gang Xin, Johan M. Carlsson, Kazunari Domen, and Markus Antonietti. A metal-free polymeric photocatalyst for hydrogen production from water under visible light. *Nat. Mater.*, 8:76, 11 2008.

[212] Juan Liu, Yang Liu, Naiyun Liu, Yuzhi Han, Xing Zhang, Hui Huang, Yeshayahu Lifshitz, Shuit-Tong Lee, Jun Zhong, and Zhenhui Kang. Metal-

free efficient photocatalyst for stable visible water splitting via a two-electron pathway. *Science*, 347:970–974, 2015.

[213] Guigang Zhang, Mingwen Zhang, Xinxin Ye, Xiaoqing Qiu, Sen Lin, and Xinchen Wang. Iodine modified carbon nitride semiconductors as visible light photocatalysts for hydrogen evolution. *Adv. Mater.*, 26:805–809, 2013.

[214] Xiaojie She, Jingjie Wu, Jun Zhong, Hui Xu, Yingchao Yang, Robert Vajtai, Jun Lou, Yang Liu, Daolin Du, Huaming Li, and Pulickel M. Ajayan. Oxygenated monolayer carbon nitride for excellent photocatalytic hydrogen evolution and external quantum efficiency. *Nano Energy*, 27:138 – 146, 2016.

[215] Srilatha Arra, K. R. Ramya, Rohit Babar, and Mukul Kabir. Photocatalytic activity of phosphorene derivatives: Coverage, electronic, optical, and excitonic properties. *J. Phys. Chem. C*, 122:7194–7202, 2018.

[216] Zhenzhen Lin and Xinchen Wang. Nanostructure engineering and doping of conjugated carbon nitride semiconductors for hydrogen photosynthesis. *Angew. Chem. Int. Ed.*, 52:1735–1738, 2013.

[217] Jingrun Ran, Tian Yi Ma, Guoping Gao, Xi-Wen Du, and Shi Zhang Qiao. Porous p-doped graphitic carbon nitride nanosheets for synergistically enhanced visible-light photocatalytic h2 production. *Energy Environ. Sci.*, 8:3708–3717, 2015.

[218] Changhui Ye, Yoshio Bando, Guozhen Shen, and Dmitri Golberg. Thickness-dependent photocatalytic performance of zno nanoplatelets. *J. Phys. Chem. B*, 110:15146–15151, 2006.

[219] Qinghua Liang, Zhi Li, Zheng-Hong Huang, Feiyu Kang, and Quan-Hong Yang. Holey graphitic carbon nitride nanosheets with carbon vacancies for

highly improved photocatalytic hydrogen production. *Adv. Funct. Mater.*, 25:6885–6892, 2015.

[220] Youwen Liu, Chong Xiao, Zhou Li, and Yi Xie. Vacancy engineering for tuning electron and phonon structures of two-dimensional materials. *Adv. Energy Mater.*, 6:1600436, 2016.

[221] Yidong Hou, Anders B. Laursen, Jinshui Zhang, Guigang Zhang, Yongsheng Zhu, Xinchen Wang, Soren Dahl, and Ib Chorkendorff. Layered nanojunctions for hydrogen-evolution catalysis. *Angew. Chem. Int. Ed.*, 52:3621–3625, 2013.

[222] Junze Chen, Xue-Jun Wu, Lisha Yin, Bing Li, Xun Hong, Zhanxi Fan, Bo Chen, Can Xue, and Hua Zhang. One-pot synthesis of cds nanocrystals hybridized with single-layer transition-metal dichalcogenide nanosheets for efficient photocatalytic hydrogen evolution. *Angew. Chem. Int. Ed.*, 127:1226–1230, 2015.

[223] Zhenyi Zhang, Jindou Huang, Mingyi Zhang, Qing Yuan, and Bin Dong. Ultrathin hexagonal sns2 nanosheets coupled with g-c3n4 nanosheets as 2d/2d heterojunction photocatalysts toward high photocatalytic activity. *Appl. Catal. B*, 163:298 – 305, 2015.

[224] Jie Li, Guangming Zhan, Ying Yu, and Lizhi Zhang. Superior visible light hydrogen evolution of janus bilayer junctions via atomic-level charge flow steering. *Nat. Commun.*, 7:11480, 2016.

[225] Yong-Jun Yuan, Zhi-Jun Ye, Hong-Wei Lu, Bin Hu, Yong-Hui Li, Da-Qin Chen, Jia-Song Zhong, Zhen-Tao Yu, and Zhi-Gang Zou. Constructing anatase tio2 nanosheets with exposed (001) facets/layered mos2 two-

dimensional nanojunctions for enhanced solar hydrogen generation. *ACS Catal.*, 6:532–541, 2016.

[226] Ang-Yu Lu, Hanyu Zhu, Jun Xiao, Chih-Piao Chuu, Yimo Han, Ming-Hui Chiu, Chia-Chin Cheng, Chih-Wen Yang, Kung-Hwa Wei, Yiming Yang, Yuan Wang, Dimosthenis Sokaras, Dennis Nordlund, Peidong Yang, David A. Muller, Mei-Yin Chou, Xiang Zhang, and Lain-Jong Li. Janus monolayers of transition metal dichalcogenides. *Nat. Nano.*, 12:744, 2017.

[227] Jing Zhang, Shuai Jia, Iskandar Kholmanov, Liang Dong, Dequan Er, Weibing Chen, Hua Guo, Zehua Jin, Vivek B. Shenoy, Li Shi, and Jun Lou. Janus monolayer transition-metal dichalcogenides. *ACS Nano*, 11:8192–8198, 2017.

[228] Sigismund Melissen, Tangui Le Bahers, Stephan N. Steinmann, and Philippe Sautet. Relationship between carbon nitride structure and exciton binding energies: A dft perspective. *J. Phys. Chem. C*, 119:25188–25196, 2015.

[229] Gerardo Algara-Siller, Nikolai Severin, Samantha Y. Chong, Torbjorn Bjorkman, Robert G. Palgrave, Andrea Laybourn, Markus Antonietti, Yaroslav Z. Khimyak, Arkady V. Krasheninnikov, Jorgen P. Rabe, Ute Kaiser, Andrew I. Cooper, Arne Thomas, and Michael J. Bojdys. Triazine-based graphitic carbon nitride: a two-dimensional semiconductor. *Angew. Chem. Int. Ed.*, 53:7450–7455, 2014.

[230] M. Dion, H. Rydberg, E. Schröder, D. C. Langreth, and B. I. Lundqvist. Van der waals density functional for general geometries. *Phys. Rev. Lett.*, 92:246401, 2004.

[231] J. Klimes, David R Bowler, and Angelos Michaelides. Chemical accuracy for the van der waals density functional. *J. Phys.: Cond. Matt.*, 22:022201, 2010.

[232] Jiajun Wang, Zhaoyong Guan, Jing Huang, Qunxiang Li, and Jinlong Yang. Enhanced photocatalytic mechanism for the hybrid g-c3n4/mos2 nanocomposite. *J. Mater. Chem. A*, 2:7960–7966, 2014.

[233] Yujin Ji, Mingye Yang, Haiping Lin, Tingjun Hou, Lu Wang, Youyong Li, and Shuit-Tong Lee. Janus structures of transition metal dichalcogenides as the heterojunction photocatalysts for water splitting. *J. Phys. Chem. C*, 122:3123–3129, 2018.

[234] Xiangchao Ma, Xin Wu, Haoda Wang, and Yucheng Wang. A janus mosse monolayer: a potential wide solar-spectrum water-splitting photocatalyst with a low carrier recombination rate. *J. Mater. Chem. A*, 6:2295–2301, 2018.

[235] Mattias Palsgaard, Tue Gunst, Troels Markussen, Kristian Sommer Thygesen, and Mads Brandbyge. Stacked janus device concepts: Abrupt pn-junctions and cross-plane channels. *Nano Lett.*, 18:7275–7281, 2018.

[236] Cen-Feng Fu, Jiuyu Sun, Qiquan Luo, Xingxing Li, Wei Hu, and Jinlong Yang. Intrinsic electric fields in two-dimensional materials boost the solar-to-hydrogen efficiency for photocatalytic water splitting. *Nano Lett.*, 18:6312–6317, 2018.

[237] Zhebo Chen, Thomas F. Jaramillo, Todd G. Deutsch, Alan Kleiman-Shwarsctein, Arnold J. Forman, Nicolas Gaillard, Roxanne Garland, Kazuhiro Takanabe, Clemens Heske, Mahendra Sunkara, Eric W. McFarland, Kazunari Domen, Eric L. Miller, John A. Turner, and Huyen N. Dinh. Accelerating materials development for photoelectrochemical hydrogen production: Standards for methods, definitions, and reporting protocols. *J. Mater. Res.*, 25:3–16, 2010.

[238] L. V. Keldysh. Coulomb interaction in thin semiconductor and semimetal films. *JETP Lett.*, 29:658, 1979.

[239] Lei Xu, Ming Yang, Shi Jie Wang, and Yuan Ping Feng. Electronic and optical properties of the monolayer group-iv monochalcogenides mx ($m = \mathrm{Ge},\ \mathrm{Sn}$; $x = \mathrm{S},\ \mathrm{Se},\ \mathrm{Te}$). *Phys. Rev. B*, 95:235434, 2017.

[240] Pierluigi Cudazzo, Ilya V. Tokatly, and Angel Rubio. Dielectric screening in two-dimensional insulators: Implications for excitonic and impurity states in graphane. *Phys. Rev. B*, 84:085406, 2011.

[241] E. E. Salpeter and H. A. Bethe. A relativistic equation for bound-state problems. *Phys. Rev.*, 84:1232–1242, 1951.

[242] Stefan Albrecht, Lucia Reining, Rodolfo Del Sole, and Giovanni Onida. Ab initio calculation of excitonic effects in the optical spectra of semiconductors. *Phys. Rev. Lett.*, 80:4510–4513, 1998.

[243] Catalin D. Spataru, Sohrab Ismail-Beigi, Lorin X. Benedict, and Steven G. Louie. Excitonic effects and optical spectra of single-walled carbon nanotubes. *Phys. Rev. Lett.*, 92:077402, 2004.

[244] Ludger Wirtz, Andrea Marini, and Angel Rubio. Excitons in boron nitride nanotubes: Dimensionality effects. *Phys. Rev. Lett.*, 96:126104, 2006.

[245] Fabio Caruso, Marina R. Filip, and Feliciano Giustino. Excitons in one-dimensional van der waals materials: sb_2s_3 nanoribbons. *Phys. Rev. B*, 92:125134, 2015.

[246] Pierluigi Cudazzo, Lorenzo Sponza, Christine Giorgetti, Lucia Reining, Francesco Sottile, and Matteo Gatti. Exciton band structure in two-dimensional materials. *Phys. Rev. Lett.*, 116:066803, 2016.

[247] Kin Fai Mak and Jie Shan. Photonics and optoelectronics of 2d semiconductor transition metal dichalcogenides. *Nat. Photon.*, 10:216–226, 2016.

[248] Li Yang, Marvin L. Cohen, and Steven G. Louie. Excitonic effects in the optical spectra of graphene nanoribbons. *Nano Lett.*, 7:3112–3115, 2007.

[249] Chendong Zhang, Amber Johnson, Chang-Lung Hsu, Lain-Jong Li, and Chih-Kang Shih. Direct imaging of band profile in single layer mos2 on graphite: Quasiparticle energy gap, metallic edge states, and edge band bending. *Nano Lett.*, 14:2443–2447, 2014.

[250] Heather M. Hill, Albert F. Rigosi, Cyrielle Roquelet, Alexey Chernikov, Timothy C. Berkelbach, David R. Reichman, Mark S. Hybertsen, Louis E. Brus, and Tony F. Heinz. Observation of excitonic rydberg states in monolayer mos2 and ws2 by photoluminescence excitation spectroscopy. *Nano Lett.*, 15:2992–2997, 2015.

[251] A. R. Klots, A. K. M. Newaz, Bin Wang, D. Prasai, H. Krzyzanowska, Junhao Lin, D. Caudel, N. J. Ghimire, J. Yan, B. L. Ivanov, K. A. Velizhanin, A. Burger, D. G. Mandrus, N. H. Tolk, S. T. Pantelides, and K. I. Bolotin. Probing excitonic states in suspended two-dimensional semiconductors by photocurrent spectroscopy. *Sci. Rep.*, 4:6608, 2014.

[252] Nihit Saigal, Vasam Sugunakar, and Sandip Ghosh. Exciton binding energy in bulk mos2: A reassessment. *Appl. Phys. Lett.*, 108:132105, 2016.

[253] Diana Y. Qiu, Felipe H. da Jornada, and Steven G. Louie. Optical spectrum of mos_2: Many-body effects and diversity of exciton states. *Phys. Rev. Lett.*, 111:216805, 2013.

[254] Tim Byrnes, Na Young Kim, and Yoshihisa Yamamoto. Exciton-polariton condensates. *Nat. Phys.*, 10:803–813, 2014.

[255] Han Liu, Adam T. Neal, Zhen Zhu, Zhe Luo, Xianfan Xu, David Tománek, and Peide D. Ye. Phosphorene: An unexplored 2d semiconductor with a high hole mobility. *ACS Nano*, 8:4033–4041, 2014.

[256] Rohit Babar and Mukul Kabir. Transition metal and vacancy defect complexes in phosphorene: A spintronic perspective. *J. Phys. Chem. C*, 120:14991–15000, 2016.

[257] Alexandra Carvalho, Min Wang, Xi Zhu, Aleksandr S. Rodin, Haibin Su, and Antonio H. Castro Neto. Phosphorene: from theory to applications. *Nat. Rev. Mater.*, 1:16061, 2016.

[258] Srilatha Arra, K. R. Ramya, Rohit Babar, and Mukul Kabir. Photocatalytic activity of phosphorene derivatives: Coverage, electronic, optical, and excitonic properties. *J. Phys. Chem. C*, 122:7194–7202, 2018.

[259] Qihang Liu, Xiuwen Zhang, L. B. Abdalla, Adalberto Fazzio, and Alex Zunger. Switching a normal insulator into a topological insulator via electric field with application to phosphorene. *Nano Lett.*, 15:1222–1228, 2015.

[260] Jimin Kim, Seung Su Baik, Sae Hee Ryu, Yeongsup Sohn, Soohyung Park, Byeong-Gyu Park, Jonathan Denlinger, Yeonjin Yi, Hyoung Joon Choi, and Keun Su Kim. Observation of tunable band gap and anisotropic dirac semimetal state in black phosphorus. *Science*, 349:723–726, 2015.

[261] Rohit Babar and Mukul Kabir. Engineering the kondo state in two-dimensional semiconducting phosphorene. *Phys. Rev. B*, 97:045132, 2018.

[262] Giovanni Onida, Lucia Reining, and Angel Rubio. Electronic excitations: density-functional versus many-body green's-function approaches. *Rev. Mod. Phys.*, 74:601–659, 2002.

[263] Liangbo Liang, Jun Wang, Wenzhi Lin, Bobby G. Sumpter, Vincent Meunier, and Minghu Pan. Electronic bandgap and edge reconstruction in phosphorene materials. *Nano Lett.*, 14:6400–6406, 2014.

[264] Hongliang Shi, Hui Pan, Yong-Wei Zhang, and Boris I. Yakobson. Quasiparticle band structures and optical properties of strained monolayer mos_2 and ws_2. *Phys. Rev. B*, 87:155304, 2013.

[265] Ashwin Ramasubramaniam. Large excitonic effects in monolayers of molybdenum and tungsten dichalcogenides. *Phys. Rev. B*, 86:115409, 2012.

[266] Joshua D. Wood, Spencer A. Wells, Deep Jariwala, Kan-Sheng Chen, EunKyung Cho, Vinod K. Sangwan, Xiaolong Liu, Lincoln J. Lauhon, Tobin J. Marks, and Mark C. Hersam. Effective passivation of exfoliated black phosphorus transistors against ambient degradation. *Nano Lett.*, 14:6964–6970, 2014.

[267] Joshua O Island, Gary A Steele, Herre S J van der Zant, and Andres Castellanos-Gomez. Environmental instability of few-layer black phosphorus. *2D Mater.*, 2:011002, 2015.

[268] Alexandre Favron, Etienne Gaufrès, Frédéric Fossard, Anne-Laurence Phaneuf-L'Heureux, Nathalie Y-W. Tang, Pierre L. Lévesque, Annick Loiseau, Richard Leonelli, Sébastien Francoeur, and Richard Martel. Photooxidation and quantum confinement effects in exfoliated black phosphorus. *Nat. Mater.*, 14:826, 2015.

[269] Ahmet Avsar, Ivan J. Vera-Marun, Jun You Tan, Kenji Watanabe, Takashi Taniguchi, Antonio H. Castro Neto, and Barbaros Ozyilmaz. Air-stable transport in graphene-contacted, fully encapsulated ultrathin black phosphorus-based field-effect transistors. *ACS Nano*, 9:4138–4145, 2015.

[270] Rostislav A. Doganov, Eoin C. T. O'Farrell, Steven P. Koenig, Yuting Yeo, Angelo Ziletti, Alexandra Carvalho, David K. Campbell, David F. Coker, Kenji Watanabe, Takashi Taniguchi, Antonio H. Castro Neto, and Barbaros Özyilmaz. Transport properties of pristine few-layer black phosphorus by van der waals passivation in an inert atmosphere. *Nat. Commun.*, 6:6647, 2015.

[271] Xiaolong Chen, Yingying Wu, Zefei Wu, Yu Han, Shuigang Xu, Lin Wang, Weiguang Ye, Tianyi Han, Yuheng He, Yuan Cai, and Ning Wang. High-quality sandwiched black phosphorus heterostructure and its quantum oscillations. *Nat. Commun.*, 6:7315, 2015.

[272] Guillermo Román-Pérez and José M. Soler. Efficient implementation of a van der waals density functional: Application to double-wall carbon nanotubes. *Phys. Rev. Lett.*, 103:096102, Aug 2009.

[273] A. Brown and S. Rundqvist. Refinement of the crystal structure of black phosphorus. *Acta Cryst.*, 19:684–685, 1965.

[274] L. Cartz, S. R. Srinivasa, R. J. Riedner, J. D. Jorgensen, and T. G. Worlton. Effect of pressure on bonding in black phosphorus. *J. Chem. Phys.*, 71:1718–1721, 1979.

[275] G. Strinati. Effects of dynamical screening on resonances at inner-shell thresholds in semiconductors. *Phys. Rev. B*, 29:5718–5726, 1984.

[276] Gregory H. Wannier. The structure of electronic excitation levels in insulating crystals. *Phys. Rev.*, 52:191–197, 1937.

[277] A. N. Rudenko and M. I. Katsnelson. Quasiparticle band structure and tight-binding model for single- and bilayer black phosphorus. *Phys. Rev. B*, 89:201408, 2014.

[278] Xihong Peng, Qun Wei, and Andrew Copple. Strain-engineered direct-indirect band gap transition and its mechanism in two-dimensional phosphorene. *Phys. Rev. B*, 90:085402, 2014.

[279] Zhizhan Qiu, Hanyan Fang, Alexandra Carvalho, A. S. Rodin, Yanpeng Liu, Sherman J. R. Tan, Mykola Telychko, Pin Lv, Jie Su, Yewu Wang, A. H. Castro Neto, and Jiong Lu. Resolving the spatial structures of bound hole states in black phosphorus. *Nano Lett.*, 17:6935–6940, 2017.

[280] Deniz Çak ır, Hasan Sahin, and François M. Peeters. Tuning of the electronic and optical properties of single-layer black phosphorus by strain. *Phys. Rev. B*, 90:205421, 2014.

[281] Jason S. Ross, Philip Klement, Aaron M. Jones, Nirmal J. Ghimire, Jiaqiang Yan, D. G. Mandrus, Takashi Taniguchi, Kenji Watanabe, Kenji Kitamura, Wang Yao, David H. Cobden, and Xiaodong Xu. Electrically tunable excitonic light-emitting diodes based on monolayer wse2 p–n junctions. *Nat. Nano.*, 9:268, 2014.

[282] F. Withers, O. Del Pozo-Zamudio, A. Mishchenko, A. P. Rooney, A. Gholinia, K. Watanabe, T. Taniguchi, S. J. Haigh, A. K. Geim, A. I. Tartakovskii, and K. S. Novoselov. Light-emitting diodes by band-structure engineering in van der waals heterostructures. *Nat. Mater.*, 14:301, 2015.

[283] Shuang Zhang, Jiong Yang, Renjing Xu, Fan Wang, Weifeng Li, Muhammad Ghufran, Yong-Wei Zhang, Zongfu Yu, Gang Zhang, Qinghua Qin, and Yuerui Lu. Extraordinary photoluminescence and strong temperature/angle-dependent raman responses in few-layer phosphorene. *ACS Nano*, 8(9):9590–9596, 2014.

[284] Likai Li, Jonghwan Kim, Chenhao Jin, Guo Jun Ye, Diana Y. Qiu, Felipe H.

da Jornada, Zhiwen Shi, Long Chen, Zuocheng Zhang, Fangyuan Yang, Kenji Watanabe, Takashi Taniguchi, Wencai Ren, Steven G. Louie, Xian Hui Chen, Yuanbo Zhang, and Feng Wang. Direct observation of the layer-dependent electronic structure in phosphorene. *Nat. Nano.*, 12:21, 2016.

[285] Yuichi Akahama, Shoichi Endo, and Shin-ichiro Narita. Electrical properties of black phosphorus single crystals. *J. Phys. Soc. Jpn.*, 52:2148–2155, 1983.

[286] Kin Fai Mak, Changgu Lee, James Hone, Jie Shan, and Tony F. Heinz. Atomically thin mos_2: A new direct-gap semiconductor. *Phys. Rev. Lett.*, 105:136805, 2010.

[287] Toshiya Nagahama, Michihiro Kobayashi, Yuichi Akahama, Shoichi Endo, and Shin-ichiro Narita. Optical determination of dielectric constant in black phosphorus. *J. Phys. Soc. Jpn.*, 54:2096–2099, 1985.

[288] Akira Morita, Hideo Asahina, Chioko Kaneta, and Taizo Sasaki. Anisotropic mobility and electron-phonon interaction in black phosphorus. In James D. Chadi and Walter A. Harrison, editors, *Proc. 17th Int. Conf. Phys. Semicond.*, pages 1320–1324, 1985.

[289] Guowei Zhang, Andrey Chaves, Shenyang Huang, Fanjie Wang, Qiaoxia Xing, Tony Low, and Hugen Yan. Determination of layer-dependent exciton binding energies in few-layer black phosphorus. *Sci. Adv.*, 4, 2018.

[290] Gabriel C. Constantinescu and Nicholas D. M. Hine. Multipurpose black-phosphorus/hbn heterostructures. *Nano Lett.*, 16:2586–2594, 2016.

[291] Yifeng Chen and Su Ying Quek. Tunable bright interlayer excitons in few-layer black phosphorus based van der waals heterostructures. *2D Mater.*, 5(4):045031, 2018.

[292] Diana Y. Qiu, Felipe H. da Jornada, and Steven G. Louie. Environmental screening effects in 2d materials: Renormalization of the bandgap, electronic structure, and optical spectra of few-layer black phosphorus. *Nano Lett.*, 17:4706–4712, 2017.

[293] Andres Castellanos-Gomez, Leonardo Vicarelli, Elsa Prada, Joshua O Island, K L Narasimha-Acharya, Sofya I Blanter, Dirk J Groenendijk, Michele Buscema, Gary A Steele, J V Alvarez, Henny W Zandbergen, J J Palacios, and Herre S J van der Zant. Isolation and characterization of few-layer black phosphorus. *2D Mater.*, 1:025001, 2014.

[294] Simone Latini, Kirsten T. Winther, Thomas Olsen, and Kristian S. Thygesen. Interlayer excitons and band alignment in mos2/hbn/wse2 van der waals heterostructures. *Nano Lett.*, 17:938–945, 2017.

[295] AH Castro Neto, Francisco Guinea, Nuno MR Peres, Kostya S Novoselov, and Andre K Geim. The electronic properties of graphene. *Rev. Mod. Phys.*, 81:109, 2009.

[296] KS Novoselov. Nobel lecture: Graphene: Materials in the flatland. *Rev. Mod. Phys.*, 83:837, 2011.

[297] Sheneve Z Butler, Shawna M Hollen, Linyou Cao, Yi Cui, Jay A Gupta, Humberto R Gutiérrez, Tony F Heinz, Seung Sae Hong, Jiaxing Huang, Ariel F Ismach, et al. Progress, challenges, and opportunities in two-dimensional materials beyond graphene. *ACS Nano*, 7:2898–2926, 2013.

[298] Gábor Zsolt Magda, János Pető, Gergely Dobrik, Chanyong Hwang, László P Biró, and Levente Tapasztó. Exfoliation of large-area transition metal chalcogenide single layers. *Sci. Rep.*, 5:14714, 2015.

[299] Juhong Park, Min Su Kim, Eunho Cha, Jeongyong Kim, and Wonbong Choi. Synthesis of uniform single layer ws2 for tunable photoluminescence. *Sci. Rep.*, 7:16121, 2017.

[300] Subhamoy Ghatak, Atindra Nath Pal, and Arindam Ghosh. Nature of electronic states in atomically thin mos2 field-effect transistors. *ACS Nano*, 5:7707–7712, 2011.

[301] Branimir Radisavljevic, Aleksandra Radenovic, Jacopo Brivio, Valentina Giacometti, and Andras Kis. Single-layer mos 2 transistors. *Nat. Nanotechnol.*, 6:147–150, 2011.

[302] Jun Kang, Sefaattin Tongay, Jian Zhou, Jingbo Li, and Junqiao Wu. Band offsets and heterostructures of two-dimensional semiconductors. *Appl. Phys. Lett.*, 102:012111, 2013.

[303] Sajedeh Manzeli, Dmitry Ovchinnikov, Diego Pasquier, Oleg V Yazyev, and Andras Kis. 2d transition metal dichalcogenides. *Nat. Rev. Mater.*, 2:1–15, 2017.

[304] Ruitao Lv, Joshua A Robinson, Raymond E Schaak, Du Sun, Yifan Sun, Thomas E Mallouk, and Mauricio Terrones. Transition metal dichalcogenides and beyond: synthesis, properties, and applications of single-and few-layer nanosheets. *Acc. Chem. Res.*, 48:56–64, 2015.

[305] Wonbong Choi, Nitin Choudhary, Gang Hee Han, Juhong Park, Deji Akinwande, and Young Hee Lee. Recent development of two-dimensional transition metal dichalcogenides and their applications. *Mater. Today*, 20:116–130, 2017.

[306] Ang-Yu Lu, Hanyu Zhu, Jun Xiao, Chih-Piao Chuu, Yimo Han, Ming-Hui Chiu, Chia-Chin Cheng, Chih-Wen Yang, Kung-Hwa Wei, Yiming Yang, et al.

Janus monolayers of transition metal dichalcogenides. *Nat. Nanotechnol.*, 12:744, 2017.

[307] Jing Zhang, Shuai Jia, Iskandar Kholmanov, Liang Dong, Dequan Er, Weibing Chen, Hua Guo, Zehua Jin, Vivek B Shenoy, Li Shi, et al. Janus monolayer transition-metal dichalcogenides. *ACS Nano*, 11:8192–8198, 2017.

[308] Liang Dong, Jun Lou, and Vivek B Shenoy. Large in-plane and vertical piezoelectricity in janus transition metal dichalchogenides. *ACS Nano*, 11:8242–8248, 2017.

[309] Yujin Ji, Mingye Yang, Haiping Lin, Tingjun Hou, Lu Wang, Youyong Li, and Shuit-Tong Lee. Janus structures of transition metal dichalcogenides as the heterojunction photocatalysts for water splitting. *J. Phys. Chem. C*, 122:3123–3129, 2018.

[310] Xiangchao Ma, Xin Wu, Haoda Wang, and Yucheng Wang. A janus mosse monolayer: a potential wide solar-spectrum water-splitting photocatalyst with a low carrier recombination rate. *J. Mater. Chem. A*, 6:2295–2301, 2018.

[311] N. Wakabayashi, H. G. Smith, and R. M. Nicklow. Lattice dynamics of hexagonal mos_2 studied by neutron scattering. *Phys. Rev. B*, 12:659–663, Jul 1975.

[312] Philip B James and MT Lavik. The crystal structure of mose2. *Acta Crystallogr.*, 16:1183–1183, 1963.

[313] Osvald Knop and Roderick D MacDonald. Chalkogenides of the transition elements: Iii. molybdenum ditelluride. *Can. J. Chem.*, 39:897–904, 1961.

[314] A Matthäus, A Ennaoui, S Fiechter, S Tiefenbacher, T Kiesewetter, K Diesner, I Sieber, W Jaegermann, T Tsirlina, and R Tenne. Highly textured films of

layered metal disulfide 2h-ws 2 preparation and optoelectronic properties. *J. Electrochem. Soc.*, 144:1013–1019, 1997.

[315] Arthur Mar, Stephane Jobic, and James A Ibers. Metal-metal vs tellurium-tellurium bonding in wte2 and its ternary variants tairte4 and nbirte4. *J. Am. Chem. Soc.*, 114:8963–8971, 1992.

[316] Srilatha Arra, Rohit Babar, and Mukul Kabir. van der waals heterostructure for photocatalysis: Graphitic carbon nitride and janus transition-metal dichalcogenides. *Phys. Rev. Mater.*, 3:095402, 2019.

[317] Ruiping Li, Yingchun Cheng, and Wei Huang. Recent progress of janus 2d transition metal chalcogenides: from theory to experiments. *Small*, 14:1802091, 2018.

[318] Yu Li Huang, Yifeng Chen, Wenjing Zhang, Su Ying Quek, Chang-Hsiao Chen, Lain-Jong Li, Wei-Ting Hsu, Wen-Hao Chang, Yu Jie Zheng, Wei Chen, et al. Bandgap tunability at single-layer molybdenum disulphide grain boundaries. *Nat. Commun.*, 6:1–8, 2015.

[319] Chendong Zhang, Amber Johnson, Chang-Lung Hsu, Lain-Jong Li, and Chih-Kang Shih. Direct imaging of band profile in single layer mos2 on graphite: quasiparticle energy gap, metallic edge states, and edge band bending. *Nano Lett.*, 14:2443–2447, 2014.

[320] Qiang Zhang, Yuxuan Chen, Chendong Zhang, Chi-Ruei Pan, Mei-Yin Chou, Changgan Zeng, and Chih-Kang Shih. Bandgap renormalization and work function tuning in mose 2/hbn/ru (0001) heterostructures. *Nat. Commun.*, 7:1–7, 2016.

[321] Archana Raja, Andrey Chaves, Jaeeun Yu, Ghidewon Arefe, Heather M Hill, Albert F Rigosi, Timothy C Berkelbach, Philipp Nagler, Christian Schüller,

Tobias Korn, et al. Coulomb engineering of the bandgap and excitons in two-dimensional materials. *Nat. Commun.*, 8:1–7, 2017.

[322] Jun Hong Park, Suresh Vishwanath, Xinyu Liu, Huawei Zhou, Sarah M Eichfeld, Susan K Fullerton-Shirey, Joshua A Robinson, Randall M Feenstra, Jacek Furdyna, Debdeep Jena, et al. Scanning tunneling microscopy and spectroscopy of air exposure effects on molecular beam epitaxy grown wse2 monolayers and bilayers. *ACS Nano*, 10:4258–4267, 2016.

[323] Tobias Korn, Stefanie Heydrich, Michael Hirmer, Johannes Schmutzler, and Christian Schüller. Low-temperature photocarrier dynamics in monolayer mos2. *Appl. Phys. Lett.*, 99:102109, 2011.

[324] Sefaattin Tongay, Jian Zhou, Can Ataca, Kelvin Lo, Tyler S Matthews, Jingbo Li, Jeffrey C Grossman, and Junqiao Wu. Thermally driven crossover from indirect toward direct bandgap in 2d semiconductors: Mose2 versus mos2. *Nano Lett.*, 12:5576–5580, 2012.

[325] Humberto R Gutiérrez, Nestor Perea-López, Ana Laura Elías, Ayse Berkdemir, Bei Wang, Ruitao Lv, Florentino López-Urías, Vincent H Crespi, Humberto Terrones, and Mauricio Terrones. Extraordinary room-temperature photoluminescence in triangular ws2 monolayers. *Nano Lett.*, 13:3447–3454, 2013.

LIST OF PUBLICATIONS

Publications included in this thesis

1. **Srilatha Arra**, K. R. Ramya, Rohit Babar and Mukul Kabir, *Photocatalytic Activity of Phosphorene Derivatives*, J. Phys. Chem. C 112, 7194-7202, (2018)

2. **Srilatha Arra**, Rohit Babar, and Mukul Kabir, *Exciton in phosphorene: Strain, impurity, thickness, and heterostructure*, Physical Review B 99, 045432, (2019)

3. **Srilatha Arra**, Rohit Babar and Mukul Kabir, *van der Waals heterostructure for photocatalysis: Graphitic carbon nitride and Janus transition-metal dichalcogenides*, Phys Rev Materials 3, 095402, (2019)

4. **Srilatha Arra**, Rohit Babar and Mukul Kabir, *Photocatalyst applications and optical properties of 2D Janus transition metal dichalcogenides*, To be published

Publications not included in this thesis

5. Sk Rejaul, **Srilatha Arra**, B. Dhara, Joel S. Miller, M. Kabir and A. Deshpande, *Enhancing Intermolecular Interaction by Cyano Substitution in Copper Phthalocyanine*, J. Phys. Chem. C 122, 429-437, (2018)

6. Sk. Rejaul, **Srilatha Arra**, B. Dhara, Joel S. Miller, M. Kabir, and A. Deshpande, *Effect of Cyano Substitution on the Step-Edge Adsorption of Copper Phthalocyanine on Au(111)*, J. Phys. Chem. C 122, 11848-11854, (2018)